

HIGHLY STABLE POROUS MATERIALS FOR HETEROGENEOUS CATALYSIS
AND CARBON CAPTURE

A Dissertation

by

XINYU YANG

Submitted to the Office of Graduate and Professional Studies of
Texas A&M University
in partial fulfillment of the requirements for the degree of

DOCTOR OF PHILOSOPHY

Chair of Committee,	Hong-Cai Zhou
Committee Members,	Sarbajit Banerjee
	Karen Wooley
	Raymundo Arroyave
Head of Department,	Simon North

August 2019

Major Subject: Chemistry

Copyright 2019 Xinyu Yang

ABSTRACT

Metal-organic frameworks (MOFs) and porous polymer networks (PPNs) are emerging porous materials that exhibit high crystallinity, large surface areas, and excellent tunability. With these features, MOFs and PPNs demonstrate great potentials in heterogeneous catalysis, gas storage/separation, chemical sensing, and biomedical application. This dissertation is focusing on the synthesis of highly stable MOFs and PPNs, and their applications in heterogeneous catalysis and carbon capture.

In the first project, core-shell MOF, PCN-222@Zr-BPDC, was synthesized through one-step strategy under the guidance of nucleation kinetics analysis. The stability, crystallinity, porosity, and structure of PCN-222@Zr-BPDC were characterized. Then, a series of multifunctional core-shell MOFs were synthesized by isorecticular expansion of microporous shell and orthogonal modification of mesoporous core. Taking advantage of the biomimetic catalytic center and adjustable window size, the core-shell MOFs work as an ideal platform for heterogeneous catalysis.

In the second project, I further explored the above-mentioned synthetic strategy. First, four zirconium core-shell MOFs with needle-like cores and octahedral shells were prepared. To demonstrate the versatility of the kinetically controlled strategy, a series of core-shell MOFs with mismatching lattice and different metals were synthesized. With the well-defined pores, the core-shell MOFs persist excellent shape and size selectivity in olefin epoxidation.

In the third project, three alkylamine tethered PPNs were developed. A novel post-synthetic modification strategy was proposed to construct alkylamine tethered PPNs to replace the liquid amine that was widely used in post-combustion carbon capture. By utilizing the polarizability and quadrupole moment of CO₂, the materials showed significant increases in CO₂ uptake capacities and high CO₂/N₂ selectivity.

In summary, a series of highly stable porous materials have been synthesized for different applications. In particular, the nucleation kinetics control has been demonstrated as a facile strategy to synthesize hybrid core-shell MOFs and anchor installation shows great potential in carbon capture.

DEDICATION

To my family for their love and support.

To my friends who helped me during my study in U.S.

ACKNOWLEDGEMENTS

I would like to express my thanks to my committee chair Dr. Hong-Cai Zhou, and my committee members, Dr. Sarbajit Banerjee, Dr. Karen Wooley, and Dr. Raymundo Arroyave for their guidance and support in the past five years.

I will always appreciate my advisor, Dr. Hong-Cai Zhou, for offering me the great opportunity to work in his group. He gave me much insightful guidance and pushed me toward success in finishing my degree. I would also like to acknowledge the Zhou group members from the past and present. Special thanks to Dr. Shuai Yuan, Dr. Jun-Sheng Qin, Dr. Lanfang Zou, and Ms. Yingmu Zhang for their mentorship and the best discussion and help.

Thanks also go to my friends and colleagues and the department faculty and staff for making my time in Texas A&M University a great experience.

Finally, I would like to express my appreciation to my wife and my parents for their patience and love.

CONTRIBUTORS AND FUNDING SOURCES

Contributors

This work was supervised by a dissertation committee consisting of Professor Hong-Cai Zhou, Professor Sarbajit Banerjee, and Professor Karen Wooley of the Department of Chemistry and Professor Raymundo Arroyave of the Department of Materials Science and Engineering.

All work conducted for the dissertation was completed by the student independently.

Funding Sources

Graduate study was supported by a fellowship from Texas A&M University.

This work was also made possible in part by the Center for Gas Separations Relevant to Clean Energy Technologies, and Energy Frontier Research Center funded by the U.S. Department of Energy, Office of Science, Office of Basic Energy Sciences under Award Number DE-SC0001015, by the Hydrogen and Fuel Cell Program under Award Number DE-EE0007049, by the financial supports of U.S. Department of Energy Office of Fossil Energy, National Energy Technology Laboratory under Award Number DE-FE0026472, by the Welch Foundation under Award Number A-1725.

Its contents are solely the responsibility of the authors and do not necessarily represent the official views of the funding offices.

NOMENCLATURE

MOFs	Metal-Organic Frameworks
PPNs	Porous Polymer Networks
COFs	Covalent Organic Frameworks
PCN	Porous Coordination Network
HKUST	Hong Kong University of Science and Technology
MIL	Material from Institute Lavoisier
ZIFs	Zeolitic Imidazole Frameworks
IRMOF	Isorecticular Metal-Organic Framework
BET	Brunauer-Emmett-Teller
PXRD	Powder X-Ray Diffraction
TGA	Thermogravimetric Analyzer
SEM	Scanning Electron Microscopy

TABLE OF CONTENTS

	Page
ABSTRACT	ii
DEDICATION	iv
ACKNOWLEDGEMENTS	v
CONTRIBUTORS AND FUNDING SOURCES.....	vi
NOMENCLATURE.....	vii
TABLE OF CONTENTS	viii
LIST OF FIGURES.....	x
LIST OF TABLES	xvi
CHAPTER I INTRODUCTION TO HIGHLY STABLE POROUS MATERIALS: DESIGN, SYNTHESIS, AND APPLICATION.....	1
1.1 Introduction to Stable Metal-Organic Framework	1
1.2 Metal-Organic Frameworks as Heterogeneous Catalyst.....	9
1.2.1 Lewis Acid Catalysis.....	9
1.2.2 Brønsted Acid Catalysis	12
1.2.3 Redox Catalysis	14
1.2.4 Photocatalysis	18
1.3 Introduction to Porous Polymer Network for Carbon Capture	20
1.3.1 Technologies/Methods and Challenges in CO ₂ Capture	20
1.3.2 CO ₂ Capture by Traditional Sorbents/Advanced Sorbents (PPNs).....	23
CHAPTER II ONE-STEP SYNTHESIS OF HYBRID CORE-SHELL METAL- ORGANIC FRAMEWORKS	26
2.1 Introduction	26
2.2 Experimental Section	29
2.2.1 Materials and Instrumentation.....	29
2.2.2 Ligand Synthesis	30
2.2.3 MOF Synthesis	35
2.3 Result and Discussion	37

2.4 Conclusion.....	60
CHAPTER III FURTHER DEVELOPMENT OF HYBRID CORE-SHELL MOF	61
3.1 Introduction	61
3.2 Experimental Section	64
3.2.1 Materials and Instruments	64
3.2.2 Ligand Synthesis	65
3.2.3 MOF Synthesis.....	72
3.3 Results and Discussion.....	74
3.4 Conclusion.....	88
CHAPTER IV ANCHOR INSTALLATION ON POROUS POLYMER NETWORKS (PPNS) FOR HIGH CO ₂ UPTAKE	89
4.1 Introduction	89
4.2 Experimental Section	93
4.2.1 Materials and Instrumentation.....	93
4.2.2 Ligand Synthesis	94
4.2.3 PPN Synthesis	96
4.2.4 Calculation of CO ₂ /N ₂ Selectivity	98
4.3 Results and Discussion.....	99
4.4 Conclusion.....	113
CHAPTER V SUMMARY AND PERSPECTIVE	114
5.1 Project Summary	114
5.2 Outlook.....	116
5.2.1 The Future of MOFs.....	116
5.2.2 Future Work: Tuning Selective Behavior by the Hydrophobicity of Shell MOF	117
5.2.3 Future Work: One-Step Synthesis of Binary Metal Core-Shell MOF	118
REFERENCES.....	119

LIST OF FIGURES

	Page
Figure I-1 Introduction to Metal-Organic Framework	1
Figure I-2 Rate of aqua ligand exchange for different metal cations as reference for M-L bond dissociation rate in carboxylate containing MOFs	3
Figure I-3 Illustration of the assembly of MIL-53/47 from ditopic carboxylate linkers and infinite chain clusters; metal ions can be Cr ³⁺ , Fe ³⁺ , Al ³⁺ , and V ⁴⁺ (MIL-47). Breathing effect is illustrated; ditopic carboxylate linkers could be bdc, ndc, and bpdc with/without functionalities. Color scheme: metal (turquoise); O (red); C (black). Reprinted with permission from Ref. 74 copyright © 2014 The Royal Society of Chemistry.	4
Figure I-4 Illustration of the assembly of MIL-100 from the btc linker and the trigonal-prismatic cluster; metal ions can be Cr ³⁺ , V ³⁺ , Fe ³⁺ , and Al ³⁺ . Color scheme: chromium (turquoise); O (red); C (black). Reprinted with permission from Ref. 74 copyright © 2014 The Royal Society of Chemistry. ...	5
Figure I-5 Illustration of the assembly of MIL-101 and MIL-88 from ditopic carboxylate linkers and trigonal-prismatic clusters; metal ions can be Cr ³⁺ , V ³⁺ , Fe ³⁺ , and Al ³⁺ . For MIL-88, the swelling effect is illustrated; ditopic linkers could be bdc, ndc, and bpdc with/without functionalities. Color scheme: Cr (turquoise polyhedra); O (red); C (black). Reprinted with permission from Ref. 74 copyright © 2014 The Royal Society of Chemistry. ...	5
Figure I-6 (a) One unit cell of copper drawn to scale with: (b) Zr-MOF with 1,4-benzene-dicarboxylate (BDC) as linker, UiO-66, (c) Zr-MOF with 4,4' - biphenyl-dicarboxylate (BPDC) as linker, UiO-67, (d) Zr-MOF with terphenyl dicarboxylate (TPDC) as linker, UiO-68. Zirconium, oxygen, carbon, and hydrogen atoms are red, blue, gray, and white, respectively. Reprinted with permission from Ref. 75, copyright © 2008 American Chemical Society	6
Figure I-7 Crystal structure and underlying network topology of PCN-222(Fe). The Fe-TCPP (a; blue square) is connected to four 8-connected Zr ₆ clusters (b; light orange cuboid) with a twisted angle to generate a 3D network in Kagome-like topology (d,e) with 1D large channels (c; green pillar). Zr black spheres, C gray, O red, N blue, Fe orange. H atoms were omitted for clarity. Reprinted with permission from Ref. 76, copyright © 2012 John Wiley and Sons.	7

Figure I-8 (a) the 6-connected D_{3d} symmetric Zr_6 in PCN-224. (b) Tetratopic TCPP(Ni) ligands (violet square) with twisted dihedral angles generate a framework with three dimensional channels (c, d). Color scheme: Zr, green spheres; C, gray; O, red; N, blue; Ni, orange; and H, white. Reprinted with permission from Ref. 77, copyright © 2013 American Chemical Society.....	8
Figure I-9 Removal of the coordinated trifluoroacetic acid by thermal activation. Reproduced with permission from Ref. 86 Copyright 2013 © American Chemical Society.	10
Figure I-10 The preparation of sulfated MOF-808 with both Lewis acidity and Bronsted acidity. Reprinted with permission from Ref. 90 copyright © 2014 American Chemical Society.	13
Figure I-11 Schematic representation of the immobilization of AuNi nanoparticles by the MIL-101 matrix using DSM combined with a liquid-phase CCR strategy. Reproduce with permission from Ref. 99 copyright © 2013 American Chemical Society.	15
Figure I-12 Illustration of the synthetic route to generate MIL-101@Pt@MIL-101, comprised of Pt nanoparticles (NPs) sandwiched between a core and a shell of MIL-101. Reproduced with permission from Ref. 100 copyright © 2016 American Association for the Advancement of Science.	16
Figure I-13 Different technologies and materials for CO ₂ separation and capture.	21
Figure I-14 The synthetic routes of (a) PPN-3, 4, 5, 6, (b) amine-tethered PPN-6 and (c) synthesis and amine-incorporation of PPN-125.	25
Figure II-1 Kinetically guided synthesis of a hybrid core-shell PCN-222@Zr-BPDC. ...	38
Figure II-2 Optical microscopic image of PCN-222@Zr-BPDC.	39
Figure II-3 SEM images of PCN-222@Zr-BPDC from different cross sections.	39
Figure II-4 PXRD patterns of Zr-BPDC, PCN-222 and PCN-222@Zr-BPDC.	40
Figure II-5 Gas adsorption isotherms of Zr-BPDC, PCN-222 and PCN-222@Zr-BPDC.	40
Figure II-6 Pore size distribution of PCN-222@Zr-BPDC. Insert shows the mesopores from PCN-222.	41
Figure II-7 Time course analysis of formation of PCN-222 (red), PCN-222@Zr-BPDC (blue) and Zr-BPDC (black).	42

Figure II-8 PXRD of PCN-222(Fe)@Zr-BPDC, PCN-222(Ni)@Zr-BPDC, PCN-222(Mn)@Zr-BPDC, and PCN-222(Zn)@Zr-BPDC.....	44
Figure II-9 Microscopic images of PCN-222@Zr-NDC, PCN-222@Zr-BPDC, PCN-222@Zr-BPYDC, PCN-222@Zr-BPDC-NO ₂ , PCN-222@Zr-BPDC-I, PCN-222@Zr-BPDC-OMe, and PCN-222@Zr-AZDC.....	44
Figure II-10 PXRD patterns of PCN-222@Zr-BPYDC, PCN222, and Zr-BPYDC.....	45
Figure II-11 PXRD patterns of PCN-222@Zr-BPDC-NO ₂ , PCN-222, and Zr-BPDC-NO ₂	45
Figure II-12 PXRD patterns of PCN-222@Zr-BPDC-I, PCN-222, and Zr-BPDC-I.....	46
Figure II-13 PXRD of PCN-222@Zr-BPDC-OMe, PCN-222, and Zr-BPDC-OMe.....	46
Figure II-14 N ₂ Uptake of PCN-222@Zr-BPYDC.	47
Figure II-15 N ₂ Uptake of PCN-222@Zr-BPDC-NO ₂	47
Figure II-16 N ₂ Uptake of PCN-222@Zr-BPDC-I.	48
Figure II-17 N ₂ Uptake of PCN-222@Zr-BPDC-OMe.	48
Figure II-18 Microscopic image of PCN-222@Zr-NDC.	49
Figure II-19 Microscopic image of PCN-222@Zr-AZDC.....	49
Figure II-20 SEM images of PCN-222@Zr-NDC.	50
Figure II-21 SEM images of PCN-222@Zr-BPDC.	50
Figure II-22 SEM images of PCN-222@Zr-AZDC.....	50
Figure II-23 PXRD patterns of Zr-NDC, PCN-222 and PCN-222@Zr-NDC.	51
Figure II-24 PXRD patterns of Zr-AZDC, PCN-222 and PCN-222@Zr-AZDC.	51
Figure II-25 Gas adsorption isotherms of Zr-NDC, PCN-222 and PCN-222@Zr-NDC.....	52
Figure II-26 Gas adsorption isotherms of Zr-AZDC, PCN-222 and PCN-222@Zr-AZDC.	52
Figure II-27 ¹ H NMR of PCN-222@Zr-NDC.	55

Figure II-28 ^1H NMR of PCN-222@Zr-BPDC.	56
Figure II-29 ^1H NMR of PCN-222@UiO-AZDC.	56
Figure II-30 Size selective olefin epoxidation using PCN-222(Fe)@Zr-NDC, PCN-222(Fe)@Zr-BPDC, PCN-222(Fe)@Zr-AZDC, and PCN-222-(Fe).	57
Figure II-31 PXRD of as-synthesized and after catalysis PCN-222(Fe)@Zr-NDC.	58
Figure II-32 PXRD of as-synthesized and after catalysis PCN-222(Fe)@Zr-BPDC.	58
Figure II-33 PXRD of as-synthesized and after catalysis PCN-222(Fe)@Zr-AZDC.	59
Figure III-1 Photographs of bimetallic and trimetallic hierarchical single crystals showing visually distinguishable colors (1-3, under daylight) or emissive colors (4-15, under UV radiation, $\lambda_{\text{ex}}=350$ nm), while solid-solution crystals show uniform emissive colors (16-18, under UV radiation, $\lambda_{\text{ex}}=350$ nm). Eu@Tb-MOF means Eu/Tb bimetallic crystal grown from Eu-MOF seed, and so on.	62
Figure III-2 PCN-222@Zr-TPDC-2Me	75
Figure III-3 PCN-222@Zr-TPDC-4Me	75
Figure III-4 PCN-222@Zr-TPDC-2Ph	76
Figure III-5 PCN-222@Zr-TPDC-2Hex	76
Figure III-6 PXRD patterns of PCN-222, Zr-TPDC-2Me, and PCN-222@Zr-TPDC-2Me	77
Figure III-7 PXRD patterns of PCN-222, Zr-TPDC-4Me, and PCN-222@Zr-TPDC-4Me	78
Figure III-8 PXRD patterns of PCN-222, Zr-TPDC-2Ph, and PCN-222@Zr-TPDC-2Ph	78
Figure III-9 PXRD patterns of PCN-222, Zr-TPDC-2Hex, and PCN-222@Zr-TPDC-2Hex.....	79
Figure III-10 Gas adsorption isotherms of PCN-222, Zr-TPDC-2Me, and PCN-222@Zr-TPDC-2Me.....	79
Figure III-11 Gas adsorption isotherms of PCN-222, Zr-TPDC-4Me, and PCN-222@Zr-TPDC-4Me.....	80

Figure III-12 Gas adsorption isotherms of PCN-222, Zr-TPDC-2Ph, and PCN-222@Zr-TPDC-2Ph.....	80
Figure III-13 Gas adsorption isotherms of PCN-222, Zr-TPDC-2Hex, and PCN-222@Zr-TPDC-2Hex	81
Figure III-14 SEM image of PCN-222@Zr-TPDC-2Me	81
Figure III-15 Optical image of PCN-134@Zr-BTB.....	84
Figure III-16 PXRD patterns of Zr-BTB, PCN-134 and PCN-134@Zr-BTB.....	84
Figure III-17 Gas adsorption isotherms of Zr-BTB, PCN-134 and PCN-134@Zr-BTB.....	85
Figure III-18 Microscopic image of PCN-222@Nu-1000.....	85
Figure III-19 PXRD patterns of Nu-1000, PCN-222 and PCN-222@Nu-1000.	86
Figure III-20 Microscopic image of La-TCPP@La-BPDC.	86
Figure III-21 PXRD patterns of La-BPDC, La-TCPP and La-TCPP@La-BPDC.....	87
Figure IV-1 N ₂ sorption at 77 K with changing solvent.	100
Figure IV-2 N ₂ sorption at 77 K with different amount of K ₂ CO ₃	100
Figure IV-3 N ₂ sorption at 77 K with different amount of CsF.	101
Figure IV-4 N ₂ isotherm of optimized PPN-200.....	102
Figure IV-5 Pore size distribution of PPN-200.....	103
Figure IV-6 The PXRD pattern of the fresh PPN-200.....	103
Figure IV-7 SEM image of PPN-200.....	104
Figure IV-8 SEM image of PPN-200Br.....	104
Figure IV-9 SEM image of PPN-200-DETA.....	105
Figure IV-10 SEM image of PPN-200-TETA.	105
Figure IV-11 SEM image of PPN-200-TAEA.....	106
Figure IV-12 N ₂ isotherms of PPN-200, PPN-200Br, and PPN-200-amines.	108

Figure IV-13 TGA of PPN-200.....	108
Figure IV-14 TGA of PPN-200Br.....	109
Figure IV-15 TGA of PPN-200-DETA.....	109
Figure IV-16 TGA of PPN-200-TETA.....	110
Figure IV-17 TGA of PPN-200-TAEA.....	110
Figure IV-18 FT-IR patterns of the PPN-200, PPN-200Br, and PPN-200-amines.....	111
Figure IV-19 CO ₂ adsorption of PPN-200Br and PPN-200-amines.....	111
Figure IV-20 CO ₂ and N ₂ adsorption for PPN-200-TAEA at 298K.....	112
Figure V-1 Advantages of core-shell MOFs.....	117

LIST OF TABLES

	Page
Table II-1 PCN-222(Fe)@Zr-BPDC catalyzed epoxidation of alkenes. ^a	54
Table III-1 PCN-222(Fe)@Zr-TPDC-2Me, PCN-222(Fe)@Zr-TPDC-4Me, PCN-222(Fe)@Zr-TPDC-2Ph, and PCN-222(Fe)@Zr-TPDC-2Hex catalyzed epoxidation of alkenes ^{a,b}	82
Table IV-1 N ₂ adsorption capabilities of PPN-200 under different conditions.	101
Table IV-2 Element characterization of PPN-200Br, PPN-200-DETA, PPN-200-TETA, and PPN-200-TAEA.....	107

CHAPTER I

INTRODUCTION TO HIGHLY STABLE POROUS MATERIALS: DESIGN, SYNTHESIS, AND APPLICATION¹

1.1 Introduction to Stable Metal-Organic Framework

Metal-Organic Frameworks (MOFs) are an emergent class of crystalline porous materials, which have received considerable attention in the past two decades.¹⁻⁵ MOF is composed of inorganic metal clusters and organic linkers. (Figure I-1) The orthogonal

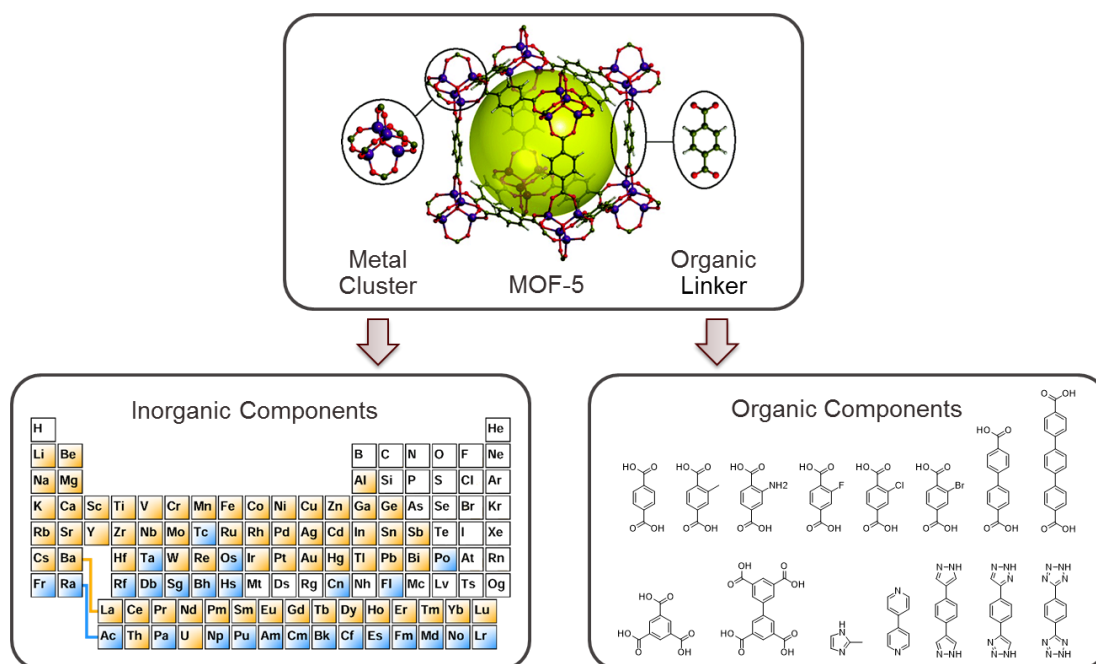


Figure I-1 Introduction to Metal-Organic Framework

¹ Part of this chapter is reproduced with permission from “Stable Metal-Organic Frameworks: Design, Synthesis, and Applications” by Yuan, S.; Feng, L.; Wang, K.; Pang, J.; Bosch, M.; Lollar, C.; Sun, Y.; Qin, J.; Yang, X.; Zhang, P.; Wang, Q.; Zou, L.; Zhang, Y.; Zhang, L.; Fang, Y.; Li, J.; Zhou, H.-C. *Adv. Mater.* **2018**, 30, 1704303, copyright 2018 by Wiley-Vch Verlag GmbH & Co. KGaA, Weinheim.

modification of these two parts makes MOF own excellent structural and functional tunability. Compared to other conventional porous materials including zeolite,^{6, 7} mesoporous silica,⁸⁻¹¹ and activated carbons,¹²⁻¹⁵ MOFs exhibit high crystallinity, large surface areas, and diverse functionality. Due to the above-mentioned advantages, MOFs show great potential in various applications, such as gas storage/separation,¹⁶⁻³² heterogeneous catalysis,^{1, 33-44} chemical sensing,⁴⁵⁻⁵¹ energy storage,⁵²⁻⁵⁷ and biomedical aspects.⁵⁸⁻⁶⁸

The stability of MOFs under harsh conditions is a prerequisite for applications in heterogeneous catalysis. As most MOFs are based on carboxylate ligand, the development of stable carboxylate-based MOF will be introduced. Many early MOFs made from divalent metals, such as Zn²⁺ or Cu²⁺,^{2, 69} have shown exceptional porosity and promise for a wide variety of applications, but ultimately proved unsuitable for use under harsh conditions because of stability issues. For instance, Nu-110, who displayed the highest experimental Brunauer-Emmett-Teller (BET) surface area (7000 m²/g) of any porous materials reported to date, must use supercritical CO₂ activation technique to avoid pore collapse.⁷⁰ When MOFs are used for certain applications, their framework integrity must be guaranteed to maintain their intended functionalities and characteristics. The instability of many MOFs in water or other harsh conditions has considerably limited their further application. Therefore, the chemical stability of MOFs has been receiving more and more attention.

The stability of MOFs can be affected by multiple factors, including the operating environment, metal ions, organic ligands, metal-ligand coordination geometry,

hydrophobicity of the pore, etc. The metal-ligand bond strength determines the thermodynamic stability of MOFs under many operating environments. Therefore, the stability of MOFs can be roughly predicted by examining the strength of the bonds that form the framework. It is known that the metal-ligand bond strengths with a given ligand are positively correlated to charges of the metal cations and negatively correlated to the ionic radius. The effects of charge and radius can be combined into the concept of charge density. When the ligands and the coordination environment remain the same, high-valent metal ions with high charge density can form stronger coordination bonds and thus a more stable framework. This trend is in line with Pearson's hard/soft acid/base (HSAB) principle and corroborated by many observations in MOF research (Figure I-2). The carboxylate-based ligands can be regarded as hard bases, which form stable MOFs with high-valent metal ions, such as Ti^{4+} , Zr^{4+} , Al^{3+} , Fe^{3+} , and Cr^{3+} .

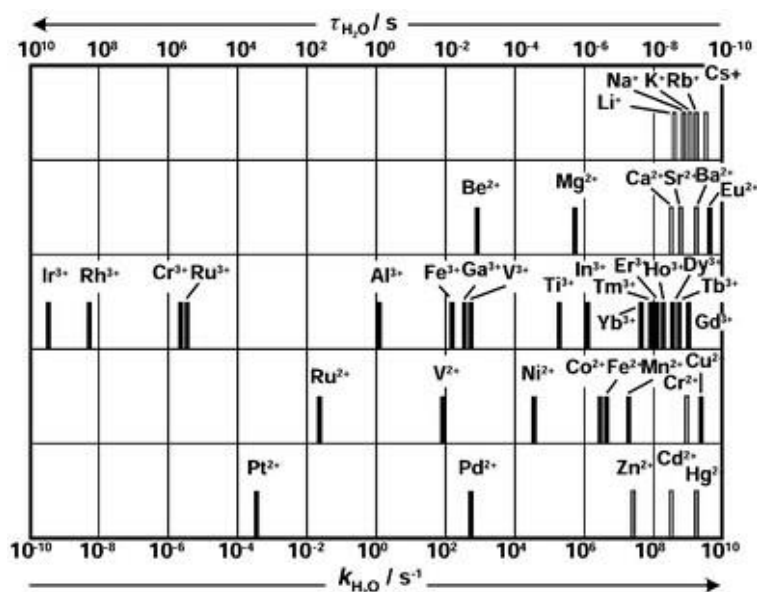


Figure I-2 Rate of aqua ligand exchange for different metal cations as reference for M-L bond dissociation rate in carboxylate containing MOFs

Early stage works on high-valent metal based MOFs were established by Férey and co-workers who developed the Al^{3+} , Fe^{3+} , and Cr^{3+} based MIL series (MIL= Material Institute Lavoisier) including well-known MIL-53 (Figure I-3),⁷¹ MIL-88,⁷² MIL-100 (Figure I-4), and MIL-101 (Figure I-5).^{73, 74} The Zr^{4+} based MOFs were first synthesized in 2008 and have attracted considerable attention since 2012 because of their remarkable stability in water and even acidic conditions.⁷⁵ Following this trend, an escalating number of stable MOFs have been synthesized and reported in recent years.

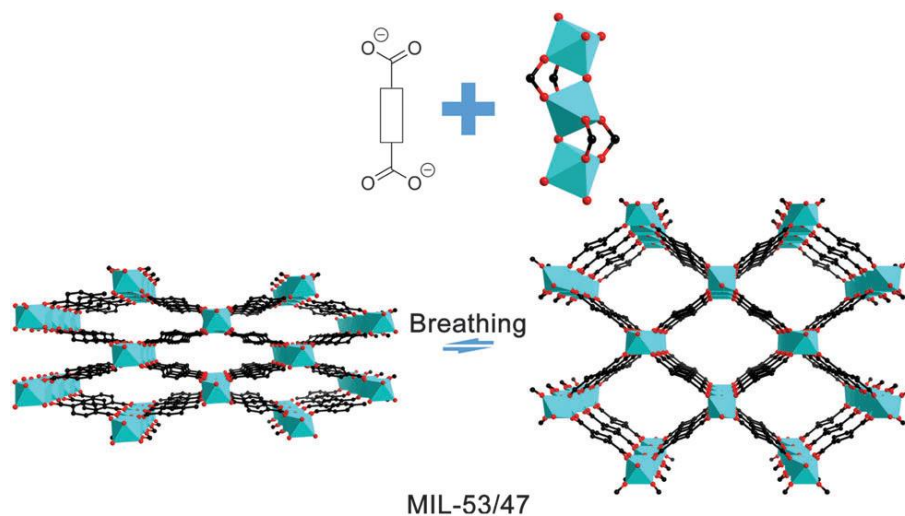


Figure I-3 Illustration of the assembly of MIL-53/47 from ditopic carboxylate linkers and infinite chain clusters; metal ions can be Cr^{3+} , Fe^{3+} , Al^{3+} , and V^{4+} (MIL-47). Breathing effect is illustrated; ditopic carboxylate linkers could be bdc, ndc, and bpdc with/without functionalities. Color scheme: metal (turquoise); O (red); C (black). Reprinted with permission from Ref. 74 copyright © 2014 The Royal Society of Chemistry.

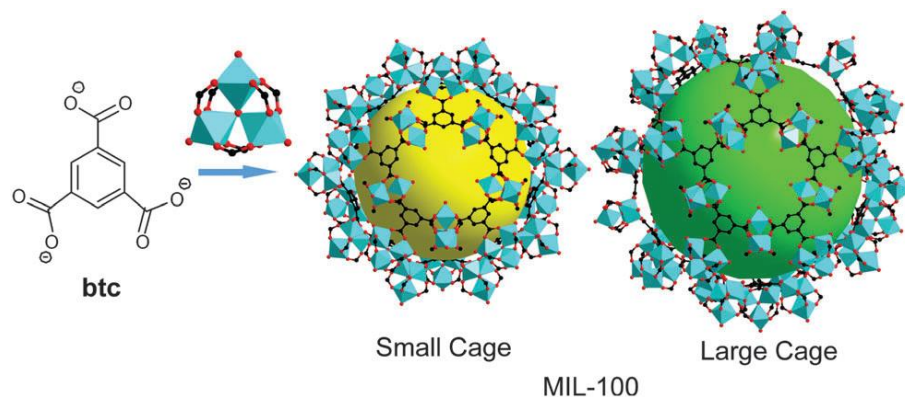


Figure I-4 Illustration of the assembly of MIL-100 from the btc linker and the trigonal-prismatic cluster; metal ions can be Cr^{3+} , V^{3+} , Fe^{3+} , and Al^{3+} . Color scheme: chromium (turquoise); O (red); C (black). Reprinted with permission from Ref. 74 copyright © 2014 The Royal Society of Chemistry.

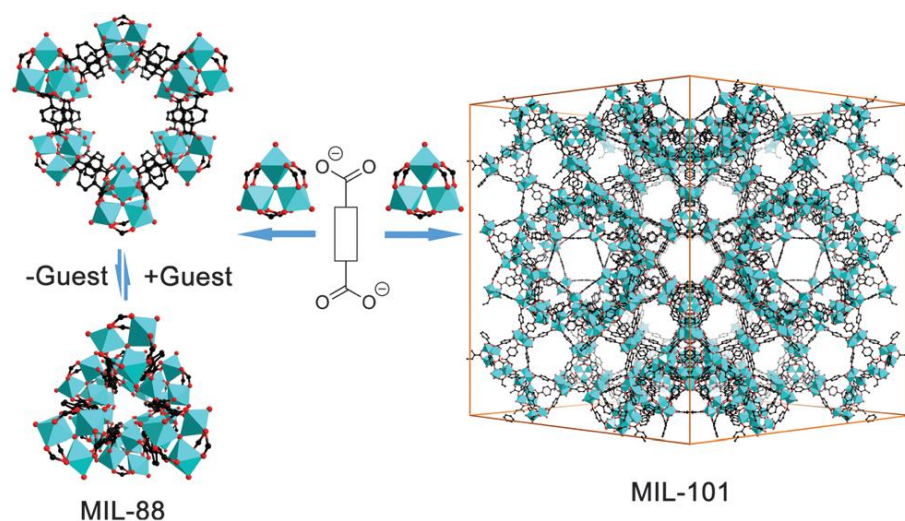


Figure I-5 Illustration of the assembly of MIL-101 and MIL-88 from ditopic carboxylate linkers and trigonal-prismatic clusters; metal ions can be Cr^{3+} , V^{3+} , Fe^{3+} , and Al^{3+} . For MIL-88, the swelling effect is illustrated; ditopic linkers could be bdc, ndc, and bpdc with/without functionalities. Color scheme: Cr (turquoise polyhedra); O (red); C (black). Reprinted with permission from Ref. 74 copyright © 2014 The Royal Society of Chemistry.

The first example of the Zr-MOF, UiO-66 (UiO= University of Oslo), (Figure I-6) was reported in 2008.⁷⁵ It is constructed from 12-connected $[\text{Zr}_6(\mu_3\text{-O})_4(\mu_3\text{-OH})_4(\text{COO})_{12}]$ clusters and linear dicarboxylate linkers. Within the octahedral cluster, six vertices are

occupied by Zr^{4+} and eight triangular faces are alternatively capped by four μ_3 -OH and four μ_3 -O. The $[Zr_6(\mu_3-O)_4(\mu_3-OH)_4]$ core is further terminated by 12 carboxylates forming $[Zr_6(\mu_3-O)_4(\mu_3-OH)_4(COO)_{12}]$ clusters. Topologically, each cluster can be simplified into a 12-connected cuboctahedral node, which is extended into an **fcu** network by linear linkers. The microporous pore is observed in the structure, leading to a BET surface area close to $1200 \text{ m}^2 \text{ g}^{-1}$. At the same time, two isorecticular structures, UiO-67 and UiO-68, with increased surface area (3000 and $4170 \text{ m}^2 \text{ g}^{-1}$ for UiO-67 and UiO-68, respectively), were also synthesized by the elongation of linkers.

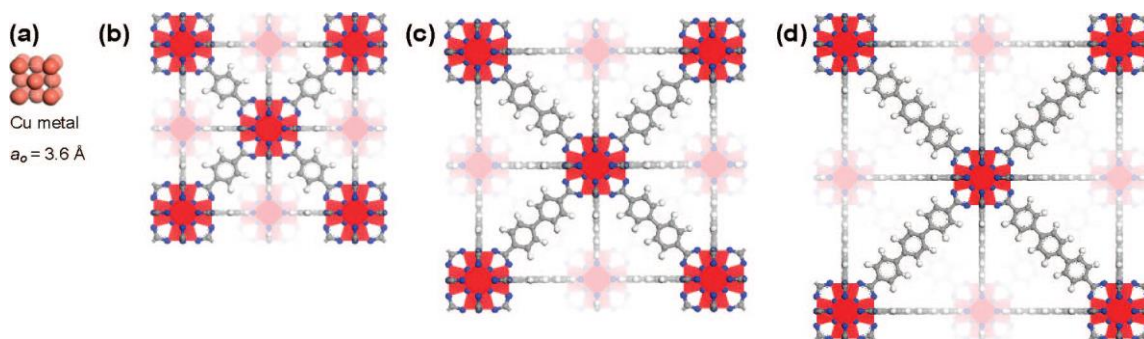


Figure I-6 (a) One unit cell of copper drawn to scale with: (b) Zr-MOF with 1,4-benzene-dicarboxylate (BDC) as linker, UiO-66, (c) Zr-MOF with 4,4'-biphenyl-dicarboxylate (BPDC) as linker, UiO-67, (d) Zr-MOF with terphenyl dicarboxylate (TPDC) as linker, UiO-68. Zirconium, oxygen, carbon, and hydrogen atoms are red, blue, gray, and white, respectively. Reprinted with permission from Ref. 75, copyright © 2008 American Chemical Society

PCN-222 (PCN = porous coordination network) was reported in 2012.⁷⁶ It is composed of heme-like porphyrinic ligand and highly stable Zr_6 cluster. With carefully selected starting materials and topology design, PCN-222(Fe) contains one of the largest known 1D open channels, with a diameter of up to 3.7 nm (Figure I-7). The porosity of PCN-222(Fe) was examined by nitrogen adsorption experiments at 77K. The typical IV isotherm of PCN-222(Fe) exhibits a steep increase at the point of $P/P_0=0.3$, suggesting

mesoporosity. A N_2 uptake of $1009 \text{ cm}^3\text{g}^{-1}$ and a BET surface area of $2200 \text{ m}^2\text{g}^{-1}$ have been observed. PCN-222(Fe) also shows exceptional stability, even in concentrated hydrochloric acid. With the TCPP (TCPP = tetrakis(4-carboxylphenyl)porphyrin) ligand in the structure, PCN-222(Fe) exhibits biomimetic catalytic activities and shows good activity for the oxidation of a variety of substrates.

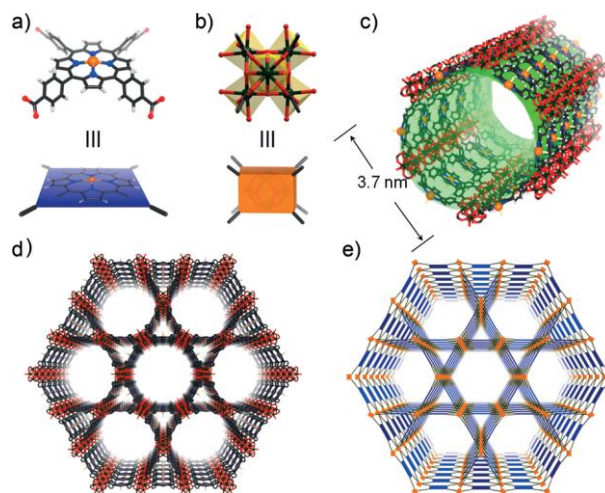


Figure I-7 Crystal structure and underlying network topology of PCN-222(Fe). The Fe-TCPP (a; blue square) is connected to four 8-connected Zr_6 clusters (b; light orange cuboid) with a twisted angle to generate a 3D network in Kagome-like topology (d,e) with 1D large channels (c; green pillar). Zr black spheres, C gray, O red, N blue, Fe orange. H atoms were omitted for clarity. Reprinted with permission from Ref. 76, copyright © 2012 John Wiley and Sons.

PCN-224 (no metal, Ni, Co, Fe) were reported in 2013.⁷⁷ PCN-224, with three-dimensional channels as large as 19\AA , was based on six-connected Zr_6 cluster with D_{3d} symmetry and porphyrinic ligand. PCN-224 crystallizes in space group $Im\bar{3}m$. Each $\text{Zr}_6(\text{OH})_8$ cluster, in which all of the triangular faces in a Zr_6 -octahedron are capped by μ_3 -OH groups, is connected to six TCPP ligands. (Figure I-8) Except for exhibits a large BET surface area ($2600 \text{ m}^2\text{g}^{-1}$), PCN-224 also presents excellent stability and remains intact in pH=0 to pH=11 aqueous solution. Remarkably, PCN-224(Co) exhibits high catalytic

activity for the CO₂/propylene oxide coupling reaction and can be used as a recoverable heterogeneous catalyst.

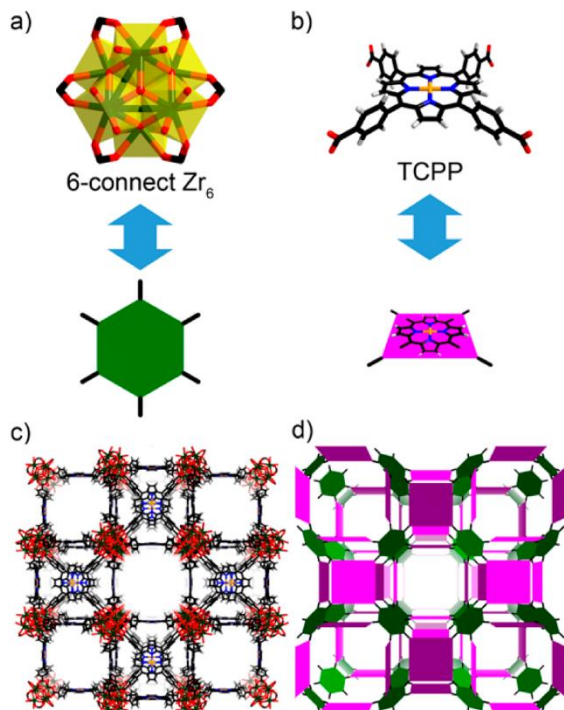


Figure I-8 (a) the 6-connected D_{3d} symmetric Zr_6 in PCN-224. (b) Tetratopic TCPP(Ni) ligands (violet square) with twisted dihedral angles generate a framework with three dimensional channels (c, d). Color scheme: Zr, green spheres; C, gray; O, red; N, blue; Ni, orange; and H, white. Reprinted with permission from Ref. 77, copyright © 2013 American Chemical Society.

1.2 Metal-Organic Frameworks as Heterogeneous Catalyst

1.2.1 Lewis Acid Catalysis

Coordinately unsaturated metal sites in MOFs have been found to act as Lewis acidic sites for catalysis. For gas phase catalysis, these sites can be exposed by the activation process (e.g., heating and evacuation) to remove the coordinated solvent molecules. In solution, the active metal sites can interact with the substrate by replacing the coordinated solvent molecules with substrate molecules. For stable MOFs based on high-valency metals and carboxylates, the metal nodes provide inherent Lewis acidic sites. Studies have shown that the Lewis acidic sites in MOFs can catalyze a variety of reactions, such as the cyanosilylation of aldehydes,⁷⁸ α -pinene oxide isomerization,⁷⁹ Friedel-Crafts reaction,⁸⁰ Hetero-Diels-Alder (hDA) reaction,⁸¹ and the cycloaddition of CO₂ and epoxides.^{77, 82} Some typical examples of stable MOFs for Lewis acid catalysis will be summarized based on the valence of metals in this section.

M³⁺-based MOF catalysts: The MIL-series (e.g., MIL-47, MIL-53, MIL-88, MIL-100, and MIL-101) are among the most widely studied classes of MOFs with trivalent metals (e.g., Al³⁺, Cr³⁺, and Fe³⁺) for Lewis acid catalysis. By removing terminal water molecules on the [Fe₃(μ_3 -O)(OH)(H₂O)₂(COO)₆] cluster, the generated metal sites in MIL-100(Fe) can act as Lewis acidic sites for catalytic reactions, including Friedel-Crafts reactions,⁸⁰ regioselective ring-opening of epoxides,⁸³ Claisen-Schmidt condensation,⁸⁴ and isomerization of α -pinene oxide.⁷⁹ For instance, the Friedel-Crafts benzylation catalytic tests conducted by Férey and co-workers showed that 100% benzyl chloride

conversion with nearly 100% diphenylmethane selectivity was attained after 5 min, indicating high activity and selectivity for MIL-100(Fe).⁸⁰

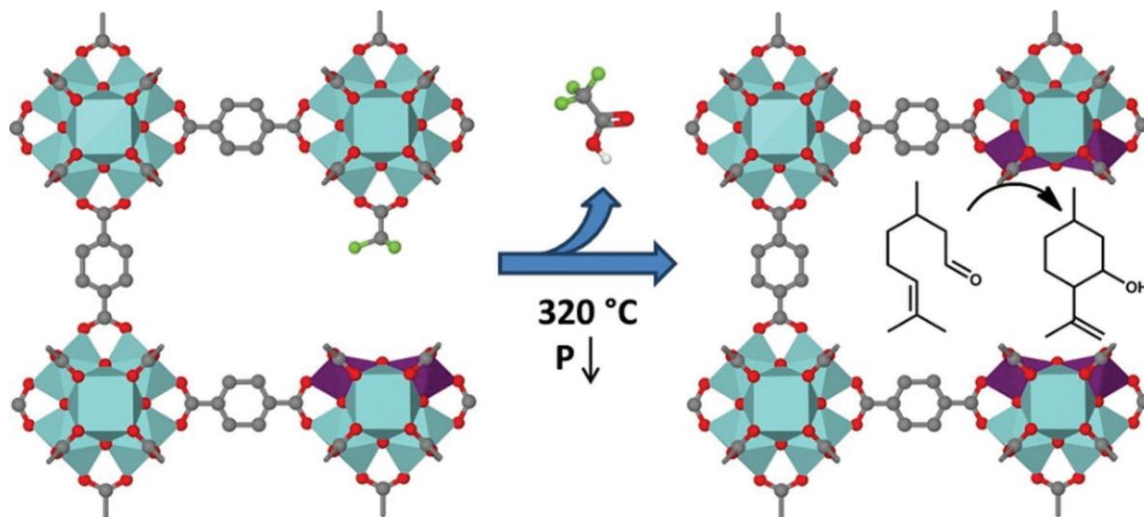


Figure I-9 Removal of the coordinated trifluoroacetic acid by thermal activation. Reproduced with permission from Ref. 86 Copyright 2013 © American Chemical Society.

M^{4+} -based MOF catalysts: Due to their high chemical stability, Zr-based MOFs have been widely studied in recent years as heterogeneous Lewis acidic catalysts. A representative example of Zr-MOFs is UiO-66 composed of $[Zr_6(\mu_3-O)_4(\mu_3-OH)_4(COO)_{12}]$ clusters and BDC (BDC= benzene-1,4-dicarboxylate) linkers. With high-valent Zr^{4+} sites, UiO-66 has been studied for a variety of catalytic reactions including the aldol condensation reaction,⁸⁵ the cyclization of citronellal, etc.^{86,87} Several methods have been investigated to increase the catalytic activity of UiO-66. One strategy is to create more open metal sites by defect engineering. Vermoortele et al. reported the synthesis of UiO-66 by using trifluoroacetic acid and HCl in the synthesis.⁸⁶ After dehydroxylation of the Zr_6 clusters and removal of the coordinated trifluoroacetic acid by thermal activation, a material with more defects and therefore more open metal sites can be generated (Figure

I-9). Another method to increase the catalytic activity is to introduce functionalized organic ligands. Using molecular modeling, Vermoortele et al. revealed that the presence of nitro-substituted BDC ligands can increase the rate of cyclization of (+)-citronellal to isopulegol as a result of the electron-withdrawing effect.⁸⁷ The substituents can not only affect the Lewis acidic properties of the MOF but also introduce stabilizing or destabilizing effects on the reactants based on their electronic properties.

1.2.2 Brønsted Acid Catalysis

Besides the inherent Lewis acidic sites, stable MOFs can be functionalized with Brønsted acid catalysts to extend the scope of catalytic reactions. Recently, stable MOFs with Brønsted acids have been investigated for various reactions including the Diels-Alder reaction,⁸⁸ acetalization,⁸⁹ isomerization,^{88, 90} Friedel-Craft reaction,^{90, 91} esterification,⁹² and dehydration.⁹³ One strategy to introduce Brønsted acids into MOFs is to covalently bind Brønsted acidic groups to organic ligands. For example, MIL-53(Cr) and MIL-101(Cr) functionalized with sulfonic acid can be obtained by treating with triflic anhydride and sulfuric acid.⁹² They showed high catalytic performance in esterification of *n*-butanol with acetic acid. The turnover frequency for sulfated MIL-53 (Cr) (0.72 min^{-1}) was higher than that of acidic polymers like Nafion NR50 (0.63 min^{-1}). In another example, Lewis acidity and Brønsted acidity coexist in the sulfated MOF-808.⁹⁰ Substitution of terminal ligands on Zr_6 -clusters with sulfate groups in a 2:1 ratio in MOF-808 forms a super acidic sulfated framework with both Lewis acidity and Brønsted acidity (Figure I-10). The sulfated MOF-808 showed activity for isomerization of methylcyclopentane at $150 \text{ }^\circ\text{C}$, which represents the benchmark for MOF-based solid-acid catalysts. It is also worth noting that Brønsted acid catalysis requires a highly stable MOF platform. The catalytic process generally involves the transfer of protons from the catalytic active sites of the MOF to the substrate, which requires the MOF to be stable toward protons. As a result, compared to the large amount of MOFs explored for Lewis acidic catalysis, only a limited number of MOFs as Brønsted acidic catalysts have thus far been developed.

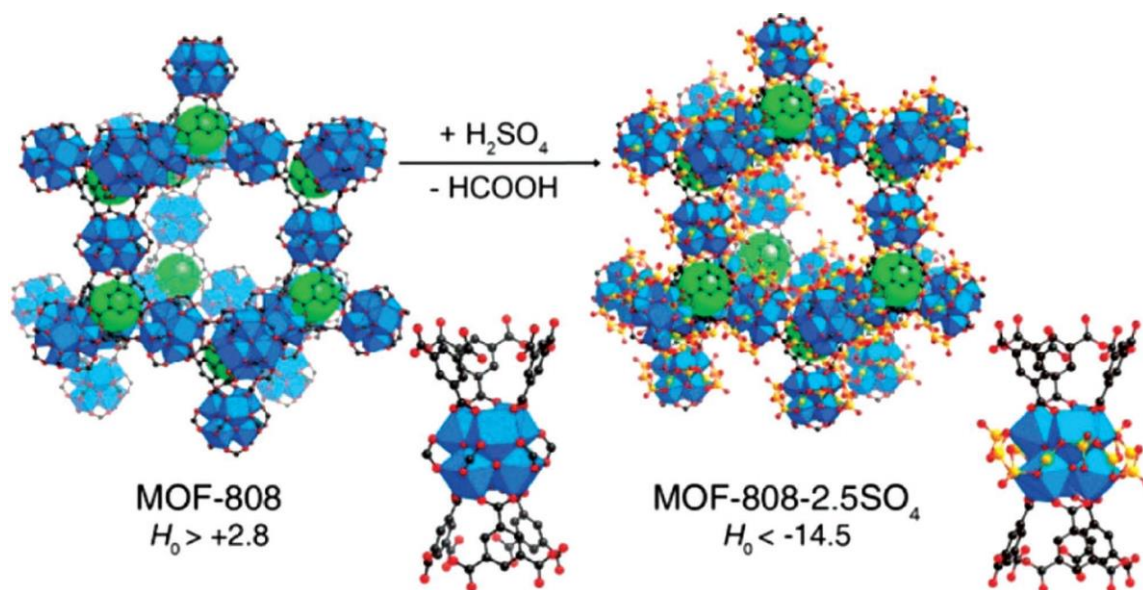


Figure I-10 The preparation of sulfated MOF-808 with both Lewis acidity and Bronsted acidity. Reprinted with permission from Ref. 90 copyright © 2014 American Chemical Society.

1.2.3 Redox Catalysis

Functionalized linkers as catalysts. The redox inertness of some stable MOFs (such as Al^{3+} and Zr^{4+} -based MOFs) limited their applications as redox catalysts. To functionalize stable MOFs for redox catalysis, one method is to adopt metallo-linkers. For example, PCN-222 with different metalloporphyrins were employed as biomimetic oxidation catalysts. Three substrates, including pyrogallol, 3,3,5,5-tetramethylbenzidine, and *o*-phenylenediamine, were adopted to estimate the catalytic activity of PCN-222(Fe). Kinetic studies have demonstrated that PCN-222(Fe) can catalyze the oxidation of a variety of substrates, acting as an effective peroxidase mimic with both excellent substrate binding affinity (K_m) and catalytic activity (k_{cat}), superior to free hemin in aqueous media. The excellent catalytic performance of PCN-222(Fe) is attributed to the stability of the framework and the large open channels, which effectively prevent the self-dimerization of porphyrin centers and facilitate the diffusion of substrates. In another example, UiO-66 was modified with molybdenum, tungsten, and vanadium for olefin epoxidation. Tan and co-workers functionalized the UiO-66-NH₂ with salicylaldehyde, pyridine-2-aldehyde, or 2-pyridine chloride by PSM and then metalated the linker with Mo(IV) catalyst.⁹⁴ The good dispersion of the Mo(IV) catalyst and the highly accessible surface area of the MOF guarantee sufficient contact between the substrate and catalytic center, facilitating the catalytic reaction. The Mo(IV)-functionalized MOFs exhibit high catalytic activity for epoxidation reactions with a conversion of 99%. In addition, Lin and co-workers constructed a series of Zr-MOFs (BPV-MOF, mBPV-MOF, and mPT-MOF) of **fcu** topology with elongated bipyridyl- and phenanthryl- containing linkers.⁹⁵ Postsynthetic

metalation of these Zr-MOFs with $[\text{Ir}(\text{COD})(\text{OMe})]_2$ afforded highly active, robust single-site catalysts for organic transformation reactions including tandem hydrosilylation/ortho-silylation of aryl ketones and aldehydes, tandem dehydrocoupling/ortho-silylation of *N*-methylbenzyl amines, and borylation of aromatic C-H bonds.

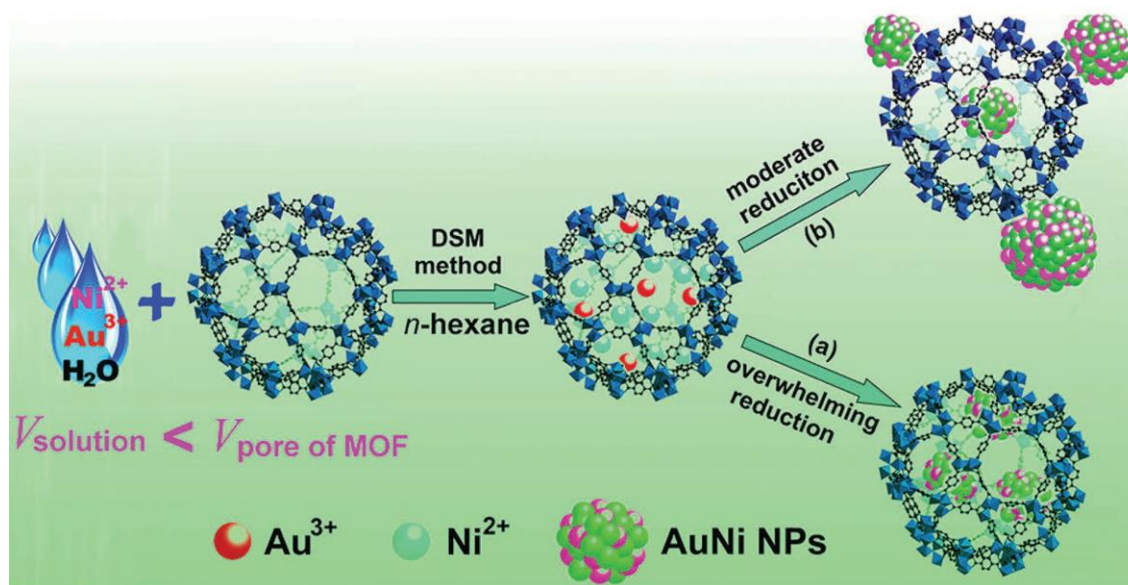


Figure I-11 Schematic representation of the immobilization of AuNi nanoparticles by the MIL-101 matrix using DSM combined with a liquid-phase CCR strategy. Reproduce with permission from Ref. 99 copyright © 2013 American Chemical Society.

Encapsulated catalysts: Besides the functionalization of linkers, redox catalysts can also be incorporated into the cavity of MOFs.⁹⁶ Noble metal nanoparticles are known as efficient catalysts with a wide range of potential applications in the fields of energy conversion and storage, environmental remediation, drug research, and chemical production. Immobilization of metal nanoparticles in MOF cavity provides highly accessible metal surfaces while preventing aggregation. Noble metal nanoparticles can be introduced into MOFs by impregnation and successive reduction.⁹⁷ Metal alloy nanoparticles were also successfully embedded in the cavity of MOFs by Xu and co-

workers. In 2011, they reported bimetallic AuPd NPs immobilized in MIL-101 and ethylenediamine (ED)-grafted MIL-101 (ED-MIL-101) as highly active catalysts for the conversion of formic acid to high-quality hydrogen at a convenient temperature.⁹⁸ Later on, they developed a liquid-phase concentration controlled reduction (CCR) strategy in combination with the double solvents method (DSM) to introduce AuNi nanoparticles into MOFs and control the size and location of the immobilized AuNi nanoparticles (Figure I-11).⁹⁹ Uniformly distributed AuNi nanoparticles encapsulated in the pores of MIL-101 were achieved which exerted high activity for hydrogen generation from the catalytic hydrolysis of ammonia borane.

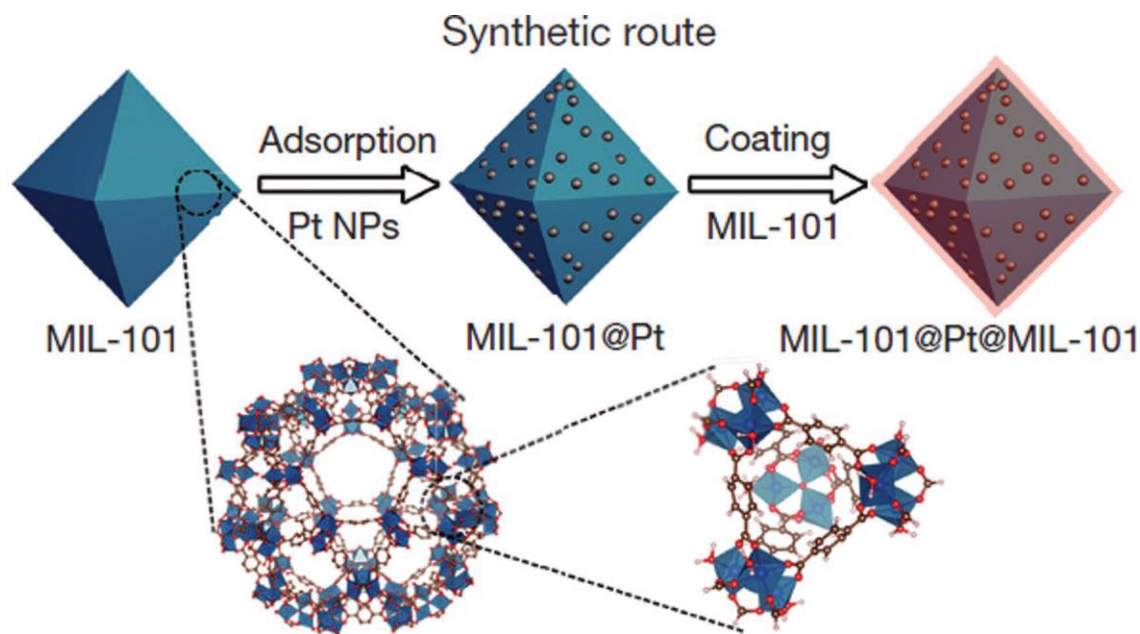


Figure I-12 Illustration of the synthetic route to generate MIL-101@Pt@MIL-101, comprised of Pt nanoparticles (NPs) sandwiched between a core and a shell of MIL-101. Reproduced with permission from Ref. 100 copyright © 2016 American Association for the Advancement of Science.

In 2016, Tang and co-workers reported a MOF@Pt NP@MOF composite as an efficient catalyst for selective hydrogenation of α , β -unsaturated aldehydes (Figure I-

12).¹⁰⁰ Sandwiching platinum nanoparticles between an inner core and an outer shell composed of MIL-101 (Fe), MIL-101(Cr), or both resulted in stable catalysts that convert a range of α , β -unsaturated aldehydes with high yield and selectivity toward unsaturated alcohols. Calculations revealed that preferential interaction of MOF metal sites with the carbon-oxygen rather than the carbon-carbon group explains the selective hydrogenation of aldehydes instead of alkenes.

1.2.4 Photocatalysis

Photocatalysis is a promising pathway for the direct conversion of solar energy to clean and valuable chemical energy.^{101, 102} MOFs can be photoresponsive through light absorption by the organic linkers or the metal centers, attracting great interest as fascinating catalysts in this field.

Ti-based MOFs, with photoactive Ti-oxo clusters, have been exclusively studied as promising photocatalysts. A reversible photochromic behavior of MIL-125(Ti) induced UV irradiation in alcohol was initially observed by Férey and co-workers.¹⁰³ Later, Li and co-workers fabricated an NH₂-functionalized MIL-125, namely MIL-125-NH₂,¹⁰⁴ which not only possesses extra light absorption in the visible light region but also exhibits enhanced adsorption capacity toward CO₂. Recent work has demonstrated that MIL-125-NH₂ can work as a light-driven photocatalyst for hydrogen generation¹⁰⁵ and CO₂ reduction.¹⁰⁴ In 2015, our group assembled the photocatalytic titanium-oxo cluster and photosensitizing porphyrinic linker into a MOF named PCN-22.¹⁰⁶ As a suitable candidate for light harvesting, PCN-22 was employed as a photocatalyst for an alcohol oxidation reaction.

Garcia and co-workers initially studied the photocatalytic activity of water stable Zr-MOFs (UiO-66 and UiO-66-NH₂) for H₂ generation in methanol or water/methanol upon irradiation at wavelengths longer than 300 nm.¹⁰⁷ The presence of the NH₂ group in the BDC fragment induces the absorption in the wavelength longer than 300 nm due to the auxochromic and bathochromic shift, which renders UiO-66-NH₂ a better photocatalyst than UiO-66. UiO-66-NH₂ also exhibits high photocatalytic activity for the

aerobic oxidation and CO₂ reduction under visible-light irradiation.^{108, 109} Pt nanoparticles were later incorporated inside of or supported on UiO-66-NH₂ as cocatalysts for photocatalytic hydrogen production.¹¹⁰ The Zr-porphyrin MOFs, PCN-222 and MOF-525, were also investigated as photocatalysts for CO₂ reduction.^{111, 112}

Compared with conventional inorganic semiconductors, it is easier to control the light-absorption properties of MOFs by tuning the light-absorption abilities of organic fragments. For instance, the introduction of NH₂ groups as substituents on ligands would result in an isostructural MOF with a new band in the visible region.¹¹³ The introduction of specific chromophores, such as porphyrin fragments, can lead to the formation of MOFs with photoresponsive characteristics derived from the corresponding chromophores. Considering the high tunability of MOFs by judicious selection of metal-oxo clusters and design of linkers, a variety of MOF based catalysts for specific applications are envisioned.

1.3 Introduction to Porous Polymer Network for Carbon Capture

1.3.1 Technologies/Methods and Challenges in CO₂ Capture

Industrial generation of greenhouse gas CO₂ from power plants using fossil fuels and biomass has an enormous impact on the global climate and environment. In order to mitigate CO₂ release, one particularly effective approach is to selectively capture CO₂ from flue gas. In coal-fired power plants, flue gas is typically composed of nitrogen (~74%), CO₂ (~12%), water vapor (~12%), and various concentrations of other minor components including oxygen, nitrogen oxides (NO_x), and sulfur oxides (SO_x). Of the many post-combustion carbon capture strategies that have emerged, the only deployed technology in the industry is amine scrubbing. In essence, the process involves the absorption of CO₂ into an aqueous solution of amine with low volatility at ambient temperature and regeneration of amine by stripping with water vapor at 100 °C to 120 °C. While amine scrubbing can achieve CO₂ capture from flue gas with efficiency up to 98%, it suffers from high parasitic energy consumption of over 30%. Moreover, SO_x and NO_x oxidize the amine absorbent thereby reducing its lifetime. The caustic nature of amine absorbent also places a burden on its container and has adverse environmental impact.¹¹⁴

115

The technologies and methods used in CO₂ separation are illustrated schematically in Figure I-13; in each case, except for cryogenic separation, different materials are required as the carriers. Absorption is a well-established CO₂ separation approach used in the chemical and petroleum industries today. It falls into two categories: a) physical, which is temperature and pressure dependent (absorption occurs at high pressures and low

temperatures) and b) chemical, where absorption of CO₂ depends on the acid-base neutralization reaction.¹¹⁶ Some of the explored solvents are amines (such as monoethanolamine or MEA), ammonia solutions, Selexol, Rectisol, fluorinated solvents, and ionic liquids.

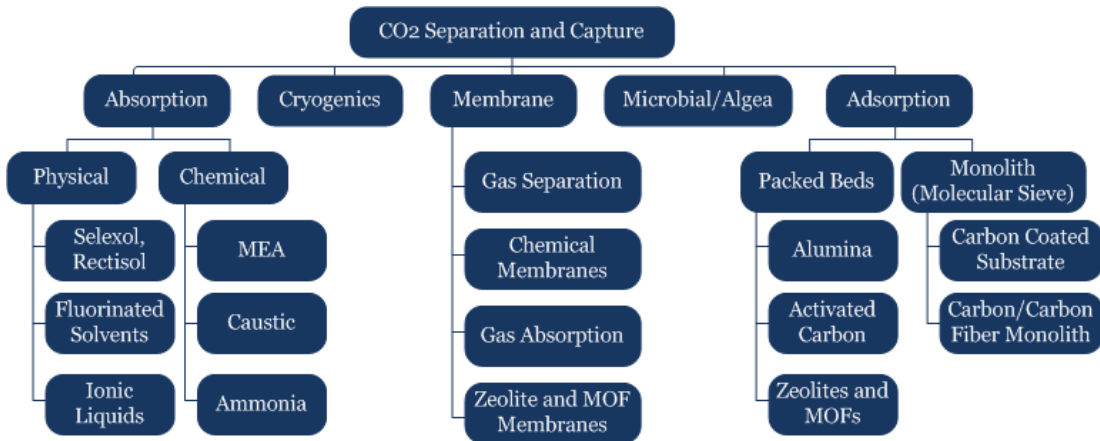


Figure I-13 Different technologies and materials for CO₂ separation and capture.

Membrane-based separation relies on the differences in physical and/or chemical interactions between gases and the membrane material, which can be modified to allow some components to pass preferentially through the membrane based on size (kinetic) and/or affinity (thermodynamics). Inorganic ceramic membranes and organic polymeric membranes have been used in CO₂ separation from flue gas in post-combustion.¹¹⁷ However, reaching a high degree of CO₂ separation by using single-stage ceramic or polymeric membrane is difficult. New materials are still required to achieve the desired effect in CO₂ separation by membranes. In addition, the potential impact of minor air pollutants in real flue gases on the membrane system performance has not been fully investigated yet. To simultaneously achieve 90% capture and 95% product purity for CO₂, it is necessary to add a two-stage membrane system to a pulverized coal power plant

however, this approach nearly doubles the plant cost of electricity and incurs a high energy penalty up to 30% of the gross electrical output. These limitations would need to be addressed to enhance the viability of membrane technology.¹¹⁸

Gas separation based on adsorption in which the selection of a sound adsorbent is the key for specific separation has been well developed. Despite the establishment of the field and a diverse range of useful sorbents are available for CO₂ separation, there is still much to be done to optimize the performance of these materials and investigate a wider range of new sorbents. These adsorbents can then be combined with a broad range of process options yielding a wide variety of opportunities for the optimization of separation performance. Conventional solid adsorbents include activated carbons, silica gel, ion-exchange resins, zeolites, mesoporous silicates, activated alumina, metal oxides, and other surface-modified porous media. In recent years, new types of adsorbents such as metal-organic frameworks (MOFs) and porous polymer networks (PPNs) have been developed for gas separation. The challenges that arise in the development of these materials and techniques lie in being able to transfer and scale the technology from the lab to the harsh conditions that it will be subjected to while maximizing efficiency and minimizing costs.

1.3.2 CO₂ Capture by Traditional Sorbents/Advanced Sorbents (PPNs)

CO₂ capture by traditional sorbents such as carbonaceous materials and crystalline inorganic materials such as zeolites is much more energy-efficient as compared to aqueous amine solutions. This is due to the absence of the formation of new chemical bonds between the sorbate and sorbent, thereby requiring significantly less energy for regeneration. In addition, the heat capacities of sorbents are only a fraction of that of the amine solution.¹¹⁹ However, the traditional carbonaceous materials (such as activated carbon and charcoal) are limited by low CO₂/N₂ selectivity (*ca.* 10), while zeolites suffer from impaired performance in the presence of water.¹²⁰ Therefore, there is an urgent need to develop advanced sorbents with excellent CO₂/N₂ selectivity, high CO₂ capacity, and enduring performance under flue gas conditions.

PPNs are composed predominantly of carbon, boron, oxygen, and nitrogen that are connected through strong covalent bonds. The major advantages of PPNS over other porous materials are exceptional porosity, ultra-high surface area, and generally superior physicochemical stability, the combination of which enables an enormous scope of post-synthetic modifications to introduce specific chemical functionalities. PPNS can generally be handled and functionalized under standard wet chemical reaction conditions without significant degradation of the framework or loss of porosity, and are ideal for applications in capturing CO₂ from harsh flue gas conditions.^{121, 122} Although PPNS have been widely studied for CO₂ capture, their application has been hampered by low CO₂ loading and CO₂/N₂ selectivity due to the lack of strong CO₂ binding sites in the frameworks. Thus, the introduction of CO₂-philic groups in PPNS through post-synthetic modification is

expected to greatly enhance the CO₂ loading capacity and CO₂/N₂ selectivity.¹²³ In this regard, amine-tethered PPNs (aPPNs) for low-energy selective capture of CO₂ have been developed.

“Wet scrubbing”, the current CO₂ capture process, suffers from a series of inherent problems, such as high regeneration costs that arise from heating the solution (*ca.* 30% of parasitic power consumption), fouling of the equipment, and solvent boil-off. To address these issues, solid adsorbents functionalized with amines can be used as substitutes for aqueous amines, reducing energetic penalty and the loss of amines throughout the processes. In this case, the working capacity of sorbents is in positive correlation with amine density. Intuitively, the higher surface area of the support media, the higher the potential amine density. To take on the challenge of maximizing CO₂ working capacity, researchers developed a series of PPNs with exceptionally high surface area and properties ideal for post-synthetic amine incorporation^{124, 125} (Figure I-14a). Among them, PPN-4 has a Brunauer-Emmett-Teller (BET) surface area of 6461 m²g⁻¹, the highest value of all organic porous materials reported so far. Moreover, our PPNs have shown excellent physiochemical stability, even toward moisture, which has historically hindered the use of advanced porous materials in industrial applications. Also importantly, the introduction of functionalities is feasible because aromatic rings are known for their susceptibility to organic reactions, such as electrophilic aromatic substitutions. Indeed, we have successfully incorporated alkyl amines into our PPNs via post-synthetic modification (Figure I-14b) and carried out preliminary studies of aPPNs for CO₂ capture. Moreover, we have successfully developed a truly cost-effective synthesis of amine-tethered porous

materials for carbon capture.¹²⁶ PPN-125 was synthesized *via* Ni(COD)₂-free coupling reaction between 1,3,5-trihydroxybenzene and terephthalaldehyde to introduce phenol groups, which can be used as anchors to introduce amine chains as shown in Figure I-14c.

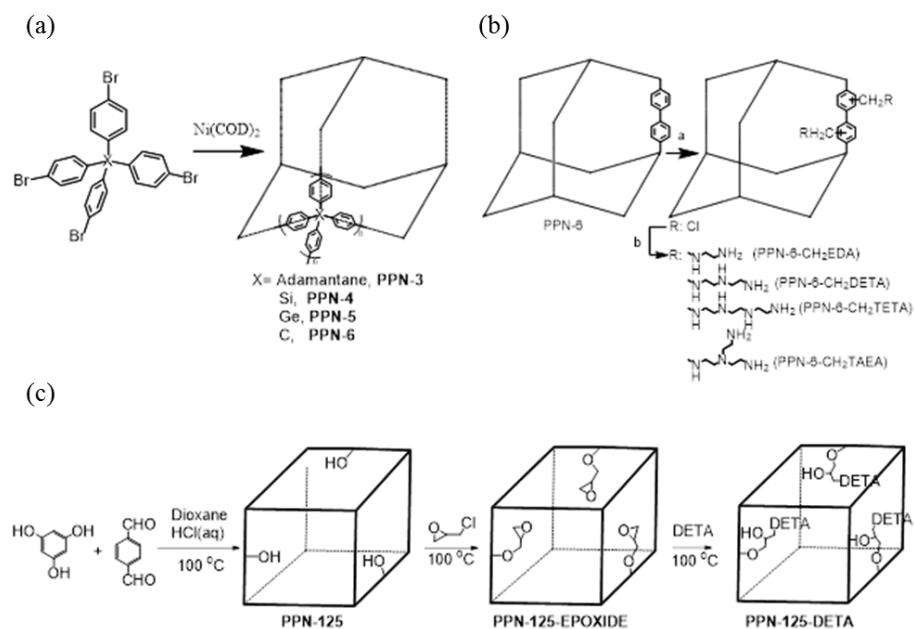


Figure I-14 The synthetic routes of (a) PPN-3, 4, 5, 6, (b) amine-tethered PPN-6 and (c) synthesis and amine-incorporation of PPN-125.

CHAPTER II

ONE-STEP SYNTHESIS OF HYBRID CORE-SHELL METAL-ORGANIC FRAMEWORKS²

2.1 Introduction

Metal-Organic Frameworks (MOFs), also known as Porous Coordination Polymers (PCPs), are an emergent class of crystalline porous materials, which have received considerable attention in the past two decades.^{4, 127-131} Due to their structural and functional tunability as well as their ever-expanding scope of application, MOFs have become one of the most intriguing classes of materials for both scientists and engineers. The high porosity, exceptional tunability, and adequate stability of MOFs make them promising candidates for many potential applications including gas storage¹³²⁻¹³⁵ and separation^{16, 136-139}, heterogeneous catalysis^{40, 42, 95, 140, 141}, sensing¹⁴²⁻¹⁴⁵, proton conduction^{146, 147}, luminescence¹⁴⁸⁻¹⁵⁰, and drug delivery.^{60, 151-154} Therefore, an expanding variety of strategies have been applied to introduce desired functionalities into MOFs. Among them, one-pot synthesis has been extensively utilized due to the convenience of incorporating multi-functionalities in a single step while preserving the structural integrity.^{155, 156} Yaghi and coworkers put forward the important concept of “heterogeneity within order”. This idea was exemplified by multivariate MOFs (MTV-MOFs), in which mixed ligands with as many as eight different substituents were introduced into MOF-5.¹⁵⁵

² Reproduced with permission from: Yang, X.; Yuan, S.; Zou, L.; Drake, H.; Zhang, Y.; Qin, J.; Alsalme, A.; Zhou, H.-C. “One-Step Synthesis of Hybrid Core-Shell Metal-Organic Frameworks” *Angew. Chem.* **2018**, *130*, 3991–3996. Copyright 2018 by Wiley-VCH Verlag GmbH & Co. KGaA, Weinheim.; Feng, D.; Gu, Z.-Y.; Li, J.-R.; Jiang, H.-L.; Wei, Z.; Zhou, H.-C. “Zirconium-Metalloporphyrin PCN-222: Mesoporous Metal-Organic Frameworks with Ultrahigh Stability as A Biomimetic Catalyst” *Angew. Chem. Int. Ed.*, **2012**, *51*, 10307–10310. Copyright 2012 by Wiley-VCH Verlag GmbH & Co. KGaA, Weinheim.

Post-synthetic modification (PSM) is another powerful tool for MOF functionalization.¹⁵⁷⁻¹⁶¹ With the PSM approach, both metal nodes and organic linkers can be functionalized without significantly compromising the overall structural integrity. This approach is adopted to build topologically identical but functionally diverse frameworks. Furthermore, the complexity can also be enhanced by encapsulating other materials to form MOF composites that combine the advantages of both.¹⁶²⁻¹⁶⁸ Recently, Tang and coworkers synthesized a series of MOF composites by incorporating Pt nanoparticles into MIL-101 to serve as an efficient catalyst for the selective hydrogenation of α , β -unsaturated aldehydes.¹⁶⁹

The complexity of MOF materials can be further escalated by the core-shell strategy to combine the functionalities of both MOFs.¹⁷⁰⁻¹⁷³ The core-shell MOF self-assembly method was demonstrated by Kitagawa and coworkers in the synthesis of Cu-based MOFs on a substrate of Zn counterpart. Another representative example was reported by Rosi and coworkers who prepared bio-MOF-11@bio-MOF-14 composite by stepwise synthesis strategy. This composite exhibited higher CO₂/N₂ selectivity and water stability than bio-MOF-11.¹⁷³ Another example was given by Oh and coworkers who reported two MOF-templated core-shell composites, MIL-68@MIL-68-Br and MIL-68@MIL-68-NDC, in which the secondary MOF showed different growth directions.¹⁷⁰

Herein, we demonstrate that hybrid core-shell MOFs with mismatching lattices can be synthesized under the guidance of nucleation kinetic analysis. A series of MOF composites with mesoporous core and microporous shell were constructed and characterized by optical microscopy, powder X-ray diffraction, gas sorption measurement,

and scanning electron microscopy. Isoreticular expansion of microporous shells and orthogonal modification of the core was realized to produce multifunctional MOF composites, which acted as size selective catalysts for olefin epoxidation with high activity and selectivity.

2.2 Experimental Section

2.2.1 Materials and Instrumentation

2.2.1.1 Materials

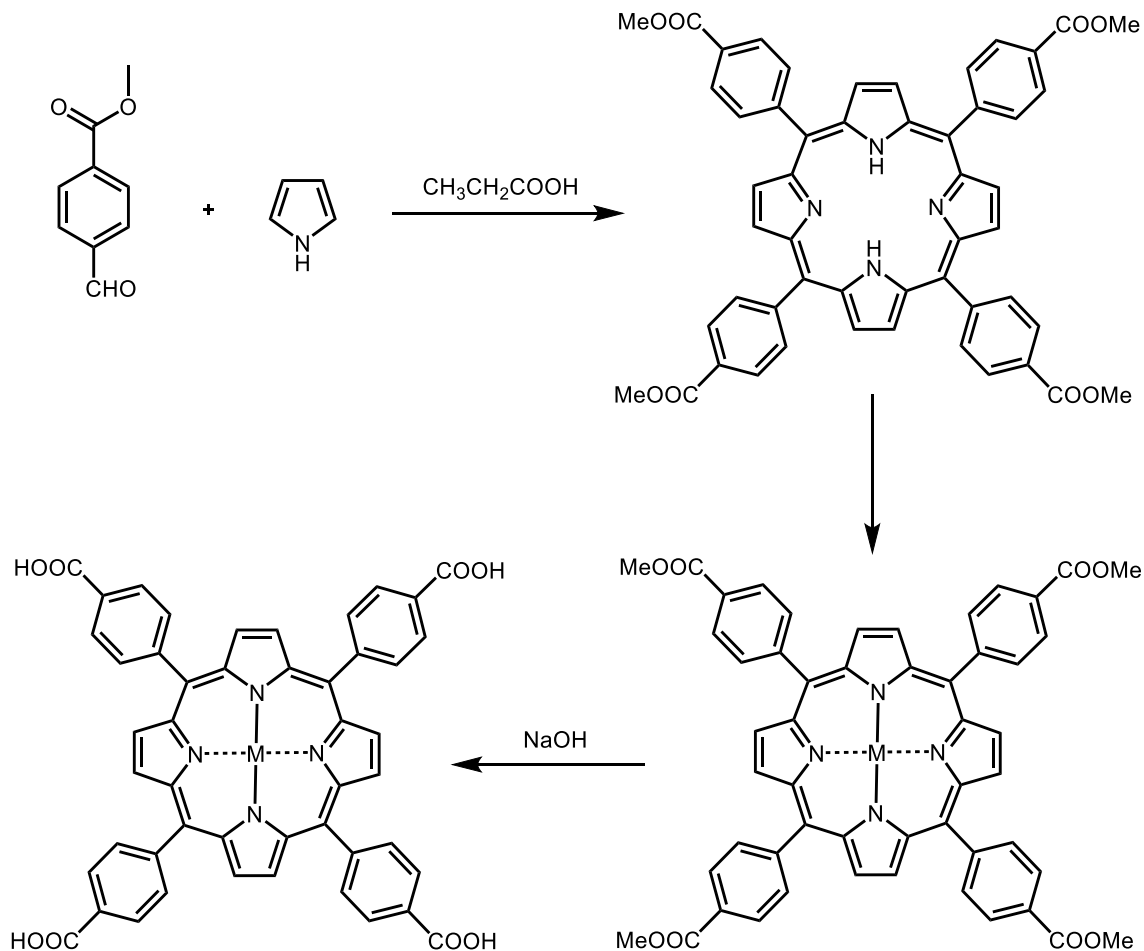
Methyl 4-formylbenzoate was purchased from Oakwood Products. Inc. Pyrrole, propionic acid, *N,N*-dimethylformamide (DMF), trifluoroacetic acid (TFA), acetone, iron(II) chloride tetrahydrate ($\text{FeCl}_2 \cdot 4\text{H}_2\text{O}$), manganese(II) chloride tetrahydrate ($\text{MnCl}_2 \cdot 4\text{H}_2\text{O}$), nickel (II) chloride hexahydrate ($\text{NiCl}_2 \cdot 6\text{H}_2\text{O}$), and zinc (II) chloride (ZnCl_2 , anhydrous) were from Alfa Aesar. 5,10,15,20-Tetrakis(4-methoxycarbonylphenyl)porphyrin (TPPCOOMe) was prepared according to procedures described in next section. All commercial chemicals were used without further purification unless otherwise mentioned.

2.2.1.2 Instrumentation

Powder X-ray diffraction (PXRD) measurements were carried out on a BRUKER D8-Focus Bragg-Brentano X-ray Powder Diffractometer equipped with a Cu sealed tube ($\lambda = 1.54178 \text{ \AA}$) at 40 kV and 40 mA. Nuclear magnetic resonance (NMR) data were collected on a Mercury 300 spectrometer. Gas sorption measurements were conducted on a Micromeritics ASAP 2020 system. Fourier transform infrared (FT-IR) measurements were performed on a SHIMADU IR Affinity-1 spectrometer. Scanning electron microscope (SEM) was performed on QUANTA 450 FEG.

2.2.2 Ligand Synthesis

The tetrakis(4-carboxyphenyl)porphyrin (H_2TCPP) ligand and other metal-involved TCPP (M-TCPP) ligands were synthesized based on previous reports with modifications. Typically, we obtained them by three steps as follows:



Scheme II-1 Synthesis strategy for H_2TCPP and M-TCPP.

2.2.2.1 5,10,15,20-Tetrakis(4-methoxycarbonylphenyl)porphyrin (TPPCOOMe)

To refluxed propionic acid (100 mL) in a 500-mL three necked flask were added pyrrole (3.0, 0.043 mol) and methyl p-formylbenzoate (6.9 g, 0.042 mol), and the solution

was refluxed for 12h in darkness. After the reaction mixture was cooled to room temperature, crystals were collected by suction-filtration to afford purple crystals (1.9g, 2.24mmol, 21.3% yield). ^1H NMR (300 MHz, CDCl_3) δ 8.81 (s, 8H), 8.43 (d, 8H), 8.28 (d, 8H), 4.11 (s, 12H), -2.83 (s, 2H).

2.2.2.2 [5,10,15,20-Tetrakis(4-methoxycarbonylphenyl)porphyrinato]-Fe(III)

Chloride (FeTPPCOOMe)

A solution of TPP-COOMe 0.854 g (1.0 mmol) and $\text{FeCl}_2 \cdot 4\text{H}_2\text{O}$ (2.5 g, 12.8 mmol) in 100 mL of DMF was refluxed for 6 h. After the mixture was cooled to room temperature, 150 mL of H_2O was added. The resultant precipitate was filtered and washed with 50 mL of H_2O for two times. The obtained solid was dissolved in CHCl_3 , followed by washing three times with 1 M HCl and twice with water. The organic layer was dried over anhydrous magnesium sulfate and evaporated to afford quantitative dark brown crystals.

2.2.2.3 [5,10,15,20-Tetrakis(4-methoxycarbonylphenyl)porphyrinato]-Mn(III)

Chloride (MnTPPCOOMe)

A solution of TPP-COOMe 0.854 g (1.0 mmol) and $\text{MnCl}_2 \cdot 4\text{H}_2\text{O}$ (2.5 g, 12.8 mmol) in 100 mL of DMF was refluxed for 6 h. After the mixture was cooled to room temperature, 150 mL of H_2O was added. The resultant precipitate was filtered and washed with 50 mL of H_2O for two times. The obtained solid was dissolved in CHCl_3 , followed by washing three times with water. The organic layer was dried over anhydrous magnesium sulfate and evaporated to afford quantitative dark green crystals.

2.2.2.4 [5,10,15,20-Tetrakis(4-methoxycarbonylphenyl)porphyrinato]-Ni(II) (NiTPPCOOMe)

A solution of TPPCOOMe 0.854 g (1.0 mmol) and NiCl₂·6H₂O (3.1 g, 12.8 mmol) in 100 mL of DMF was refluxed for 6 h. After the mixture was cooled to room temperature, 150 mL of H₂O was added. The resultant precipitate was filtered and washed with 50 mL of H₂O for two times. The obtained solid was dissolved in CHCl₃, followed by washing three times with 1 M HCl and twice with water. The organic layer was dried over anhydrous magnesium sulfate and evaporated to afford quantitative crimson crystals.

2.2.2.5 [5,10,15,20-Tetrakis(4-methoxycarbonylphenyl)porphyrinato]-Zn(II) (ZnTPPCOOMe)

A solution of TPPCOOMe 0.854 g (1.0 mmol) and ZnCl₂ (1.75 g, 12.8 mmol) in 100 mL of DMF was refluxed for 6 h. After the mixture was cooled to room temperature, 150 mL of H₂O was added. The resultant precipitate was filtered and washed with 50 mL of H₂O for two times. The obtained solid was dissolved in CHCl₃, followed by washing three times with water. The organic layer was dried over anhydrous magnesium sulfate and evaporated to afford quantitative violet crystals.

2.2.2.6 [5,10,15,20-Tetrakis(4-carboxyphenyl)porphyrinato]-Fe(III) Chloride (TCPP(Fe))

The obtained ester (0.75 g) was stirred in THF (25 mL) and MeOH (25 mL) mixed solvent, to which a solution of KOH (2.63 g, 46.95 mmol) in H₂O (25 mL) was introduced. This mixture was refluxed for 12 h. After cooling down to room temperature, THF and

MeOH were evaporated. Additional water was added to the resulting water phase and the mixture was heated until the solid was fully dissolved, then the homogeneous solution was acidified with 1M HCl until no further precipitate was detected. The brown solid was collected by filtration, washed with water and dried in vacuum.

2.2.2.7 [5,10,15,20-Tetrakis(4-carboxyphenyl)porphyrinato]-Mn(III) Chloride (TCPP(Mn))

The obtained ester (0.75 g) was stirred in THF (25 mL) and MeOH (25 mL) mixed solvent, to which a solution of KOH (2.63 g, 46.95 mmol) in H₂O (25 mL) was introduced. This mixture was refluxed for 12 h. After cooling down to room temperature, THF and MeOH were evaporated. Additional water was added to the resulting water phase and the mixture was heated until the solid was fully dissolved, then the homogeneous solution was acidified with 1M HCl until no further precipitate was detected. The dark green solid was collected by filtration, washed with water and dried in vacuum.

2.2.2.8 [5,10,15,20-Tetrakis(4-carboxyphenyl)porphyrinato]-Ni(II) (TCPP(Ni))

The obtained ester (0.75 g) was stirred in THF (25 mL) and MeOH (25 mL) mixed solvent, to which a solution of KOH (2.63 g, 46.95 mmol) in H₂O (25 mL) was introduced. This mixture was refluxed for 12 h. After cooling down to room temperature, THF and MeOH were evaporated. Additional water was added to the resulting water phase and the mixture was heated until the solid was fully dissolved, then the homogeneous solution was acidified with 1M HCl until no further precipitate was detected. The crimson solid was collected by filtration, washed with water and dried in vacuum.

2.2.2.9 [5,10,15,20-Tetrakis(4-carboxyphenyl)porphyrinato]-Zn(II) (TCPP(Zn))

The obtained ester (0.75 g) was stirred in THF (25 mL) and MeOH (25 mL) mixed solvent, to which a solution of KOH (2.63 g, 46.95 mmol) in H₂O (25 mL) was introduced. This mixture was refluxed for 12 h. After cooling down to room temperature, THF and MeOH were evaporated. Additional water was added to the resulting water phase and the mixture was heated until the solid was fully dissolved, then the homogeneous solution was acidified with 1M HCl until no further precipitate was detected. The violet solid was collected by filtration, washed with water and dried in vacuum.

2.2.3 MOF Synthesis

2.2.3.1 Synthesis of PCN-222/PCN-222(Fe)@Zr-NDC

ZrCl₄ (130 mg), NDC (100 mg), TCPP/TCPP(Fe) (10 mg), trifluoroacetic acid (2.5 ml) and DMF (15 ml) were charged in a Pyrex vial. The mixture was heated in 120 °C oven for 7 days. After cooling down to room temperature, the crystals of PCN-222/PCN-222(Fe)@Zr-NDC were harvested.

2.2.3.2 Synthesis of PCN-222/PCN-222(Fe)@Zr-BPDC

ZrCl₄ (130 mg), BPDC (100 mg), TCPP/TCPP(Fe) (10 mg), trifluoroacetic acid (2.5 ml) and DMF (15 ml) were charged in a Pyrex vial. The mixture was heated in 120 °C oven for 7 days. After cooling down to room temperature, the crystals of PCN-222/PCN-222(Fe)@Zr-BPDC were harvested.

2.2.3.3 Synthesis of PCN-222/PCN-222(Fe)@Zr-BPYDC

ZrCl₄ (130 mg), BPYDC (100 mg), TCPP/TCPP(Fe) (10 mg), trifluoroacetic acid (2.5 ml) and DMF (15 ml) were charged in a Pyrex vial. The mixture was heated in 120 °C oven for 7 days. After cooling down to room temperature, the crystals of PCN-222/PCN-222(Fe)@Zr-BPYDC were harvested.

2.2.3.4 Synthesis of PCN-222/PCN-222(Fe)@Zr-BPDC-NO₂

ZrCl₄ (130 mg), BPDC-NO₂ (100 mg), TCPP/TCPP(Fe) (10 mg), trifluoroacetic acid (2.5 ml) and DMF (15 ml) were charged in a Pyrex vial. The mixture was heated in

120°C oven for 7 days. After cooling down to room temperature, the crystals of PCN-222/PCN-222(Fe)@Zr-BPDC-NO₂ were harvested.

2.2.3.5 Synthesis of PCN-222/PCN-222(Fe)@Zr-BPDC-I

ZrCl₄ (130 mg), BPDC-I (100 mg), TCPP/TCPP(Fe) (10 mg), trifluoroacetic acid (2.5 ml) and DMF (15 ml) were charged in a Pyrex vial. The mixture was heated in 120°C oven for 7 days. After cooling down to room temperature, the crystals of PCN-222/PCN-222(Fe)@Zr-BPDC-I were harvested.

2.2.3.6 Synthesis of PCN-222/PCN-222(Fe)@Zr-BPDC-OMe

ZrCl₄ (130 mg), BPDC-OMe (100 mg), TCPP/TCPP(Fe) (10 mg), trifluoroacetic acid (2.5 ml) and DMF (15 ml) were charged in a Pyrex vial. The mixture was heated in 120°C oven for 7 days. After cooling down to room temperature, the crystals of PCN-222/PCN-222(Fe)@Zr-BPDC-OMe were harvested.

2.2.3.7 Synthesis of PCN-222/PCN-222(Fe)@Zr-AZDC

ZrCl₄ (130 mg), AZDC (100 mg), TCPP/TCPP(Fe) (10 mg), trifluoroacetic acid (2.5 ml) and DMF (15 ml) were charged in a Pyrex vial. The mixture was heated in 120°C oven for 7 days. After cooling down to room temperature, the crystals of PCN-222/PCN-222(Fe)@Zr-AZDC were harvested.

2.3 Result and Discussion

To date, core-shell MOFs were mostly synthesized *via* a stepwise strategy in which the core was initially synthesized and subsequently used as a seed for the shell crystal growth. Lattice matching (similar crystallographic parameters) was usually required for the core-shell MOF crystal growth as the metal secondary building units (SBUs) of the core were aligned with those of the shell. However, the inconvenient stepwise synthesis and the strict lattice-matching requirement have limited the development of core-shell MOFs. To address this issue, we recently explored the one-pot synthesis of hybrid core-shell MOFs (PCN-222@Zr-BPDC) with mismatching lattices. The design and synthesis of hybrid core-shell MOFs were guided by nucleation kinetics (Figure II-1). Linkers with high connectivity (TCPP, H₄TCPP = tetrakis (4-carboxyphenyl)porphyrin) bind strongly with metal cations, allowing for fast homogeneous nucleation in solvothermal reaction conditions. In contrast, the low connectivity linkers (BPDC, BPDC = biphenyl-4,4'-dicarboxylate) usually take longer time to form crystals than TCPP under similar conditions. However, heterogeneous nucleation takes place far more quickly than homogenous ones since the seed crystal act as a template for the growth of the second MOF. The one-step approach thus eliminates the necessity of creating a new surface and reduces incipient surface energy requirements. Guided by kinetic control, PCN-222@Zr-BPDC(UiO-67) were synthesized by a solvothermal reaction of ZrCl₄ with H₄TCPP and H₂BPDC.

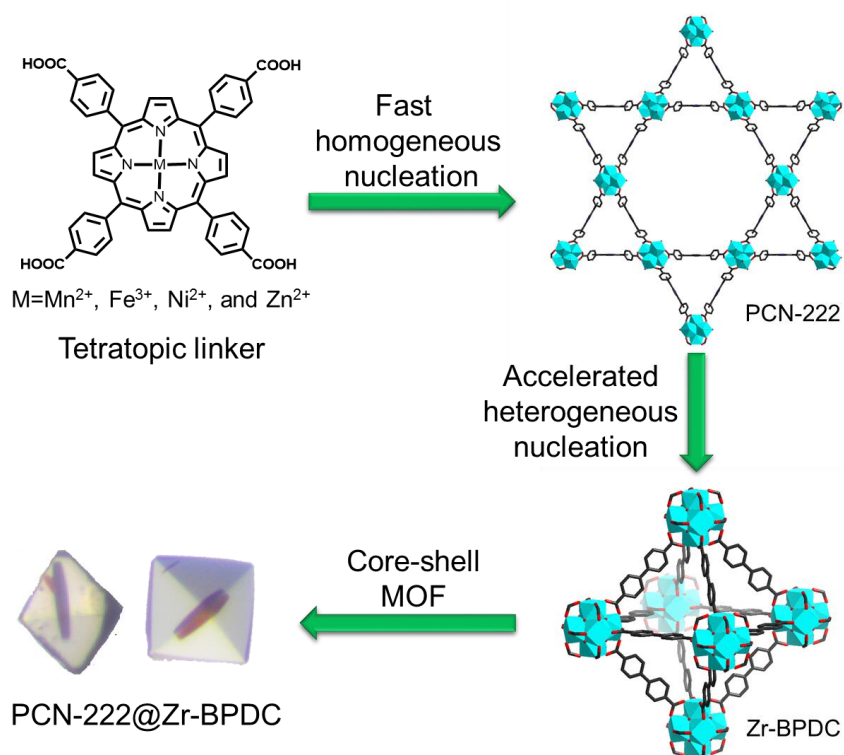


Figure II-1 Kinetically guided synthesis of a hybrid core-shell PCN-222@Zr-BPDC.

From the optical microscopic image (Figure II-2), the core and shell MOFs can clearly be distinguished. The cores consisted of red needle-shaped crystals and the shells were colorless bulk crystals. The SEM images (Figure II-3) from different cross sections also indicated a core-shell structure. The composition of the core-shell MOF was identified by powder X-ray diffraction (PXRD) patterns (Figure II-4). All characteristic peaks from both the PCN-222 and Zr-BPDC were found in the PXRD patterns, demonstrating that the core is composed of PCN-222 while the shell MOF have Zr-BPDC structures. The N₂ adsorption isotherm (Figure II-5) of the PCN-222@Zr-BPDC was very close to that of Zr-BPDC (UiO-67), but with a noticeable hysteresis loop around P/P₀ =

0.3 due to the presence of a small amount of PCN-222. In the pore size distribution plot (Figure II-6), mesopores of 3.2 nm were observed, which is characteristic of the mesoporous PCN-222. These results suggested that the mesopores of PCN-222 were not blocked in the core-shell structures.

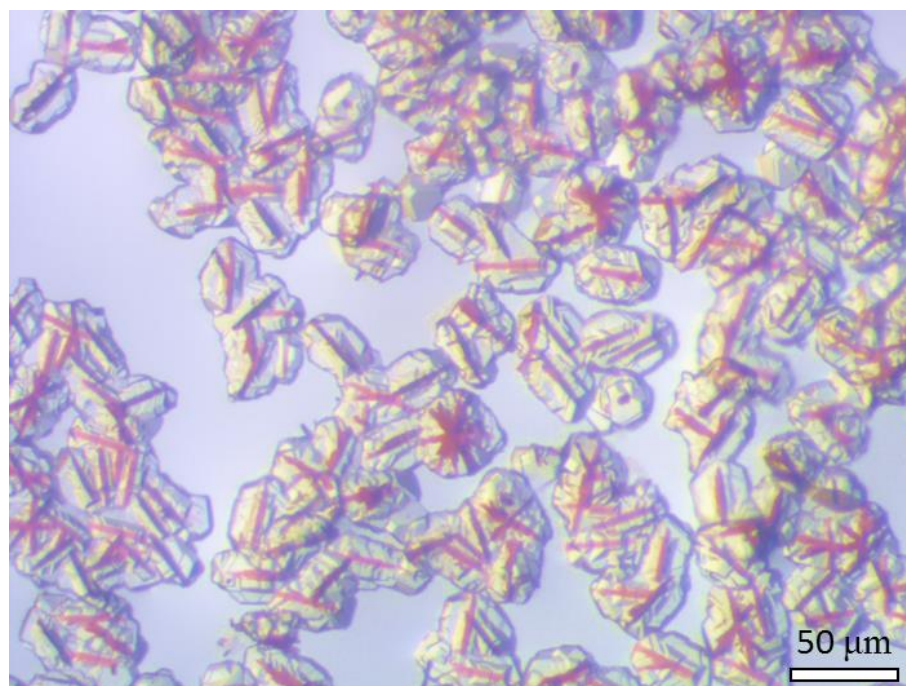


Figure II-2 Optical microscopic image of PCN-222@Zr-BPDC.

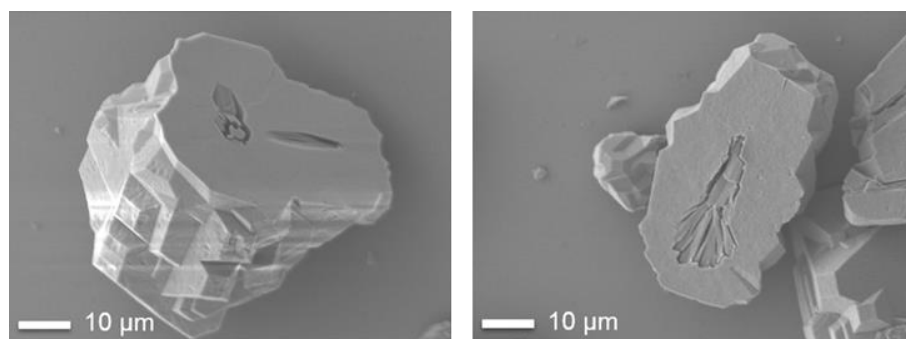


Figure II-3 SEM images of PCN-222@Zr-BPDC from different cross sections.

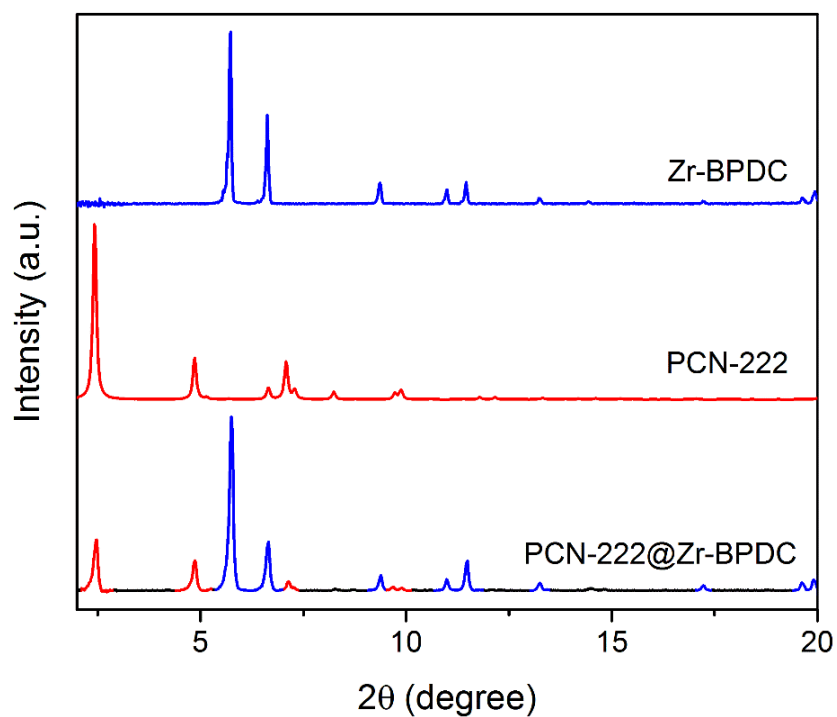


Figure II-4 PXRD patterns of Zr-BPDC, PCN-222 and PCN-222@Zr-BPDC.

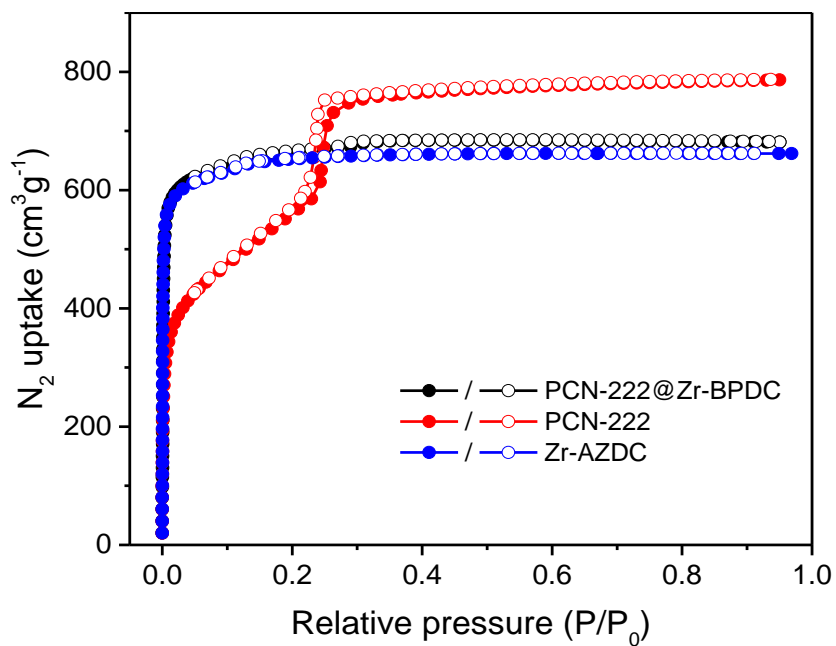


Figure II-5 Gas adsorption isotherms of Zr-BPDC, PCN-222 and PCN-222@Zr-BPDC.

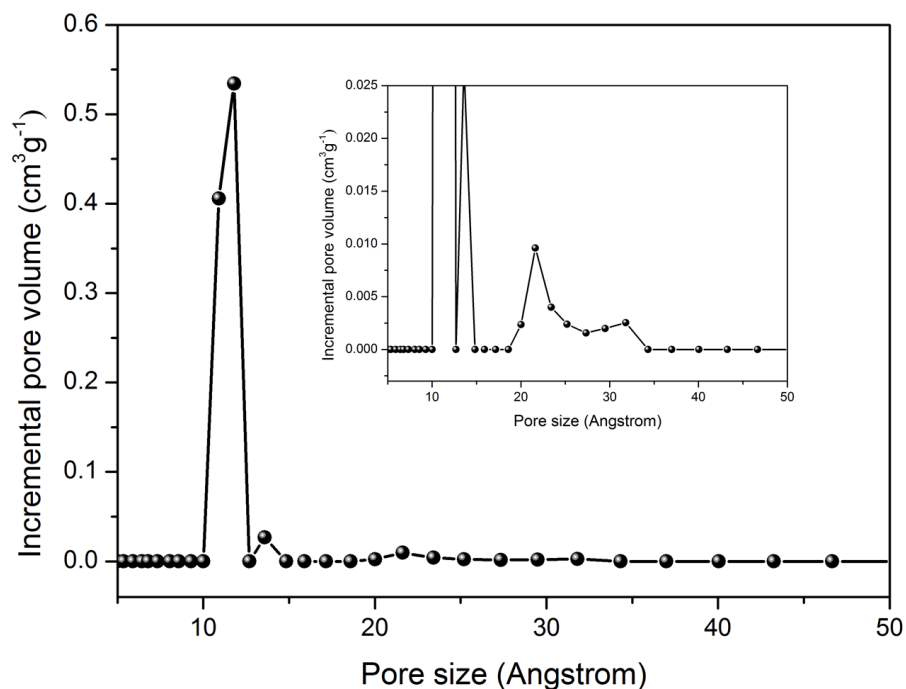


Figure II-6 Pore size distribution of PCN-222@Zr-BPDC. Insert shows the mesopores from PCN-222.

The crystal growth of PCN-222, Zr-BPDC, and PCN-222@Zr-BPDC were monitored and compared to shed light on the formation mechanism of core-shell structures. During the crystal growth of PCN-222@Zr-BPDC(UiO-67), the nucleation of PCN-222 was preferred at the beginning and formed the needlelike crystal, because highly connected TCPP linkers competitively bind with Zr^{4+} . The PCN-222 crystals were formed within two days (Figure II-7, red and blue traces) and subsequently acted as seed crystals to accelerate the growth of the otherwise slow Zr-BPDC(UiO-67) crystallization on its surface. The formation of Zr-BPDC(UiO-67) was observed on the surface of PCN-222 after five days (Figure II-7, blue trace). With the extension of reaction time, the Zr-BPDC(UiO-67) shell kept growing as the concentration of volatile TFA decreased. Indeed,

the heterogeneous nucleation takes place faster than the homogeneous one as PCN-222 crystals act as a template for Zr-BPDC(UiO-67) crystal growth. A control experiment was conducted under synthetic conditions similar to those of the core-shell MOF composite but without the TCPP linkers. This experiment took much longer time (~10 days) to form the Zr-BPDC(UiO-67) crystals as a result of the lack of crystal nucleus (Figure II-7, black trace). This indicates the remarkably accelerating effect of PCN-222 on the nucleation of Zr-BPDC(UiO-67) crystals.

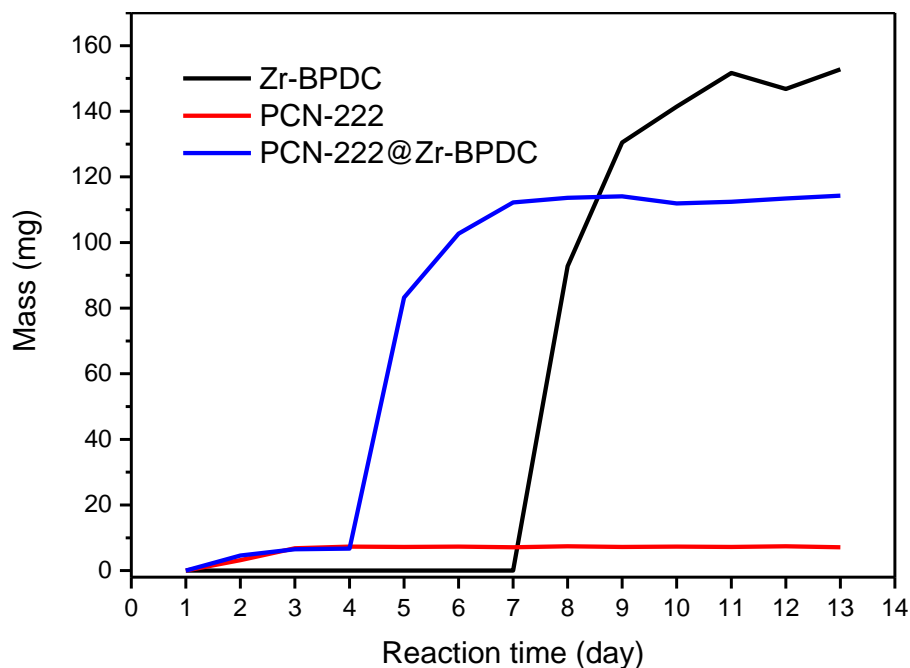


Figure II-7 Time course analysis of formation of PCN-222 (red), PCN-222@Zr-BPDC (blue) and Zr-BPDC (black).

Orthogonal modification of the core-MOF and shell-MOF can be realized in the PCN-222@Zr-BPDC(UiO-67) system to produce multifunctional MOF composites. The porphyrin moiety in PCN-222 can be coordinated with a variety of metals. Different

metalloporphyrin based linkers were successfully incorporated into PCN-222(M)@Zr-BPDC(UiO-67) ($M = \text{Mn}^{2+}, \text{Fe}^{3+}, \text{Ni}^{2+}, \text{and Zn}^{2+}$) (Figure II-8). Furthermore, the Zr-BPDC(UiO-67) shells were modified with different functional groups including bipyridyl, nitro, iodo, and methoxy groups (PCN-222@Zr-BPYDC (BPYDC = 2,2'-bipyridyl-5,5'-dicarboxylate), PCN-222@Zr-BPDC-NO₂ (BPDC-NO₂= 2,2'-Dinitrobiphenyl-4,4'-dicarboxylate, PCN-222@Zr-BPDC-I (BPDC-I= 2,2'-Diiodobiphenyl-4,4'-dicarboxylate) and PCN-222@Zr-BPDC-OMe (BPDC-OMe= 2,2'-Dimethoxybiphenyl-4,4'-dicarboxylate)) (Figure II-9). The PXRD patterns (Figures II-10-13) showed the high crystallinity of these core-shell MOF composites and all N₂ adsorption isotherms (Figures II-14-17) presented noticeable hysteresis loop near $P/P_0 = 0.3$ due to the presence of PCN-222. In addition, we tuned the length of the linear linker by using NDC (NDC = naphthalene dicarboxylate) and AZDC (AZDC = azobenzene dicarboxylate), which are shorter or longer than BPDC, respectively. From the microscopic images (Figures II-18-19) and SEM images (Figures II-20-22), we could easily distinguish the core-shell structure of PCN-222@Zr-NDC and PCN-222@Zr-AZDC. The PXRD patterns (Figures II-23-24) and N₂ adsorption isotherms (Figures II-25-26) demonstrated high crystallinity and accessibility of pores of the core-shell MOF composites, respectively. As the core and shell components can be easily tuned by functionalizing the linear linker and the TCPP ligand, the PCN-222@UiO-series are an ideal platform to take advantage of both MOFs.

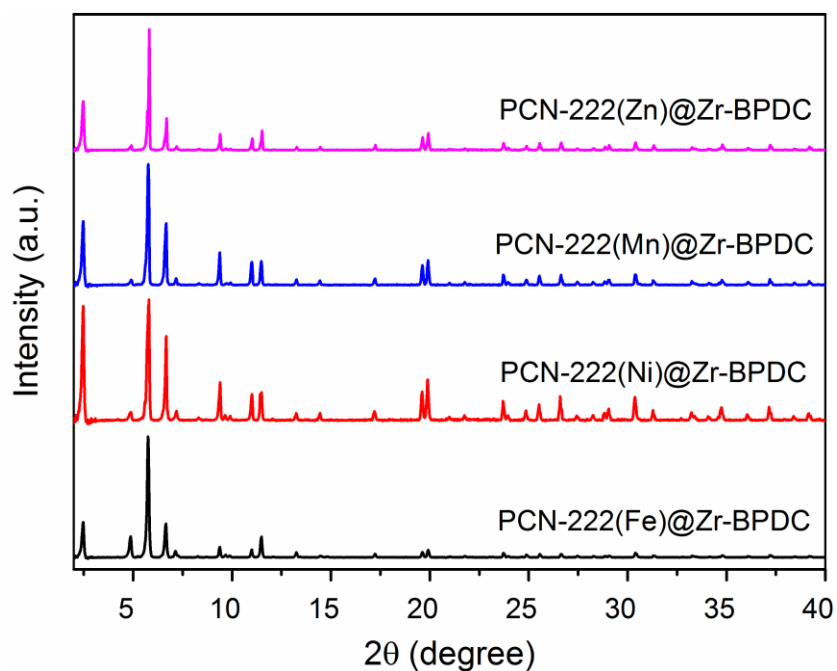


Figure II-8 PXRD of PCN-222(Fe)@Zr-BPDC, PCN-222(Ni)@Zr-BPDC, PCN-222(Mn)@Zr-BPDC, and PCN-222(Zn)@Zr-BPDC.

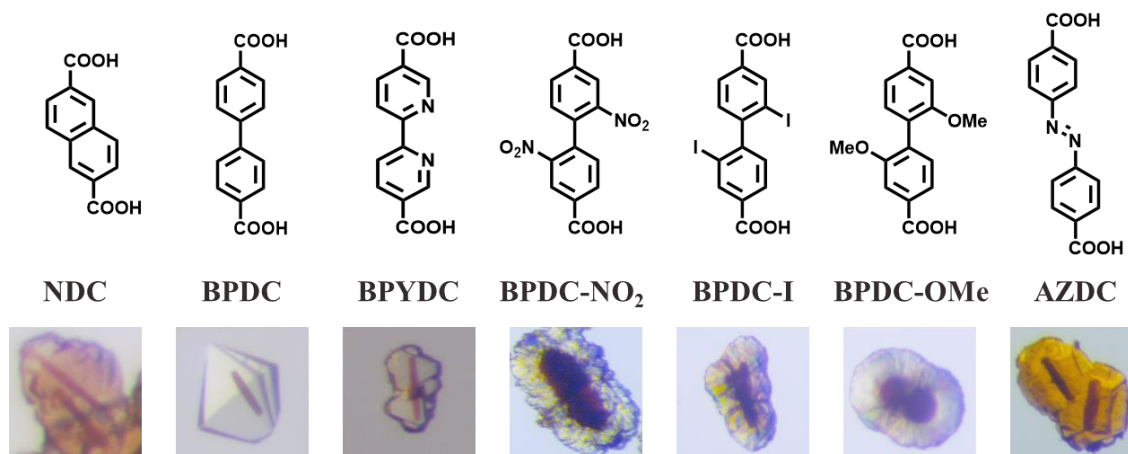


Figure II-9 Microscopic images of PCN-222@Zr-NDC, PCN-222@Zr-BPDC, PCN-222@Zr-BPYDC, PCN-222@Zr-BPDC-NO₂, PCN-222@Zr-BPDC-I, PCN-222@Zr-BPDC-OMe, and PCN-222@Zr-AZDC.

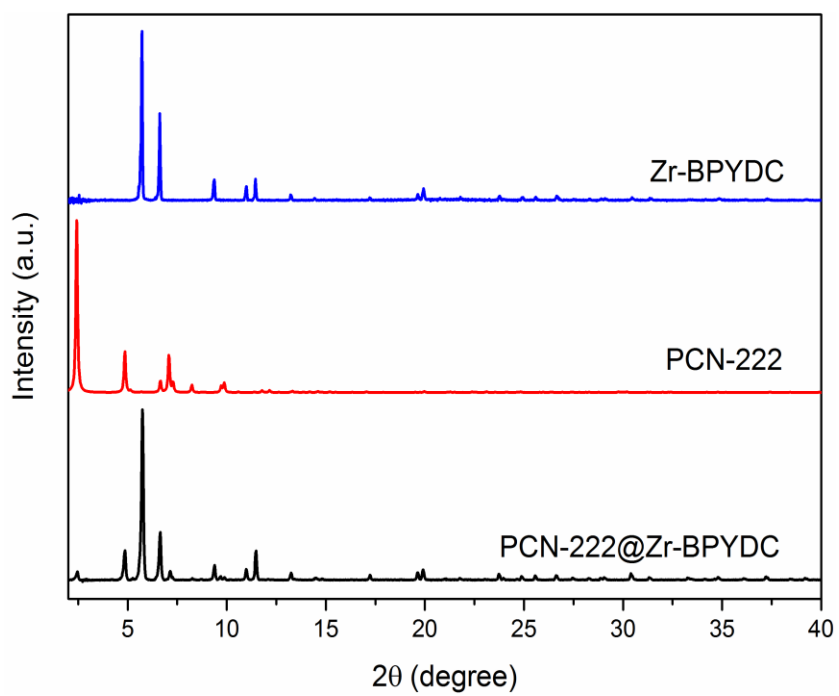


Figure II-10 PXRD patterns of PCN-222@Zr-BPYDC, PCN222, and Zr-BPYDC.

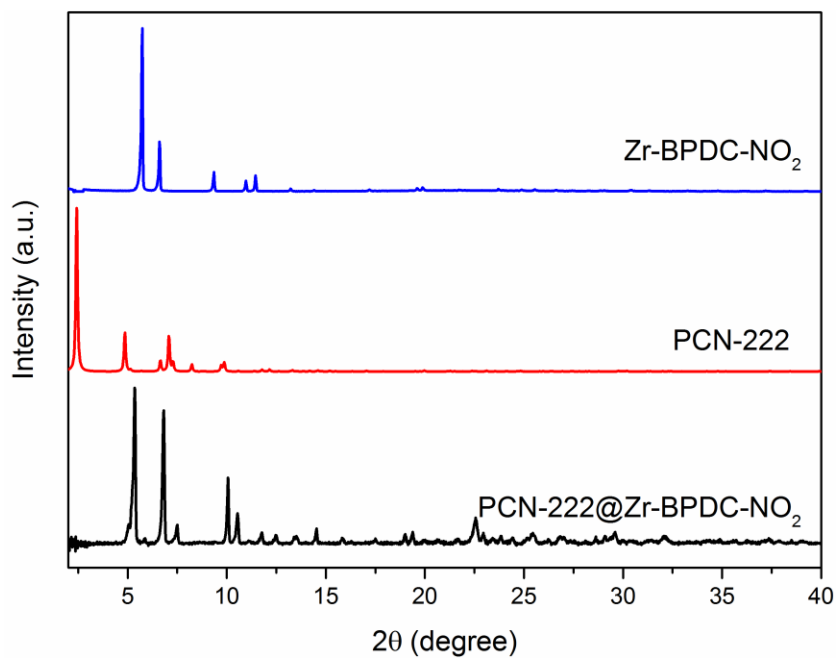


Figure II-11 PXRD patterns of PCN-222@Zr-BPDC-NO₂, PCN-222, and Zr-BPDC-NO₂.

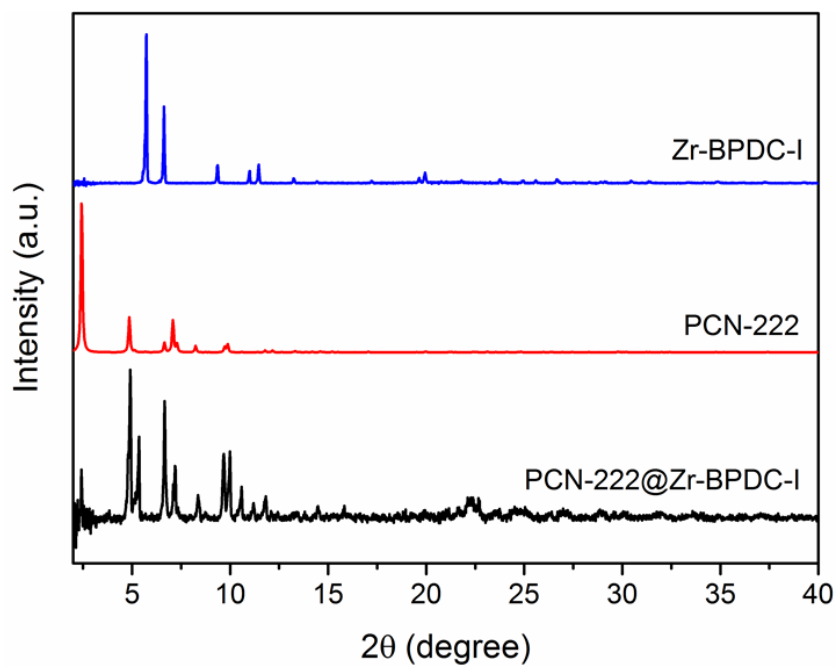


Figure II-12 PXR D patterns of PCN-222@Zr-BPDC-I, PCN-222, and Zr-BPDC-I.

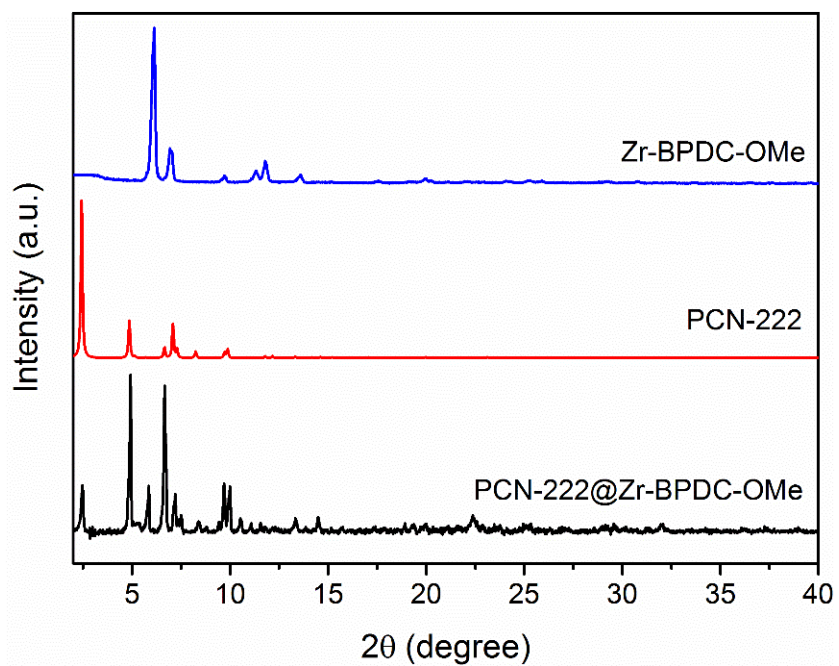


Figure II-13 PXR D of PCN-222@Zr-BPDC-OMe, PCN-222, and Zr-BPDC-OMe.

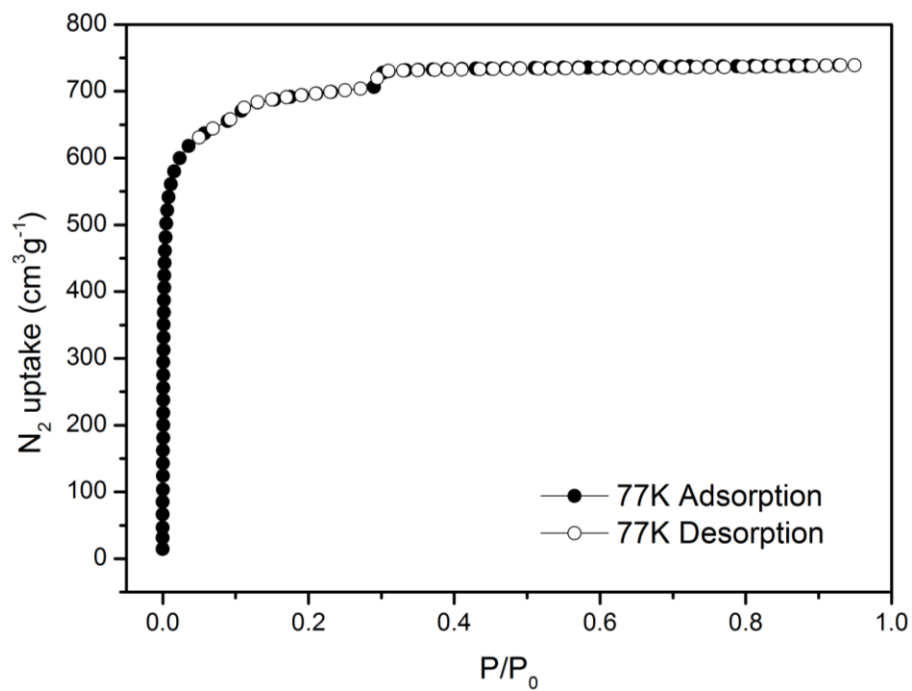


Figure II-14 N₂ Uptake of PCN-222@Zr-BPYDC.

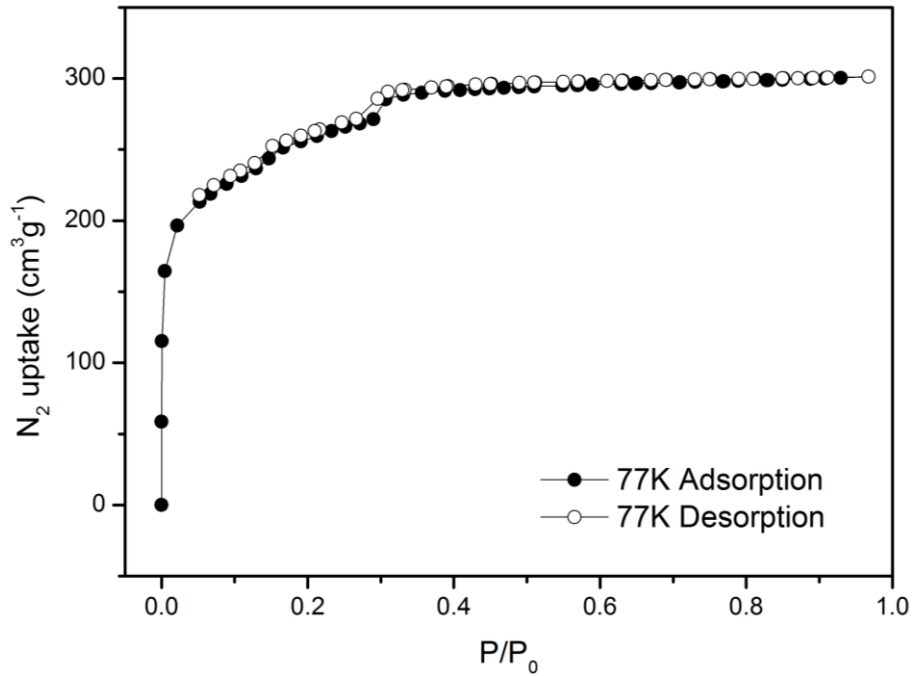


Figure II-15 N₂ Uptake of PCN-222@Zr-BPDC-NO₂.

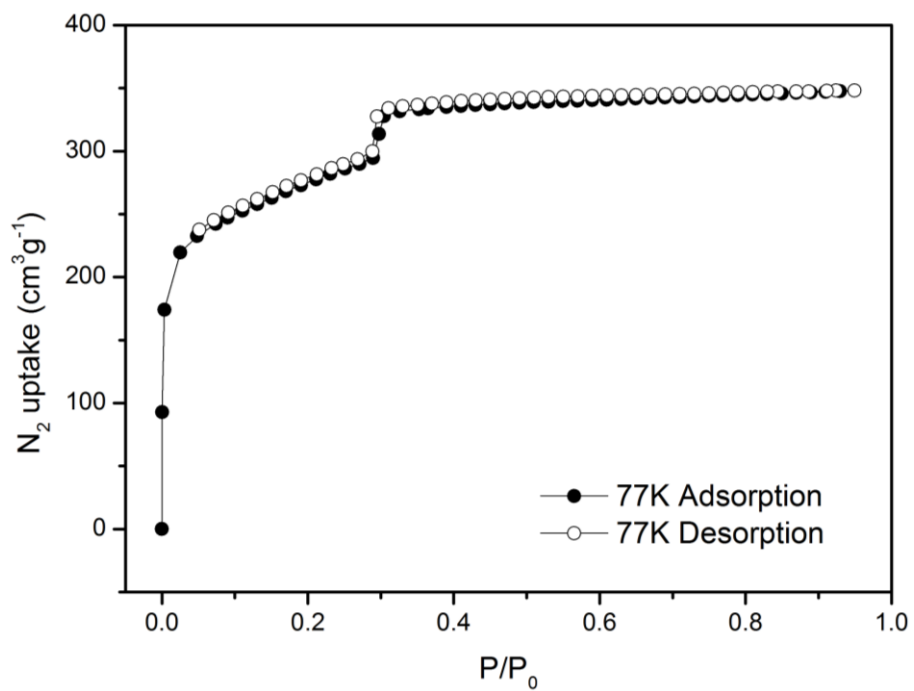


Figure II-16 N₂ Uptake of PCN-222@Zr-BPDC-I.

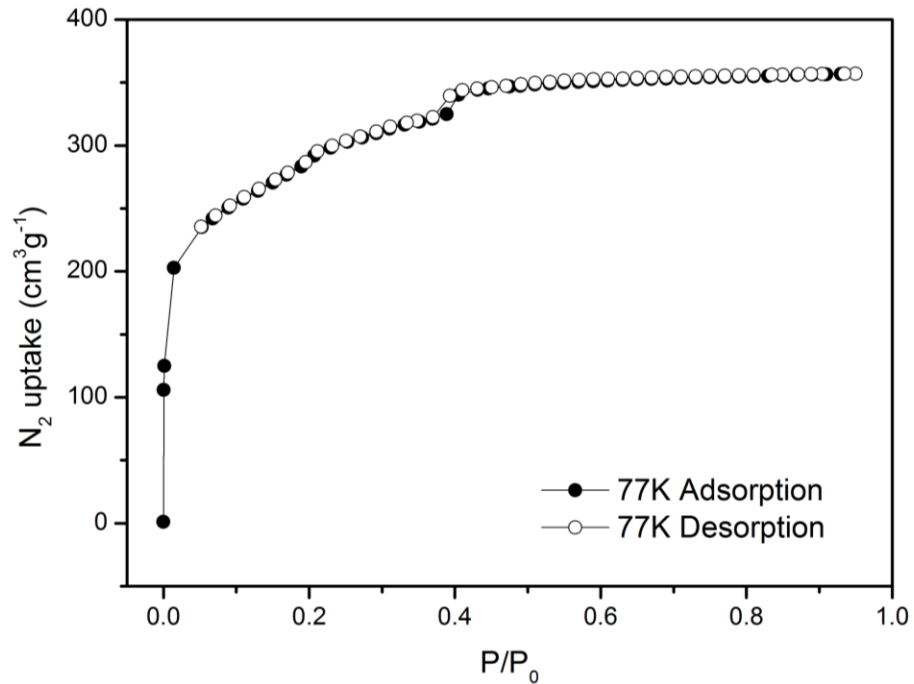


Figure II-17 N₂ Uptake of PCN-222@Zr-BPDC-OMe.

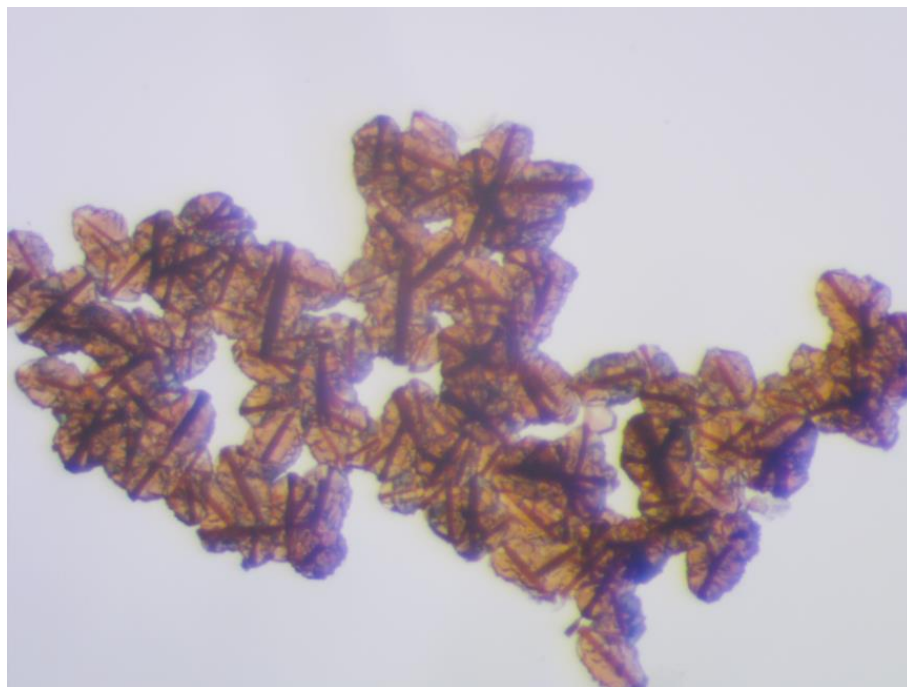


Figure II-18 Microscopic image of PCN-222@Zr-NDC.

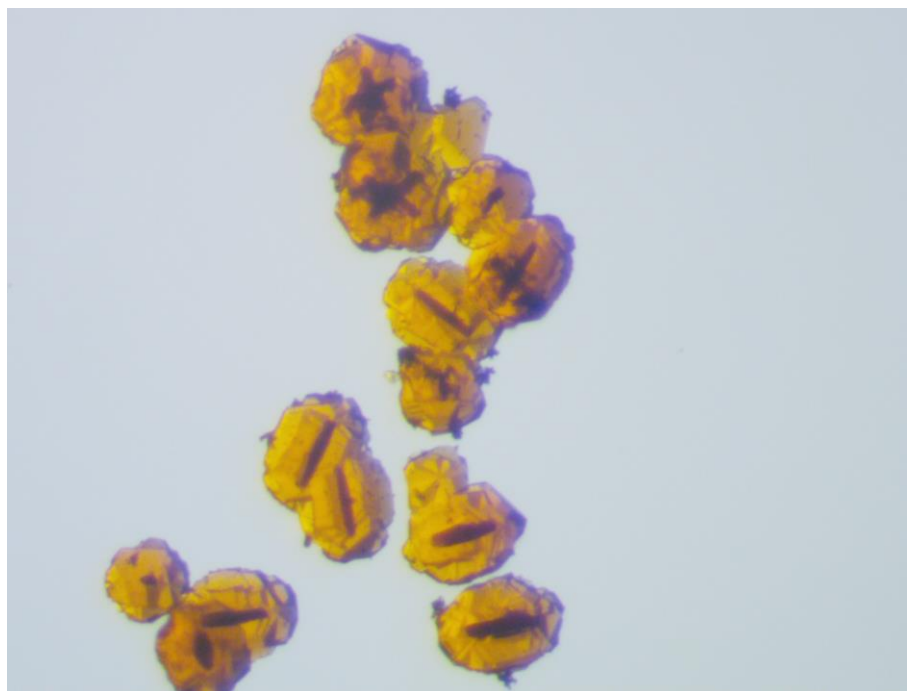


Figure II-19 Microscopic image of PCN-222@Zr-AZDC.

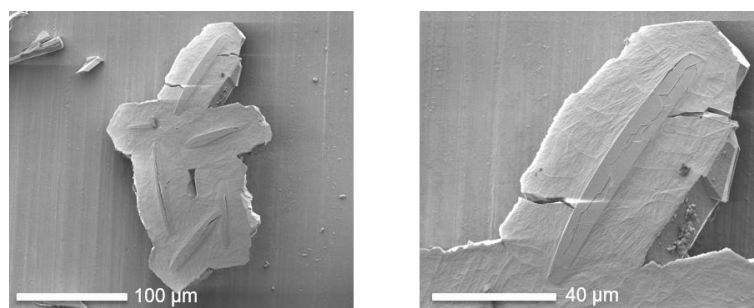


Figure II-20 SEM images of PCN-222@Zr-NDC.

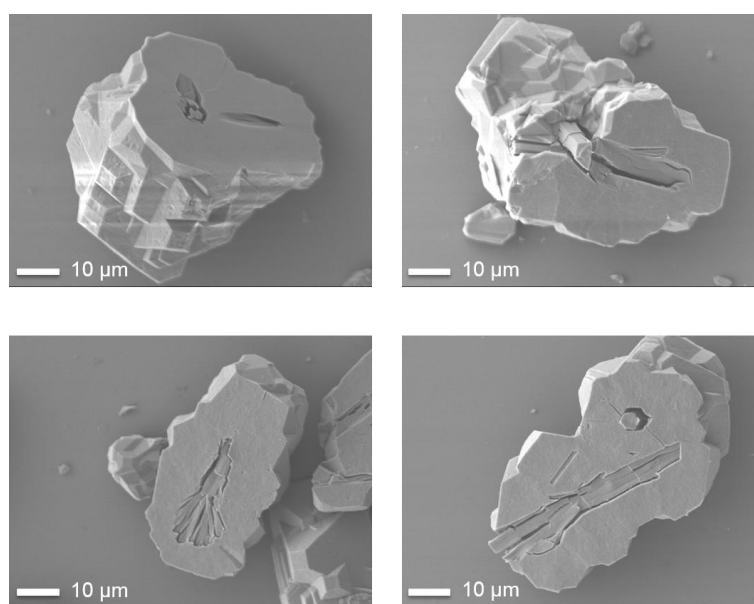


Figure II-21 SEM images of PCN-222@Zr-BPDC.

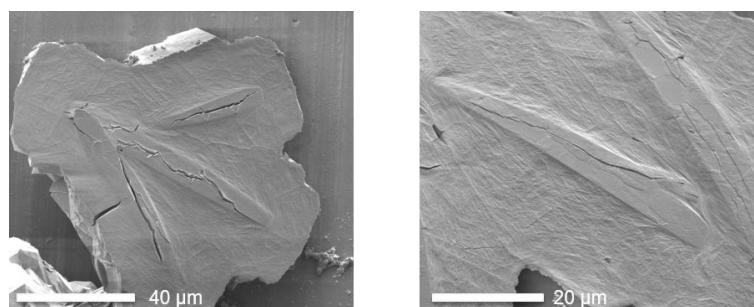


Figure II-22 SEM images of PCN-222@Zr-AZDC.

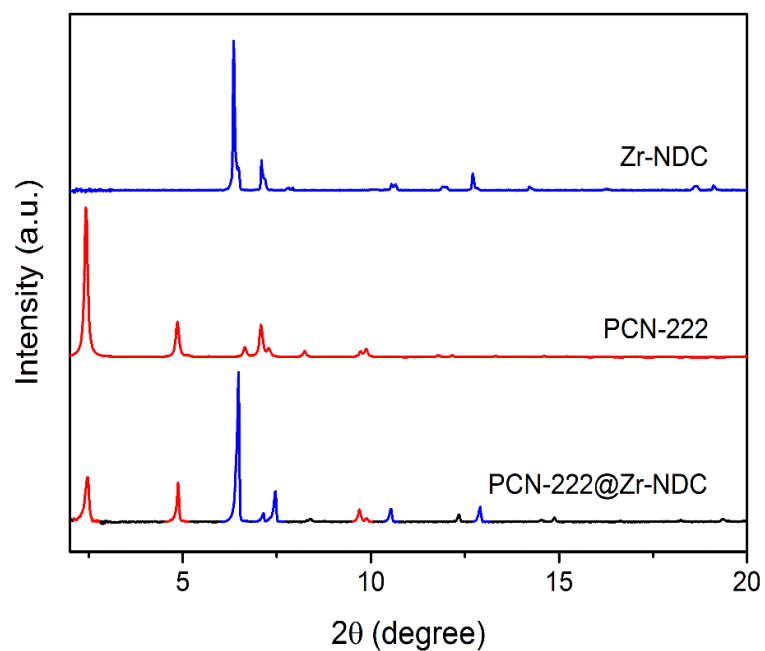


Figure II-23 PXRD patterns of Zr-NDC, PCN-222 and PCN-222@Zr-NDC.

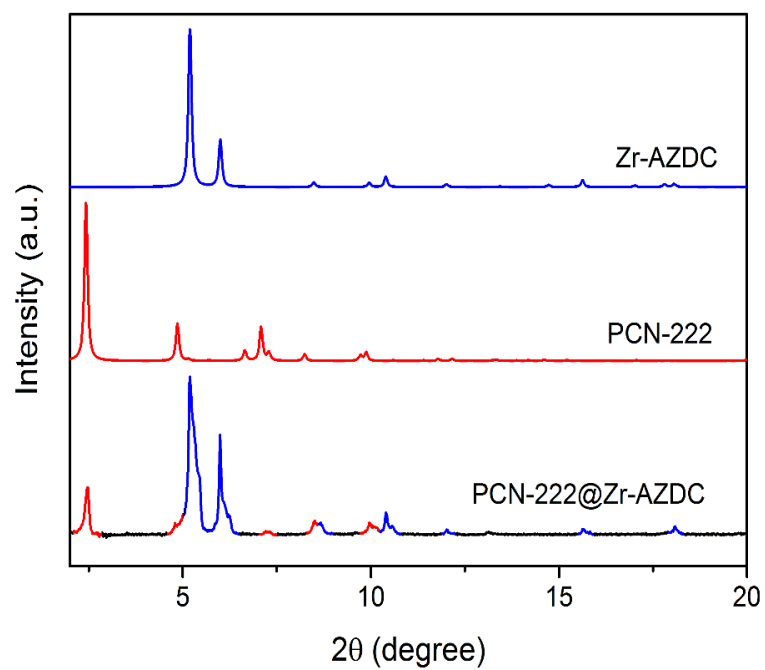


Figure II-24 PXRD patterns of Zr-AZDC, PCN-222 and PCN-222@Zr-AZDC.

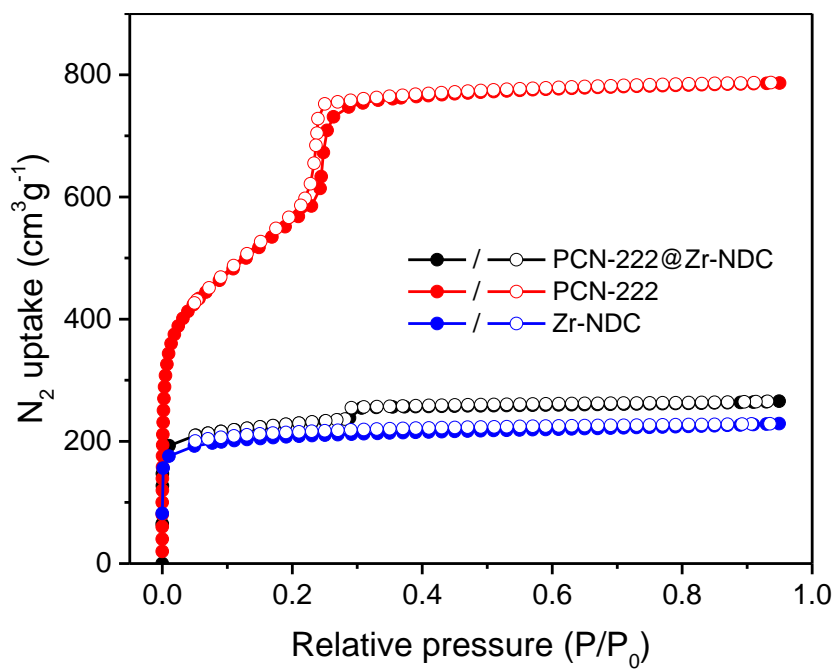


Figure II-25 Gas adsorption isotherms of Zr-NDC, PCN-222 and PCN-222@Zr-NDC.

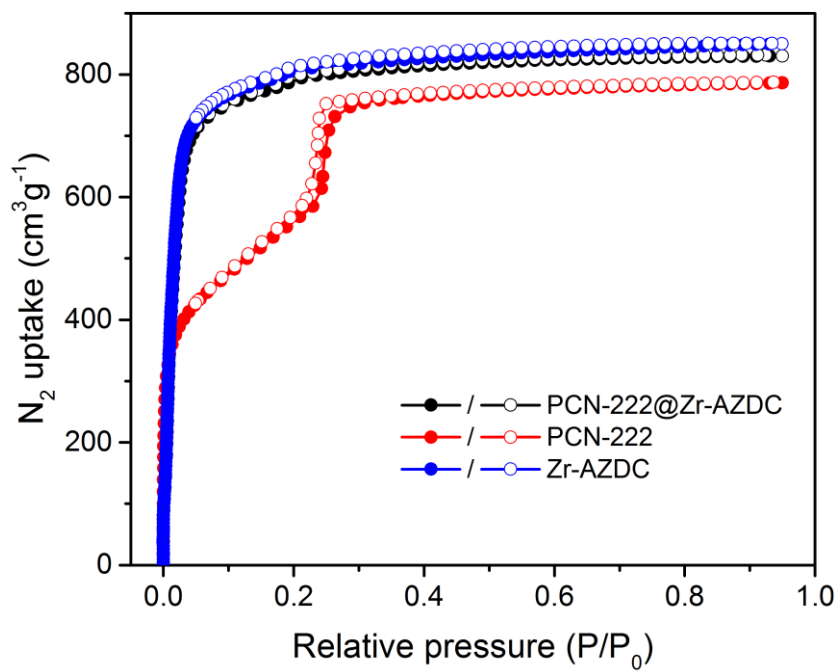


Figure II-26 Gas adsorption isotherms of Zr-AZDC, PCN-222 and PCN-222@Zr-AZDC.

Olefin epoxidation is an important reaction as epoxides are widely used in the production of epoxy resins, paints, and surfactants. Epoxides are also intermediates in many organic reactions. Although many catalytic epoxidation reactions using transition-metal compounds have been successfully demonstrated^[15], the homogeneous catalysts are somewhat under-utilized due to difficulties in product separation from the residual catalyst. Therefore, the immobilization of homogeneous catalysts has attracted a lot of attention. Common polymer or silica supported catalysts, however, give rise to poor selectivity. Herein, core-shell MOFs have been applied as the catalyst, in which the well-defined pores of MOFs can enhance shape and size selectivity.

Firstly, a series of functionalized core-shell MOFs, including PCN-222(Fe)@Zr-NDC, PCN-222(Fe)@Zr-BPDC(UiO-67), and PCN-222(Fe)@Zr-AZDC, have been prepared. The core MOF, with Fe-porphyrin moieties, acted as the catalytic center for olefin epoxidation reaction, while the shell with a tunable window size, controlled the selectivity of the substrates. The two components worked synergistically leading to a size-selective catalyst. The compositions of the core-shell MOFs were investigated by ¹H-NMR digest experiments (Figures II-27-29). The core shell ratios, defined as the molar ratio of the tetratopic linker to the linear linker, were determined to be 0.01, 0.02, and 0.04 for PCN-222@Zr-NDC, PCN-222@Zr-BPDC(UiO-67), and PCN-222@Zr-AZDC, respectively. The catalytic performance of PCN-222(Fe)@Zr-BPDC(UiO-67) in the epoxidation of various olefins with different steric hindrance was evaluated. As shown in Table II-1, the olefins were converted to corresponding epoxides in different conversion ratios due to their molecular sizes. The small olefins (Table II-1, entry 1-5) showed ideal

conversions, suggesting the high accessibility and activity of the catalytic center. Indeed, the sizes of these olefins are smaller than the window sizes of Zr-BPDC(UiO-67), allowing for efficient diffusion of the substrates. Olefin size correlates very well with conversion; as olefin size increases, the conversion decreases. This trend for decreased olefin conversion eventually became little to no conversion under similar experimental conditions, even with longer reaction times. The large olefins (Table II-1, entry 8-10) longer than BPDC were blocked by the shell. The shell, though inert in catalysis, limited the diffusion rates of the substrates and the accessibility of catalytic centers, leading to clear size selectivity.

Table II-1 PCN-222(Fe)@Zr-BPDC catalyzed epoxidation of alkenes. ^a





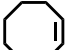
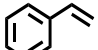
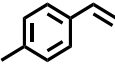


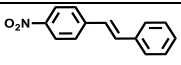
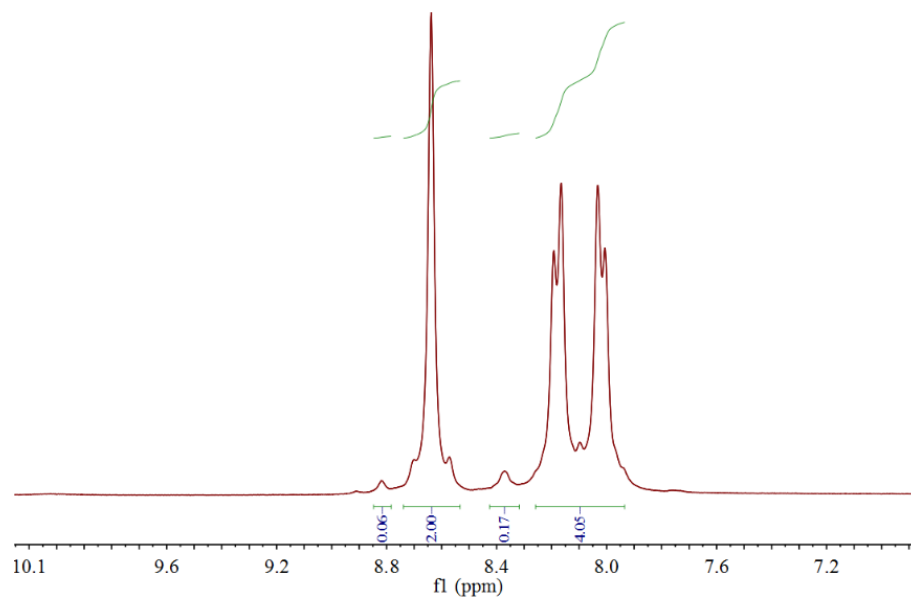
Entry	Substrate	Time(h)	Conversion (%)	
			PCN-222(Fe)@UiO-67	PCN-222(Fe)
1		12	>99	>99
2		12	>99	>99
3		12	97	>99
4		12	95	>99
5		12	91	>99
6		24	87	96

Table II-2 PCN-222(Fe)@Zr-BPDC catalyzed epoxidation of alkenes. (continued)

Entry	Substrate	Time(h)	Conversion (%)	
			PCN-222(Fe)@UiO-67	PCN-222(Fe)
7		24	47	95
8		24	<1	57
9		24	<1	47
10		24	<1	41

^a Reaction conditions: Olefin (500 mM), PhIO (10 mM), catalyst (5 mM, based on PCN-222(Fe)) and acetonitrile (5.0 mL) sealed in a Teflon-lined screw cap vial were stirred at room temperature.

^b Conversion was determined by ¹H NMR with 1,4-dibromobenzene as the internal standard.

**Figure II-27** ¹H NMR of PCN-222@Zr-NDC.

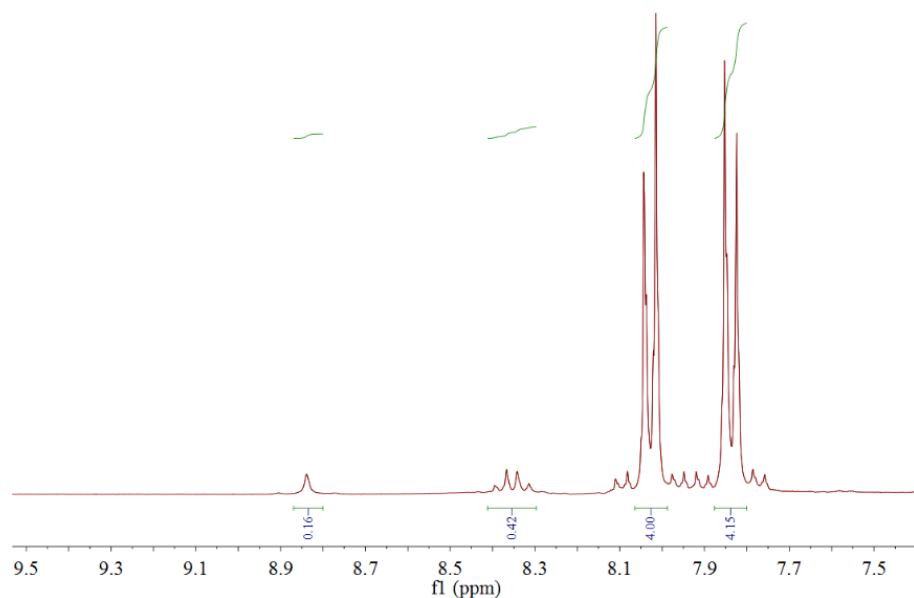


Figure II-28 ^1H NMR of PCN-222@Zr-BPDC.

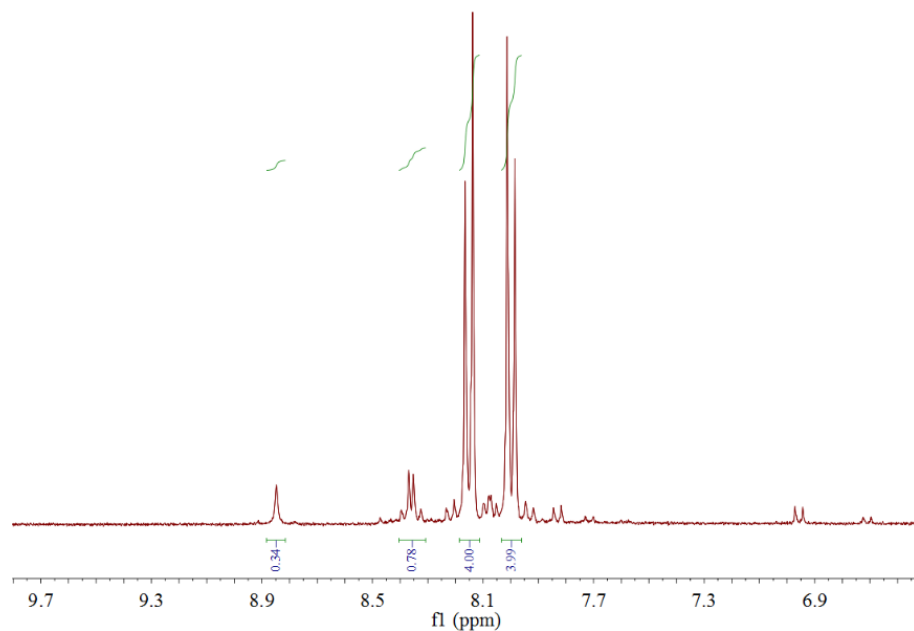


Figure II-29 ^1H NMR of PCN-222@UiO-AZDC.

From Table II-1, it is clear that in size, substrates 6 and 7 are comparable to that of the open window in Zr-BPDC(UiO-67). However, an additional methyl group in

substrate 7, accounts for a 40% decrease in conversion compared to that of substrate 6! To further explore the reason behind this dramatic decrease in conversion, similar epoxidation reactions were carried out by using PCN-222(Fe)@Zr-NDC and PCN-222(Fe)@Zr-AZDC. Consequently, the conversions of substrate 6 and 7 were dramatically altered as a result of their respective steric hindrance due to the change in window size (Figure II-30). With Zr-NDC as the shell, substrate 7 was blocked by the narrow open window, accounting for the lower conversion. With a Zr-AZDC shell, nearly all of the substrates can diffuse through the windows of the shell structure to reach the catalytic center. The PXRD patterns of core-shell MOFs recovered from catalytic reactions remained essentially unchanged from the freshly prepared samples (Figures II-31-33), indicating that these selective catalysts were very stable under reaction conditions.

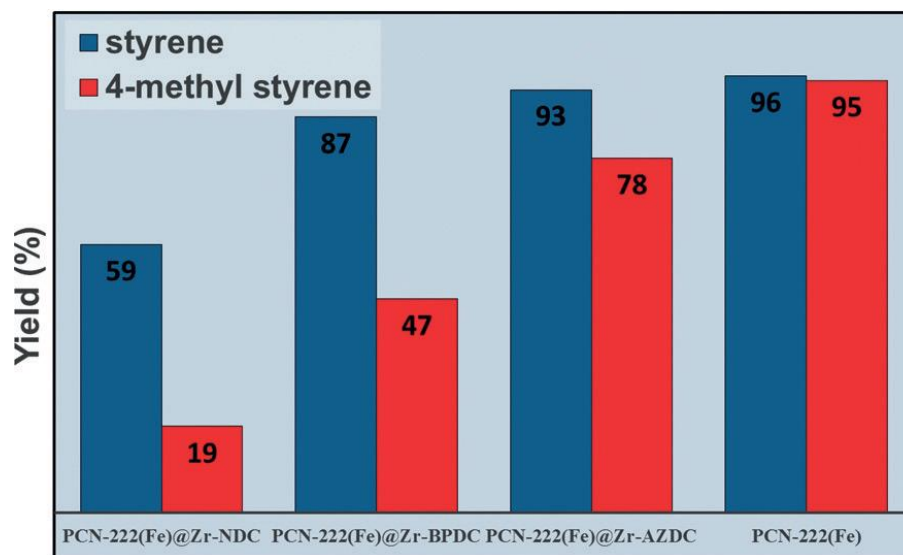


Figure II-30 Size selective olefin epoxidation using PCN-222(Fe)@Zr-NDC, PCN-222(Fe)@Zr-BPDC, PCN-222(Fe)@Zr-AZDC, and PCN-222(Fe).

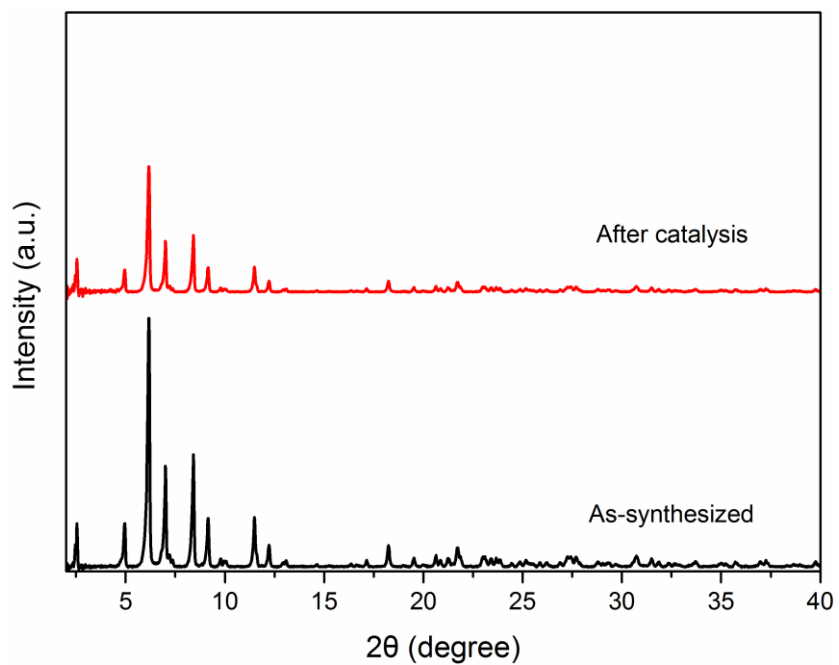


Figure II-31 PXRD of as-synthesized and after catalysis PCN-222(Fe)@Zr-NDC.

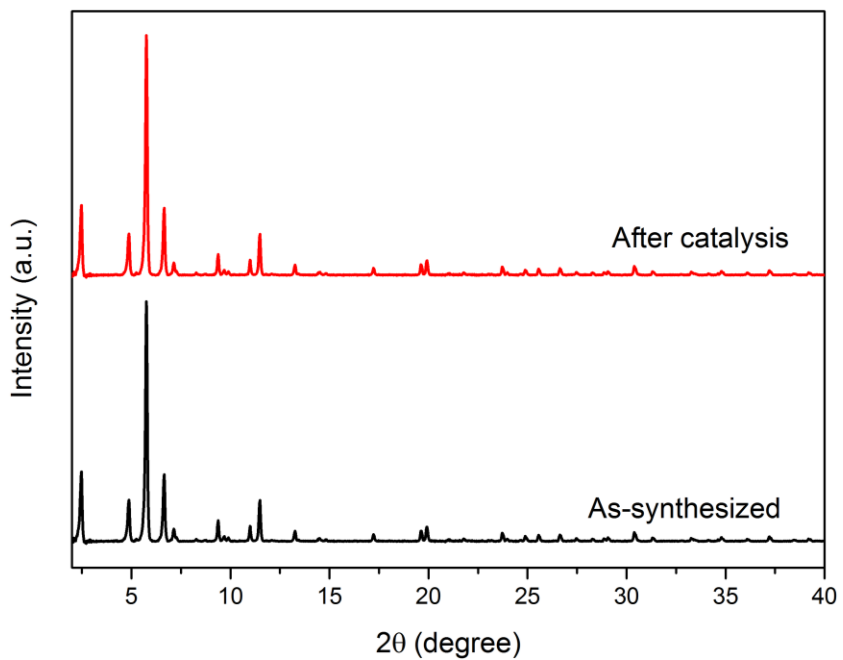


Figure II-32 PXRD of as-synthesized and after catalysis PCN-222(Fe)@Zr-BPDC.

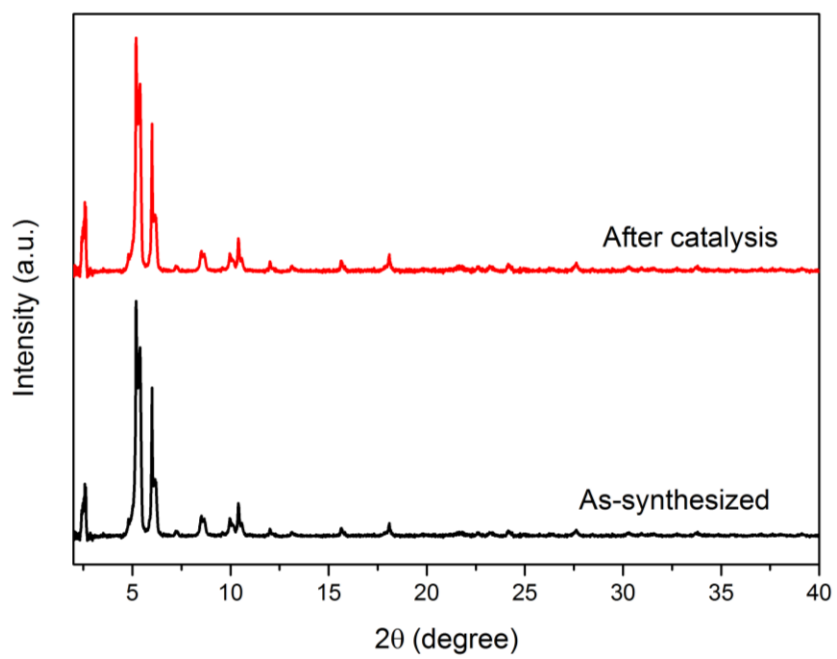


Figure II-33 PXRD of as-synthesized and after catalysis PCN-222(Fe)@Zr-AZDC.

2.4 Conclusion

The core–shell architectures were fully characterized by optical microscopic images, PXRD, N₂ sorption isotherms, and SEM images. Size selective catalysis is realized in the core–shell MOFs by judicious isorecticular expansion of the shells. The strategies developed shall lead to facile synthesis of hybrid core–shell MOF composite with enhanced functionalities.

CHAPTER III

FURTHER DEVELOPMENT OF HYBRID CORE-SHELL MOF

3.1 Introduction

As inorganic and organic hybrid materials, metal–organic frameworks (MOFs) epitomize an ideal tunable platform through judicious design of metal nodes, organic linkers, as well as the combination thereof. Quests for advanced functionalities in MOFs inevitably encounter increasing complexity in their tailored framework architectures. Constructing MOFs from multiple components is a pathway to achieve sophisticated applications which require high complexity in highly ordered crystalline materials. Even though various hybrid MOFs have been made through conventional methods, epitaxial growth of MOF-on-MOF composite is still a challenging research topic.

Core-shell MOFs are a special group of hierarchical MOF composites as the dense MOF shell can enrich the functions of the resultant composite from at least the following three aspects: a) discriminate larger guest molecules through a molecular sieving mechanism for selective catalysis; b) serve as a protective layer to mitigate the inherent instability of the core MOF; and c) serve as a transition layer to bridge the core MOF and its surroundings.

In previously reported methods, the core-shell MOFs were synthesized via a stepwise strategy that involved growing the shell-MOFs on top of the preformed core-MOFs with matched lattice parameters. In 2017, Su and coworkers synthesized a series of core-shell heteroatomic lanthanide MOF hierarchical single crystals through liquid-phase anisotropic epitaxial growth (Figure III-1).¹⁷⁴ Different types of domain and orientation-

controlled multicolor photophysical models are presented, which show either visually distinguishable or visible/near infrared (NIR) emissive colors.

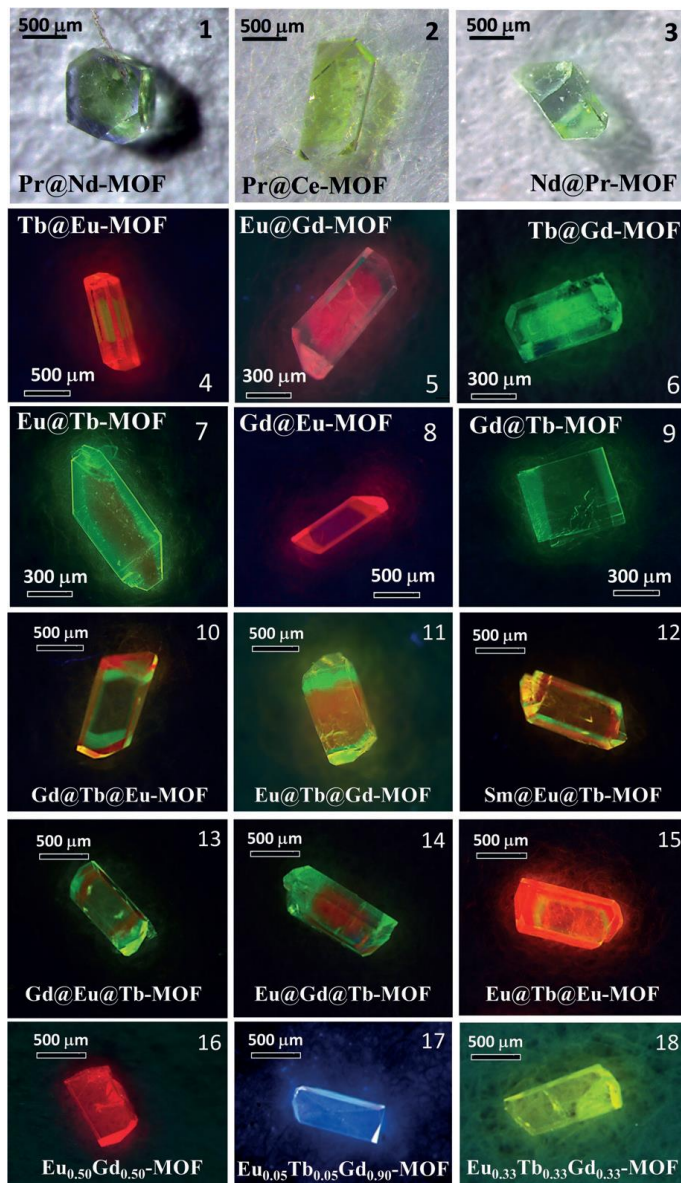


Figure III-1 Photographs of bimetallic and trimetallic hierarchical single crystals showing visually distinguishable colors (1-3, under daylight) or emissive colors (4-15, under UV radiation, $\lambda_{ex}=350$ nm), while solid-solution crystals show uniform emissive colors (16-18, under UV radiation, $\lambda_{ex}=350$ nm). Eu@Tb-MOF means Eu/Tb bimetallic crystal grown from Eu-MOF seed, and so on. Reproduce with permission from Ref. 174 copyright © 2017 John Wiley and Sons.

However, the inconvenient stepwise synthesis and the strict lattice-matching requirement have limited the preparation of core-shell MOFs. In this chapter, one-step synthesis strategy will be further studied to demonstrate that the size selective catalytic behavior can be systematically tuned through changing either ligand length or ligand functionality.

3.2 Experimental Section

3.2.1 Materials and Instruments

3.2.1.1 Materials

N,N-dimethylformamide (DMF), trifluoroacetic acid (TFA), acetone, iron(II) chloride tetrahydrate ($\text{FeCl}_2 \cdot 4\text{H}_2\text{O}$), Ethylene glycol dimethyl ether, 1,4-dibromo-2,5-dimethylbenzene, 4-methoxyl carbonylphenylboronic acid, potassium carbonate, THF, MeOH, KOH, 1,4-diiodo-2,3,5,6-tetramethylbenzene, cesium fluoride, 1-Bromohexane, Mg, 1,2-dibromoethane, 1,4-dichlorobenzene, Bromine, hexane, 9,10-dibromoanthracene, $\text{PdCl}_2(\text{PPh}_3)_2$, tetrakis(triphenylphosphine) palladium, $\text{PdCl}_2(\text{dppf})_2$, (1,3-bis[diphenylphosphino]propane)dichloronickel(II) were from Alfa Aesar. All commercial chemicals were used without further purification unless otherwise mentioned.

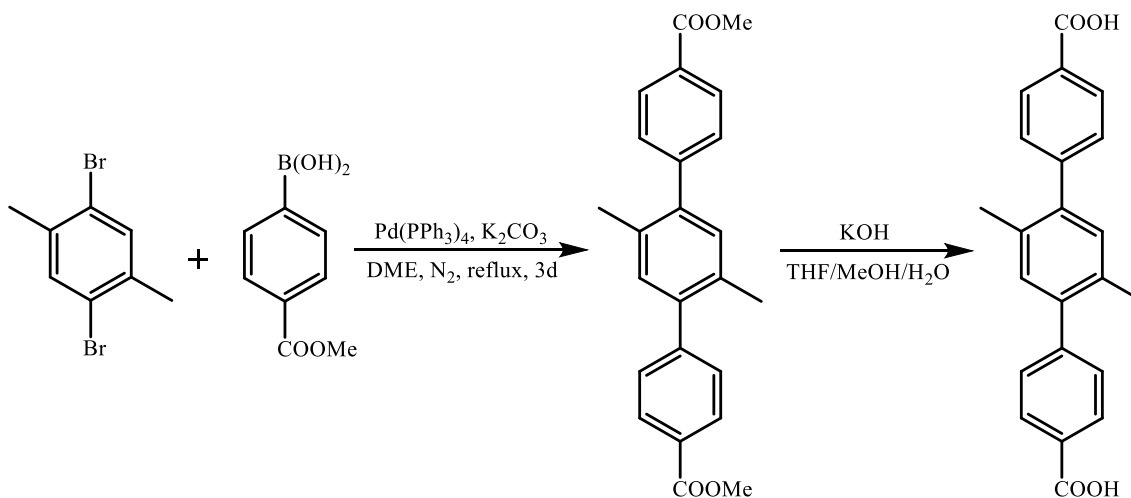
3.2.1.2 Instrumentation

Powder X-ray diffraction (PXRD) measurements were carried out on a BRUKER D8-Focus Bragg-Brentano X-ray Powder Diffractometer equipped with a Cu sealed tube ($\lambda = 1.54178 \text{ \AA}$) at 40 kV and 40 mA. Nuclear magnetic resonance (NMR) data were collected on a Mercury 300 spectrometer. Gas sorption measurements were conducted on a Micromeritics ASAP 2020 system. Fourier transform infrared (FT-IR) measurements were performed on a SHIMADU IR Affinity-1 spectrometer. Scanning electron microscope (SEM) was performed on QUANTA 450 FEG.

3.2.2 Ligand Synthesis

3.2.2.1 Synthesis of 2',5'-dimethyl-[1,1':4',1''-terphenyl]-4,4''-dicarboxylic acid

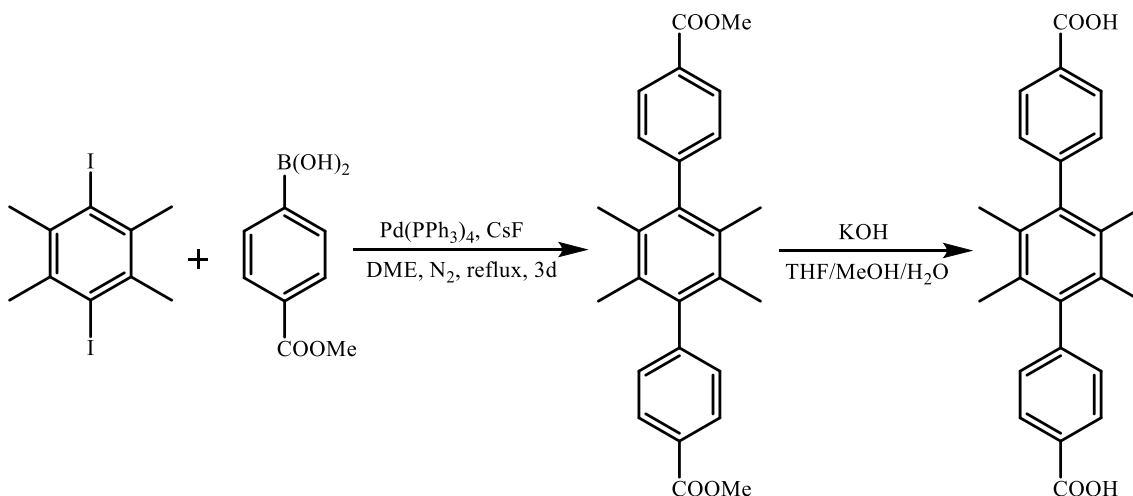
(TPDC-2CH₃)



The 1st step: Ethylene glycol dimethyl ether (DME, 250 mL) was bubbling with nitrogen for around 1 h before introducing into nitrogen-protected solid mixture of 1,4-dibromo-2,5-dimethylbenzene (4 g, 15.2 mmol), 4-methoxycarbonylphenylboronic acid (6.57 g, 36.48 mmol), potassium carbonate (12.59 g, 91.2 mmol) and tetrakis(triphenylphosphine) palladium (0.5 g, 0.43 mmol). The mixture was allowed to reflux for 3 days under nitrogen protection. After cooling to r.t., the solvent was evaporated to dryness. The residue was washed with a large amount of water followed by acetone. After removing the solvent, the residue was purified with column chromatography (silica gel, CH₂Cl₂) to give the ester as a white solid (yield: 4.7 g). ¹H NMR (300 MHz, CDCl₃): δ = 8.11 (d, 4 H), 7.45 (d, 4 H), 7.16 (s, 2 H), 3.96 (s, 6 H), 2.27 (s, 6 H).

The 2nd step: The carboxylic ester (2.0 g, 5.35 mmol) was stirred in THF (60 mL) and MeOH (60 mL) mixed solvent, to which a solution of KOH (8.98 g, 160.4 mmol) in H₂O (32 mL) was introduced. This mixture was refluxed for 12 h. After cooling down to room temperature, THF and MeOH were evaporated. Additional water was added to the resulting solution and the mixture was heated until the solid was fully dissolved, then the homogeneous solution was acidified with diluted HCl until no further precipitate was detected (pH \approx 2-3). The grayish white solid TPDC-2CH₃ was collected by filtration, washing with water and drying in vacuum (1.65 g). ¹H NMR (300 MHz, DMSO): δ = 8.03 (d, 4 H), 7.52 (d, 4 H), 7.20 (s, 2 H), 2.24 (s, 6 H).

3.2.2.2 Synthesis of 2',3',5',6'-tetramethyl-[1,1':4',1''-terphenyl]-4,4''-dicarboxylic acid (TPDC-4CH₃)

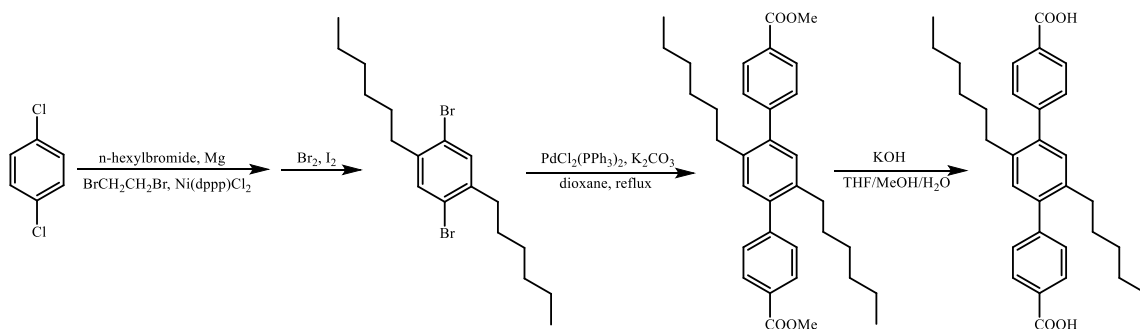


The 1st step: Ethylene glycol dimethyl ether (DME, 100 mL) was bubbling with nitrogen for around 1 h before introducing into nitrogen-protected solid mixture of 1,4-diiodo-2,3,5,6- tetramethylbenzene (1.0 g, 2.59 mmol), 4-methoxyl carbonylphenylboronic acid

(1.12 g, 6.24 mmol), cesium fluoride (2.37 g, 15.6 mmol) and tetrakis (triphenylphosphine) palladium (0.3 g, 0.26 mmol). The mixture was allowed to reflux for 3 days under nitrogen protection. After cooling to r.t., the solvent was evaporated to dryness. The residue was washed with a large amount of water followed by acetone. After removing the solvent, the residue was purified with column chromatography (silica gel, CH₂Cl₂) to give the ester as a white solid (yield: 0.85 g). ¹H NMR (300 MHz, CDCl₃): δ = 8.10 (d, 4 H), 7.26 (d, 4 H), 3.94 (s, 6 H), 1.90 (s, 12 H).

The 2nd step: The carboxylic ester (0.63 g, 1.57 mmol) was stirred in THF (25 mL) and MeOH (25 mL) mixed solvent, to which a solution of KOH (2.63 g, 46.95 mmol) in H₂O (25 mL) was introduced and the mixture was refluxed for 12 h. After cooling down to room temperature, THF and MeOH were evaporated. Additional water was added to the resulting water phase and the mixture was heated until the solid was fully dissolved, then the homogeneous solution was acidified with diluted HCl until no further precipitate was detected (pH ≈ 2-3). The white solid TPDC-4CH₃ was collected by filtration, washing with water and drying in vacuum (0.50 g). ¹H NMR (300 MHz, DMSO-d₆): δ= 8.02 (d, 4 H), 7.26 (d, 4 H), 1.80 (s, 12 H).

3.2.2.3 2',5'-dihexyl-[1,1':4',1''-terphenyl]-4,4''- dicarboxylic acid (TPDC-2Hex)



The 1st step: 1-Bromohexane (30 ml, 213.73 mmol), Mg (5.196 g, 213.73 mmol) and THF (300 ml) were used to make the organomagnesium compound under strictly anhydrous conditions and under nitrogen atmosphere. The Grignard reagent was prepared first, initiated with 1,2-dibromoethane (3 drops). Initially the mixture was cooled to 0°C in an ice-bath, then allowed to reflux for 0.25 h, and finally by heating at reflux for 1 h. After this time all of the magnesium metal had dissolved and the mixture was homogeneous. The mixture was stirred overnight at room temperature then cooled to 0°C. 1,4-Dichlorobenzene (12.567 g, 85.492 mmol) was added slowly in small solid portions followed by (1,3- bis[diphenylphosphino]propane)dichloronickel(II) (0.232 g, 0.427 mmol). The mixture became pale milky green in color. This mixture was heated at reflux for 32 h then cooled to room temperature. Water (40 ml) was added slowly, followed by 2M HCl (aq) (200 ml) and Et₂O (100 ml). The layers were separated and the aqueous layer extracted with Et₂O (5 × 30 ml). The combined organic extracts were dried over anhydrous Na₂SO₄, filtered and concentrated to dryness in vacuo to afford a dark yellow oil. This was purified by flash chromatography using 1:1 Et₂O/Hexane as eluent to afford 1,4- di(hexyl)benzene as a pale yellow coloured oil (20.40g, 97%). Bromine (27.12

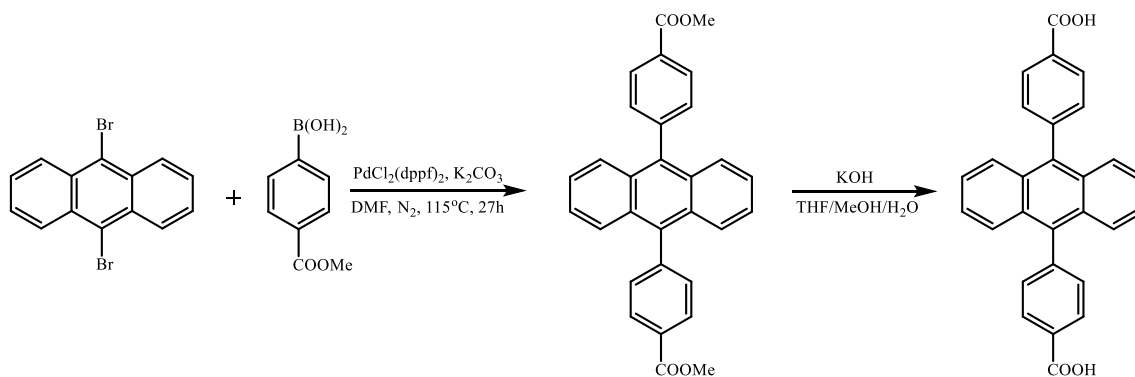
g, 8.7 ml, 169.71 mmol) was added dropwise over 0.5 h to a stirred and ice-cooled mixture of 1,4-di(hexyl)benzene (20.40 g, 82.785 mmol) and iodine (0.214 g, 0.828 mmol) under rigorous exclusion of light. The subsequent mixture was allowed to slowly warm to room temperature and stirred for 24 h. After this time KOH (aq) (20% w/v, 100 ml) was added slowly and the mixture stirred vigorously at 40°C for 1.5 h, then overnight at room temperature during which time the colour of the mixture disappeared. The liquid was then decanted, before more water (100 ml) was added and again decanted to afford an off-white solid. This solid was recrystallized from EtOH to afford 1,4-dibromo-2,5-dihexylbenzene as a colorless crystalline solid (21.689 g, 65%) ¹H NMR (CDCl₃, 300 MHz) δ= 7.35 (s, 2H), 2.64 (dd, 4H), 1.58 (m, 4H), 1.34 (m, 12H), 0.90 (t, 6H).

The 2nd step: 1,4-dibromo-2,5-dihexyl-benzene (2.707 g, 6.696 mmol), 4-(methoxycarbonyl)benzene boronic acid (3.000 g, 16.739 mmol), K₂CO₃ (3.686 g, 26.671 mmol) and PdCl₂(PPh₃)₂ (0.200 g) in anhydrous THF (75 ml) were combined at room temperature under inert atmosphere (N₂), and the resultant suspension heated at reflux with stirring for 20 h. The mixture was then cooled to room temperature, and concentrated to dryness in vacuo. The residue was taken up in H₂O (200 ml) and CH₂Cl₂ (100 ml), and the layers separated. The aqueous phase was extracted with CH₂Cl₂ (3×40 ml), then the combined organic extracts were dried over anhydrous MgSO₄, filtered and concentrated to dryness in vacuo. The mixture was purified by flash chromatography using 1:9 Et₂O/Hexane to afford dimethyl 2',5'-dihexyl-[1,1':4',1''-terphenyl]-4,4''-dicarboxylate

(0.871 g) as a colorless solid. $^1\text{H NMR}$ (CDCl_3 , 300 MHz) δ = 8.10 (d, 4H), 7.43 (d, 4H), 7.12 (s, 2H), 3.96 (s, 6H), 2.55 (dd, 4H), 1.44 (m, 4H), 1.17 (m, 12H), 0.80 (t, 6H).

The 3rd step: Dimethyl 2',5'-dihexyl- [1,1':4',1''-terphenyl]-4,4''-dicarboxylate (500 mg, 0.972 mmol), KOH (435 mg, 7.772 mmol), H_2O (10 ml) and THF (10 ml) were treated by the general procedure to afford the desired 2',5'-dihexyl-[1,1':4',1''-terphenyl]- 4,4''-dicarboxylic acid as a colorless powder (467 mg, 99%). $^1\text{H NMR}$ (DMSO-d_6 , 500 MHz) δ = 0.70 (6H, m), 1.06 (12H, m), 1.33 (4H, m), 2.46 (4H, m), 7.09 (2H, s), 7.44 (4H, d), 7.98 (4H, d), 12.96 (2H, s).

3.2.2.4 4,4'-(anthracene-9,10-diyl)dibenzoic acid (DCDPA) (TPDC-2Ph)



The 1st step: The mixture of 9,10-dibromoanthracene (2.00 g, 5.95 mmol), (4-(methoxycarbonyl)phenyl)boronic acid, (2.68 g, 14.88 mmol) and a catalytic amount of $\text{PdCl}_2(\text{dppf})_2$ (10 mol%) was dissolved in 75 mL of degassed DMF. Then an aqueous 2 M K_2CO_3 solution was added to the mixture and the reaction was heated to 115°C for 27 h until the anthracene-based starting material was consumed. After cooling to room temperature, the crude product was purified by column chromatography (silica, DCM) to

afford compound DCDPA-ester as a pale ivory solid (1.97 g, 74%). ^1H NMR (300 MHz, CDCl_3): δ (ppm) = 8.30 (d, 4H), 7.59 (m, 8H), 7.34 (m, 4H), 4.02 (s, 6H).

The 2nd step: In a 250 mL flask, DCDPA-ester (1.97 g, 4.41 mmol) was suspended in 80 mL THF/MeOH (v:v = 1:1), and 40 mL of 2 M KOH solution was added. The mixture was refluxed for 24 h. The pH value was adjusted to $\sim\text{pH}=2$ using 2 M HCl. The resulting white precipitate was collected by centrifugation, washed with water, and dried under vacuum to afford DCDPA as an ivory solid (1.52 g, 82%). ^1H NMR (300 MHz, DMSO-d_6): δ (ppm) = 13.17 (s, 2H), 8.22 (d, 4H), 7.61 (d, 4H), 7.50 (m, 8H).

3.2.3 MOF Synthesis

3.2.3.1 Synthesis of PCN-222/PCN-222(Fe)@Zr-TPDC-2Me

ZrCl₄ (130 mg), TPDC-2Me (100 mg), TCPP/TCPP(Fe) (10 mg), trifluoroacetic acid (2.5 ml) and DMF (15 ml) were charged in a Pyrex vial. The mixture was heated in 120°C oven for 7 days. After cooling down to room temperature, the crystals of PCN-222/PCN-222(Fe)@Zr-TPDC-2Me were harvested.

3.2.3.2 Synthesis of PCN-222/PCN-222(Fe)@Zr-TPDC-4Me

ZrCl₄ (130 mg), TPDC-4Me (100 mg), TCPP/TCPP(Fe) (10 mg), trifluoroacetic acid (2.5 ml) and DMF (15 ml) were charged in a Pyrex vial. The mixture was heated in 120°C oven for 7 days. After cooling down to room temperature, the crystals of PCN-222/PCN-222(Fe)@Zr-TPDC-4Me were harvested.

3.2.3.3 Synthesis of PCN-222/PCN-222(Fe)@Zr-TPDC-2Hex

ZrCl₄ (130 mg), TPDC-2Hex (100 mg), TCPP/TCPP(Fe) (10 mg), trifluoroacetic acid (2.5 ml) and DMF (15 ml) were charged in a Pyrex vial. The mixture was heated in 120°C oven for 7 days. After cooling down to room temperature, the crystals of PCN-222/PCN-222(Fe)@Zr-TPDC-2Hexyl were harvested.

3.2.3.4 Synthesis of PCN-222/PCN-222(Fe)@Zr-TPDC-2Ph

ZrCl₄ (130 mg), TPDC-2Ph (100 mg), TCPP/TCPP(Fe) (10 mg), trifluoroacetic acid (2.5 ml) and DMF (15 ml) were charged in a Pyrex vial. The mixture was heated in

120°C oven for 7 days. After cooling down to room temperature, the crystals of PCN-222/PCN-222(Fe)@Zr-TPDC-2Ph were harvested.

3.2.3.5 Synthesis of PCN-134/PCN-134(Fe)@Zr-BTB

ZrCl₄ (150 mg), BTB (108 mg), TCPP/TCPP(Fe) (24 mg), trifluoroacetic acid (1.5 ml) and DMF (15 ml) were charged in a Pyrex vial. The mixture was heated in 120°C oven for 5 days. After cooling down to room temperature, the crystals of PCN-134/PCN-134(Fe)@Zr-BTB were harvested.

3.2.3.6 Synthesis of PCN-222@Nu-1000

ZrCl₄ (100 mg), TCPP (40 mg), TBAPy (40 mg), trifluoroacetic acid (2.5 ml), and DMF (15 ml) were charged in a Pyrex vial. The mixture was heated in 120°C oven for 7 days. After cooling down to room temperature, the crystals of PCN-222@Nu-1000 were harvested.

3.2.3.7 Synthesis of La-TCPP@La-BPDC

LaCl₃ (100 mg), TCPP (20 mg), BPDC (50 mg), trifluoroacetic acid (1 ml), and DMF (15 ml) were charged in a Pyrex vial. The mixture was heated in 120 oven for 3 days. After cooling down to room temperature, the crystals of La-TCPP@La-BPDC were harvested.

3.3 Results and Discussion

It has been proposed that the stability of MOFs is governed by many factors, among which the metal-ligand bond strength is believed to be crucial for determining the hydrothermal stability of MOF, and it is determined by the nature of both the metal ion and the ligand. Thus, comparing the bonding strength of MOFs with different metals and ligands is not a straightforward affair. Nevertheless, it is well established that metal–ligand bond interactions in MOFs with a given ligand are greatly affected by the oxidation state and the ionic radius, or the charge density of the metal ions. One key feature of Zr-MOFs is the high oxidation state of Zr(IV) compared with M(I), M(II), and M(III)-based MOFs (M= metal elements). Due to high charge density and bond polarization, there is a strong affinity between Zr(IV) and carboxylate O atoms in most carboxylate-based Zr-MOFs. This is in line with Pearson’s hard/soft acid/base concept. Zr(IV) ions and carboxylate ligands are considered hard acid and hard base, respectively, and their coordination bonds are strong. As a result, most Zr-MOFs are stable in organic solvents and water, and even tolerable to acidic aqueous solution. So we chose two kinds of Zr-MOFs, UiO-series and PCN-series, to synthesize hybrid core-shell MOFs through one pot reaction.

Herein, we designed and synthesized a series of core-shell MOFs (PCN-222@Zr-TPDC-2Me, PCN-222@Zr-TPDC-4Me, PCN-222@Zr-TPDC-2Hex, and PCN-222@Zr-TPDC-2Ph), guided by the nucleation kinetics. From the optical microscopic images (Figures III-2-5), one can clearly distinguish the core and shell MOFs: the cores, consist of porphyrin ligands (TCPP), showed red color and needle-like shape and shells are colorless octahedral crystals that result from the using of longer linker linkers.

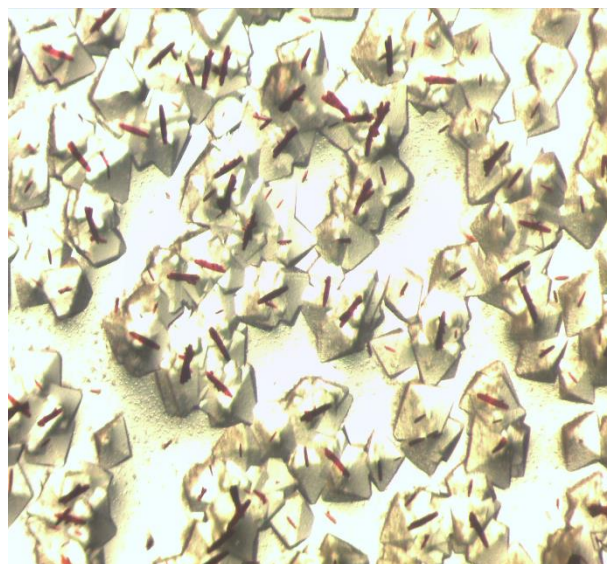


Figure III-2 PCN-222@Zr-TPDC-2Me

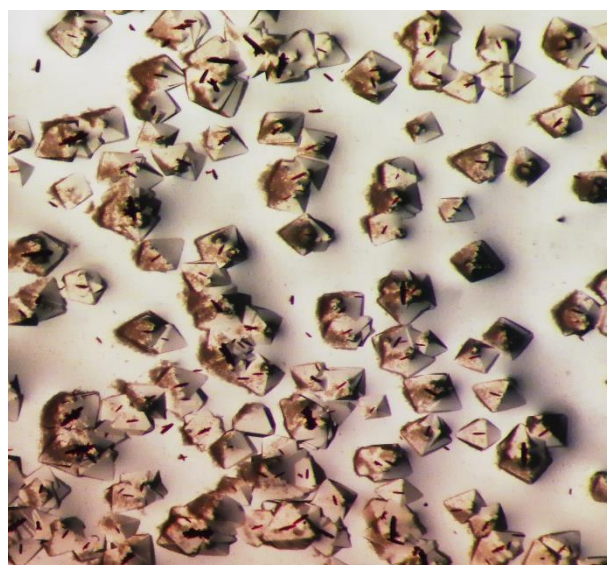


Figure III-3 PCN-222@Zr-TPDC-4Me

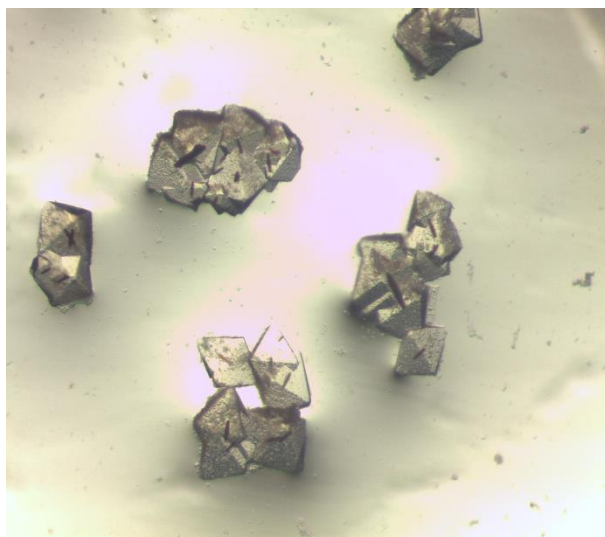


Figure III-4 PCN-222@Zr-TPDC-2Ph

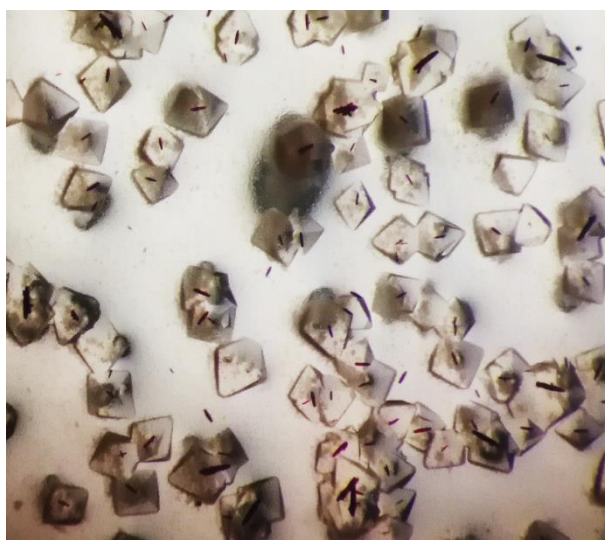


Figure III-5 PCN-222@Zr-TPDC-2Hex

To further demonstrate the formation of the crystalline core-shell structure, powder X-ray diffraction (PXRD) patterns (Figures III-6-9) were collected. All characteristic peaks from both the PCN-222 core and UiO shell were found in the PXRD patterns of the core-shell MOFs. The porosity measurements of these materials also corroborate well with the core-shell structures. The N₂ adsorption isotherms (Figures III-10-13) of the core-shell

MOFs were very close to UiO shell, but there is a noticeable hysteresis loop near $P/P_0 = 0.3$ due to the presence of mesoporous core. The scanning electron microscope (SEM) images of PCN-222@Zr-TPDC-2Me (Figure III-14) also reveal that the UiO shell grew as an extension of the PCN-222's crystal lattice to form core-shell structures instead of a mechanical mixture or randomly dispersed "solid solution".

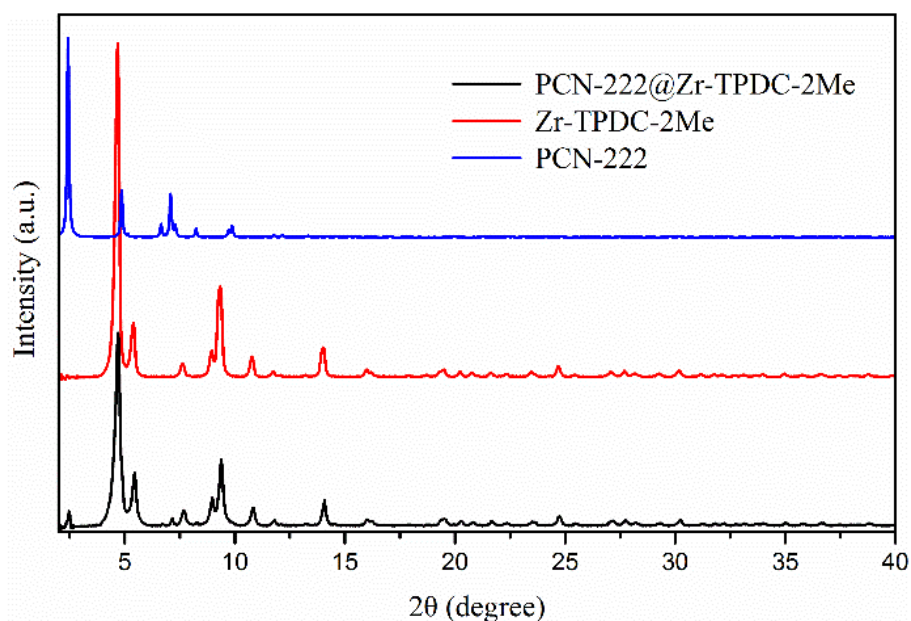


Figure III-6 PXRD patterns of PCN-222, Zr-TPDC-2Me, and PCN-222@Zr-TPDC-2Me

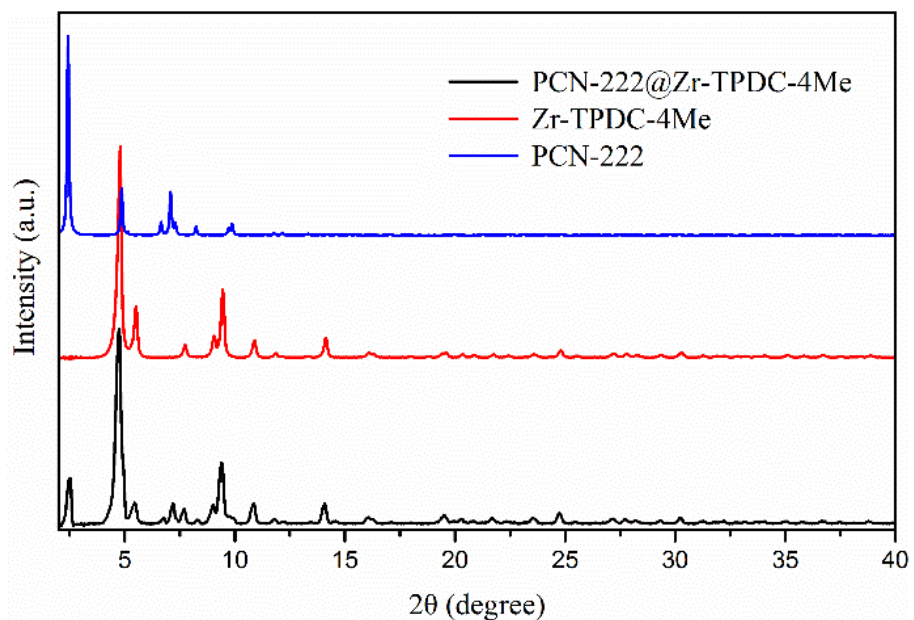


Figure III-7 PXRD patterns of PCN-222, Zr-TPDC-4Me, and PCN-222@Zr-TPDC-4Me

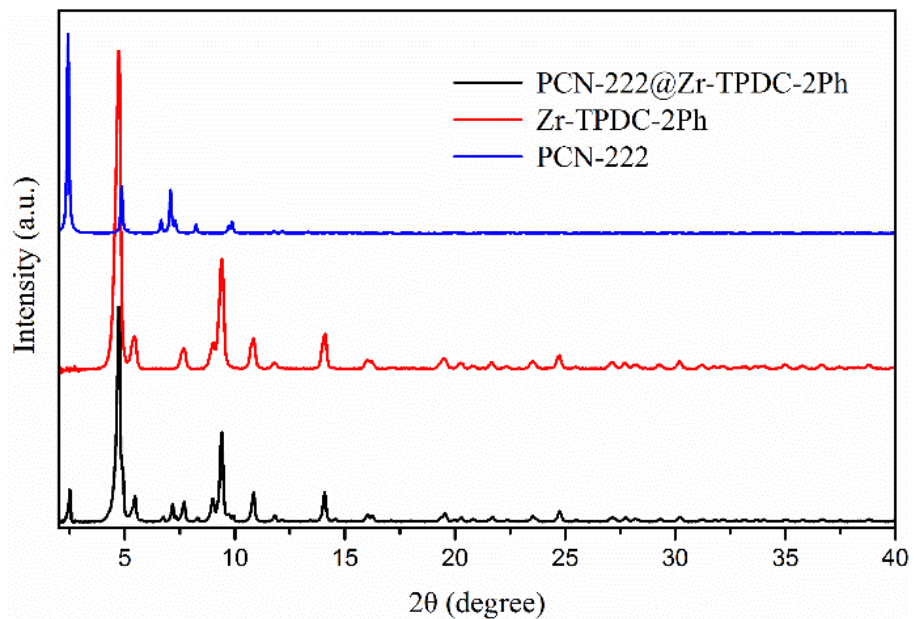


Figure III-8 PXRD patterns of PCN-222, Zr-TPDC-2Ph, and PCN-222@Zr-TPDC-2Ph

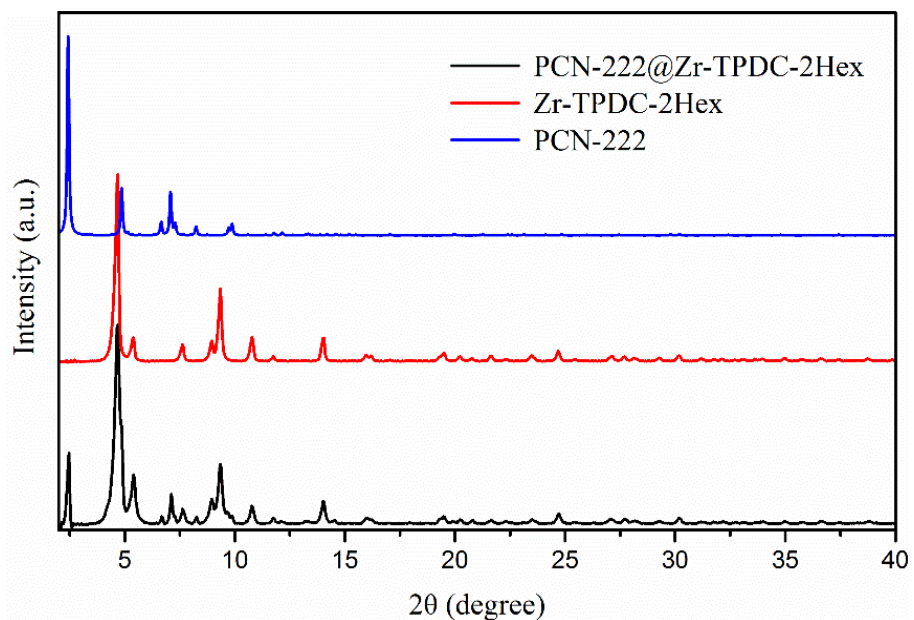


Figure III-9 PXR D patterns of PCN-222, Zr-TPDC-2Hex, and PCN-222@Zr-TPDC-2Hex

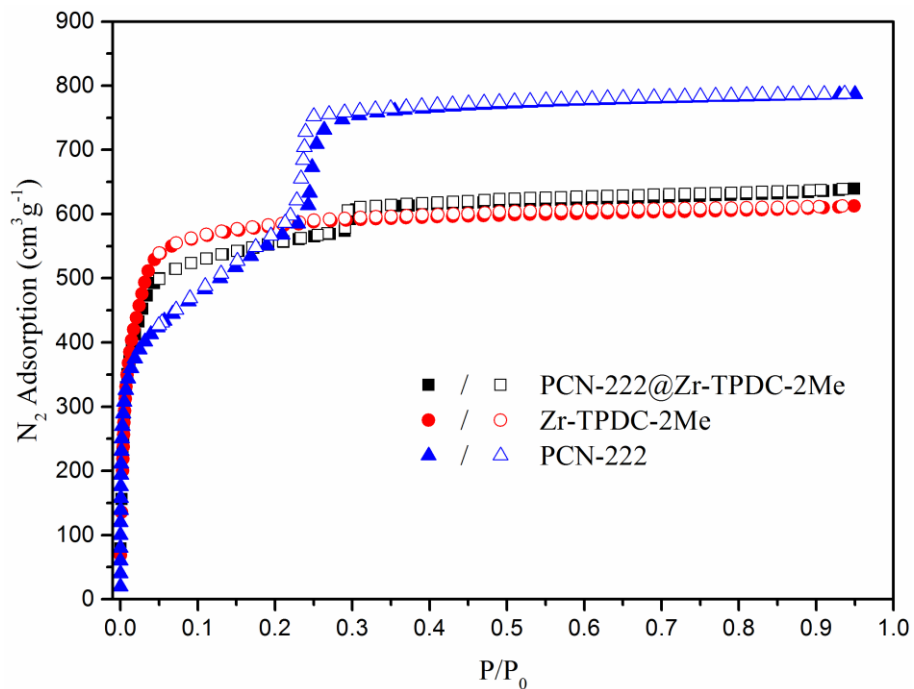


Figure III-10 Gas adsorption isotherms of PCN-222, Zr-TPDC-2Me, and PCN-222@Zr-TPDC-2Me

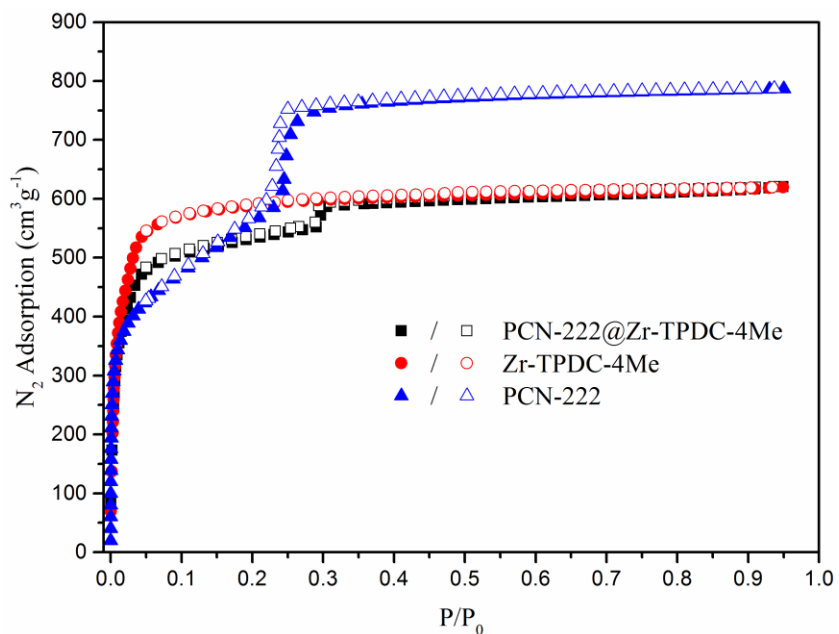


Figure III-11 Gas adsorption isotherms of PCN-222, Zr-TPDC-4Me, and PCN-222@Zr-TPDC-4Me

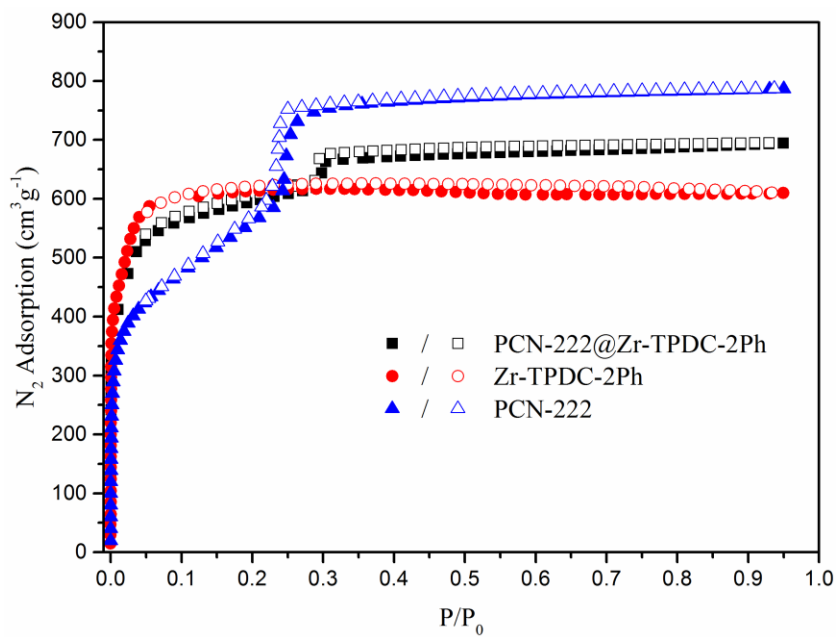


Figure III-12 Gas adsorption isotherms of PCN-222, Zr-TPDC-2Ph, and PCN-222@Zr-TPDC-2Ph

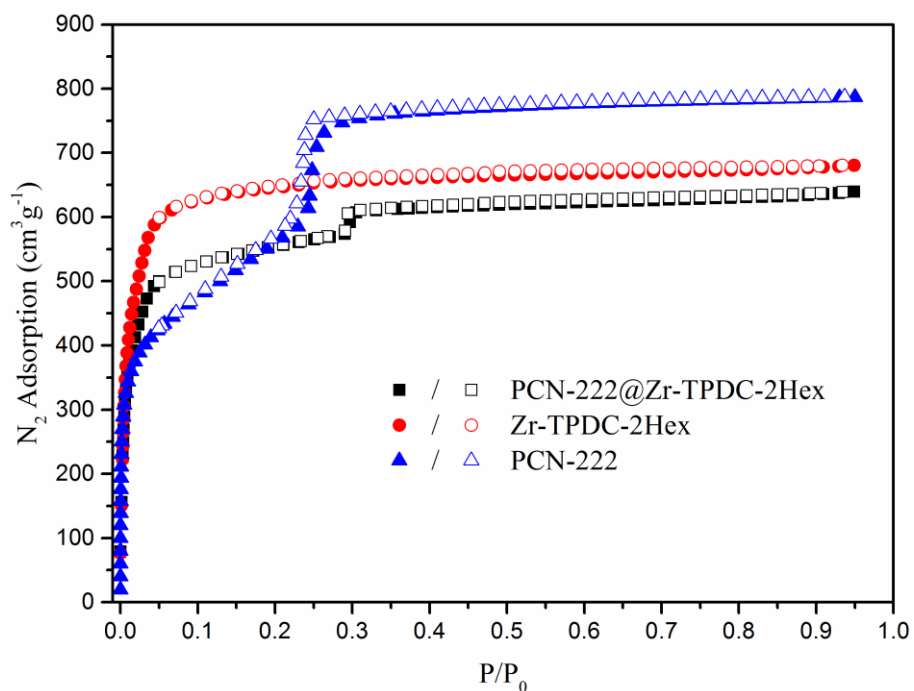


Figure III-13 Gas adsorption isotherms of PCN-222, Zr-TPDC-2Hex, and PCN-222@Zr-TPDC-2Hex

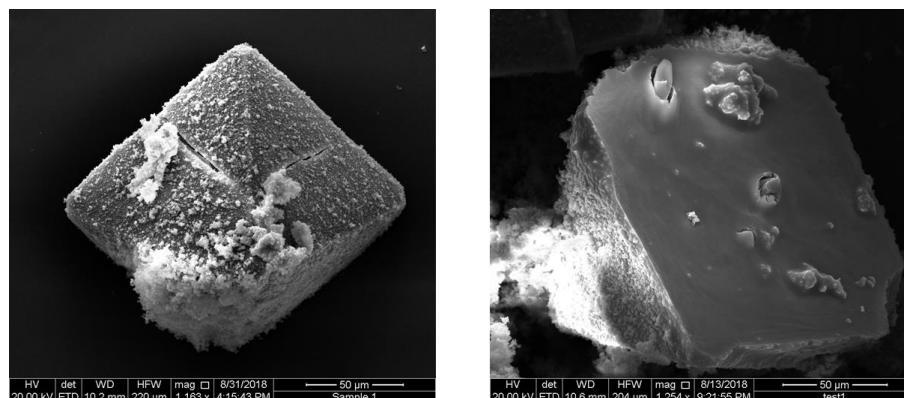

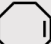
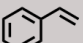
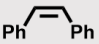

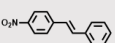


Figure III-14 SEM image of PCN-222@Zr-TPDC-2Me

Olefin epoxidation is an important reaction because epoxides are widely used in the production of epoxy resins, paints, and surfactants and are also intermediates in many organic synthesis. Although many catalytic epoxidation reactions using transition-metal compounds of molybdenum, tungsten, and vanadium have been successfully

demonstrated, the homogeneous catalysts have proved to be of somewhat limited use due to the difficulties in separating the products and contamination by the residual catalyst. Therefore, the immobilization of homogeneous catalysts has attracted a lot of attention. In this case, we used the core-shell MOFs as the catalyst, in which the well-defined pores of MOF catalysts may favor shape and size selectivity, which is difficult to be realized in other systems.

Table III-1 PCN-222(Fe)@Zr-TPDC-2Me, PCN-222(Fe)@Zr-TPDC-4Me, PCN-222(Fe)@Zr-TPDC-2Ph, and PCN-222(Fe)@Zr-TPDC-2Hex catalyzed epoxidation of alkenes^{a,b}

Entry	Substrate	PCN-222(Fe) @Zr-TPDC-2Me	PCN-222(Fe) @Zr-TPDC-4Me	PCN-222(Fe) @Zr-TPDC-2Ph	PCN-222(Fe) @Zr-TPDC-2Hex
1		95	97	97	96
2		87	89	74	69
3		91	83	68	72
4		78	68	31	19
5		72	58	24	8
6		59	55	17	13

^a Reaction conditions: Olefin (500 mM), O₂, catalyst (5 mM, based on PCN-222(Fe)) and acetonitrile (5.0 mL) sealed in a Teflon-lined screw cap vial were stirred at room temperature for 24h.

^b Conversion was determined by ¹H NMR with 1,4-dibromobenzene as the internal standard.

The catalytic performances of the PCN-222(Fe)@Zr-TPDC-2Me, PCN-222(Fe)@Zr-TPDC-4Me, PCN-222(Fe)@Zr-TPDC-2Ph, and PCN-222(Fe)@Zr-TPDC-2Hex in the epoxidation of various olefins with different steric sizes were evaluated. As shown in the Table III-1, with the increasing of the size of substrates and with the

increasing of the size of substituents on linear linker, the conversion of the alkene decrease, which shows the catalytic selectivity of the core-shell MOFs.

To demonstrate the generality of the kinetically controlled strategy, three additional sets of core-shell MOFs with mismatching lattice were constructed (PCN-134@Zr-BTB, PCN-222@Nu-1000, and La-TCPP@La-BPDC, BTB = benzene tribenzoate). First, we show that our synthetic method can be applied to mixed-linker MOFs and 2D-MOFs. PCN-134^[16] is a mixed-linker Zr-MOF constructed from 3-connected BTB and 4-connected TCPP linkers with a 3D layer-pillar structure. Zr-BTB is a 2D MOF with 6-connected Zr-cluster and BTB linker.^[17] From the optical microscopic image (Figure III-15), the core and shell MOFs can clearly be distinguished. The cores (PCN-134) consisted of red hexagonal crystals and the shells (Zr-BTB) were colorless hexagonal crystals. The composition and crystallinity of the core-shell MOF were identified by PXRD patterns (Figure III-16). All characteristic peaks from both PCN-134 and Zr-BTB were found in the PXRD patterns, demonstrating the highly crystalline nature of core-shell MOF, PCN-134@Zr-BTB. The N₂ adsorption isotherm (Figure III-17) also confirm the core-shell structure of PCN-134@Zr-BTB. In addition, two linkers with the same connectivity can also form core-shell MOFs guided by nucleation kinetics. PCN-222 and Nu-1000 are all based on tetratopic linkers and 8-connected Zr-clusters. However, the nucleation PCN-222 is faster than that of Nu-1000, which affords the formation of PCN-222@Nu-1000 (Figures III-18-19). More importantly, La-TCPP@La-BPDC (Figures III-20-21) were constructed indicating that the synthetic strategy is not merely

limited to Zr-MOFs.^[18] Similar to the PCN-222@Zr-BPDC system, the La-TCPP was initially formed as the core, which induced the growth of La-BPDC shell.

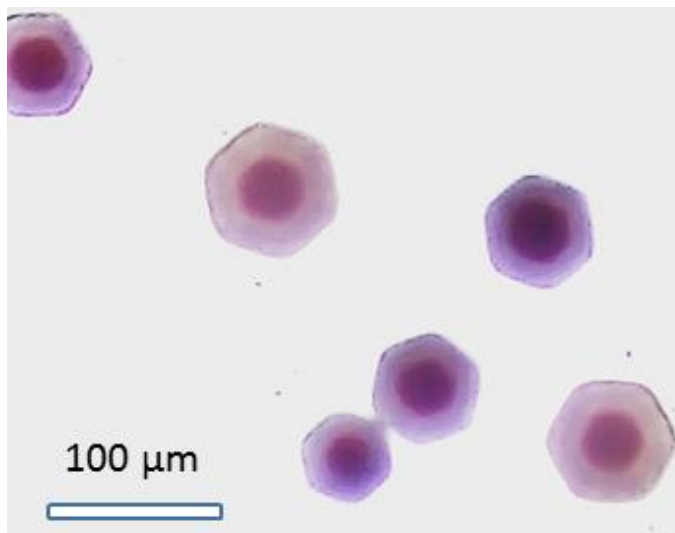


Figure III-15 Optical image of PCN-134@Zr-BTB.

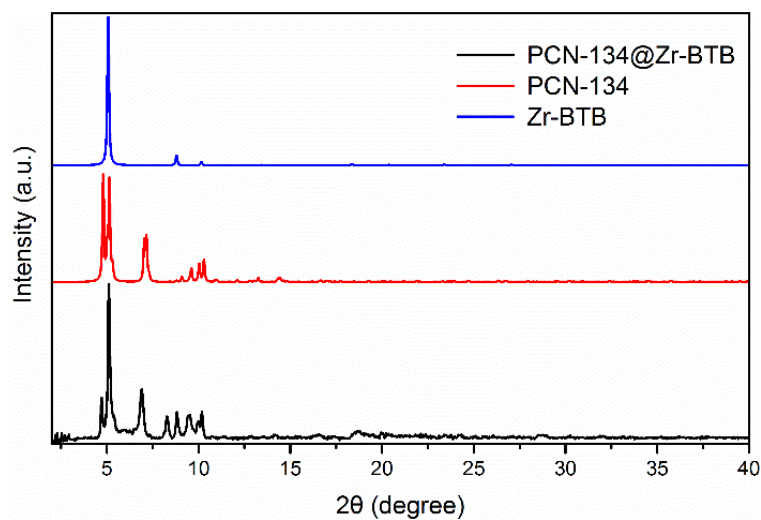


Figure III-16 PXRD patterns of Zr-BTB, PCN-134 and PCN-134@Zr-BTB.

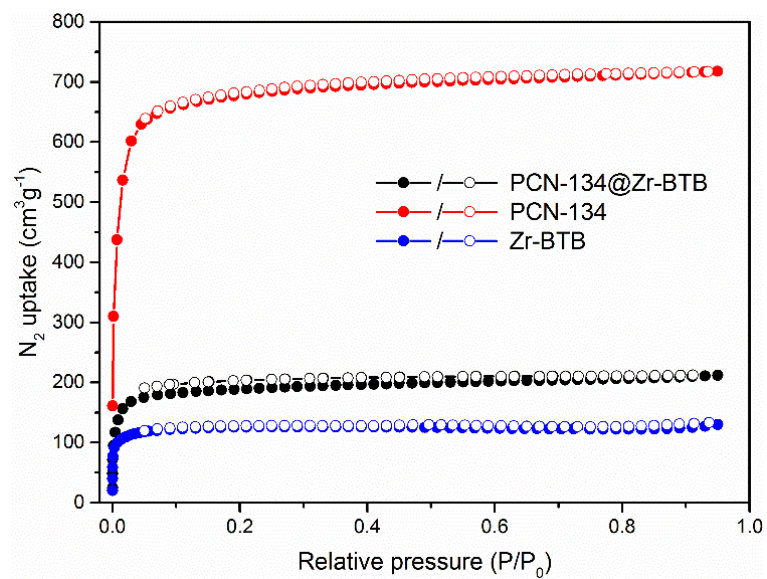


Figure III-17 Gas adsorption isotherms of Zr-BTB, PCN-134 and PCN-134@Zr-BTB.

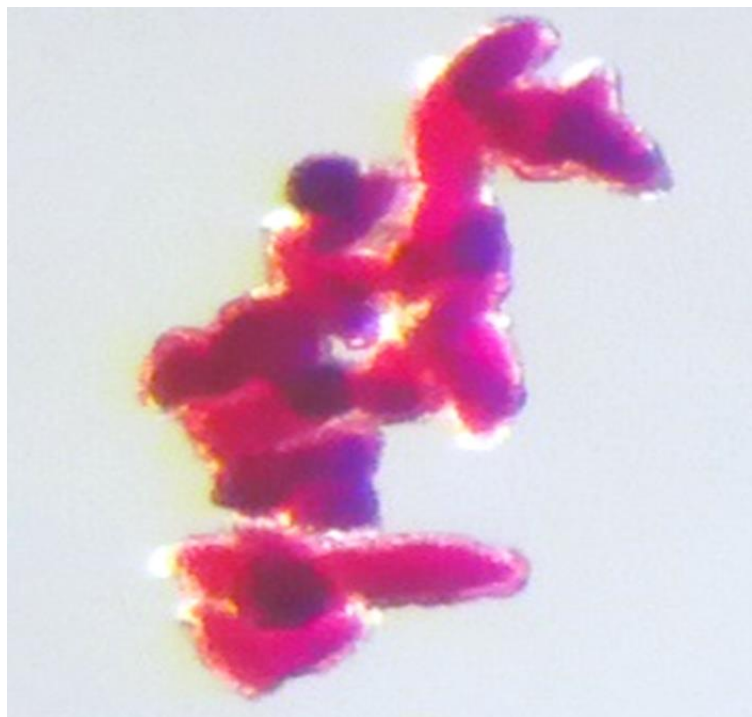


Figure III-18 Microscopic image of PCN-222@Nu-1000.

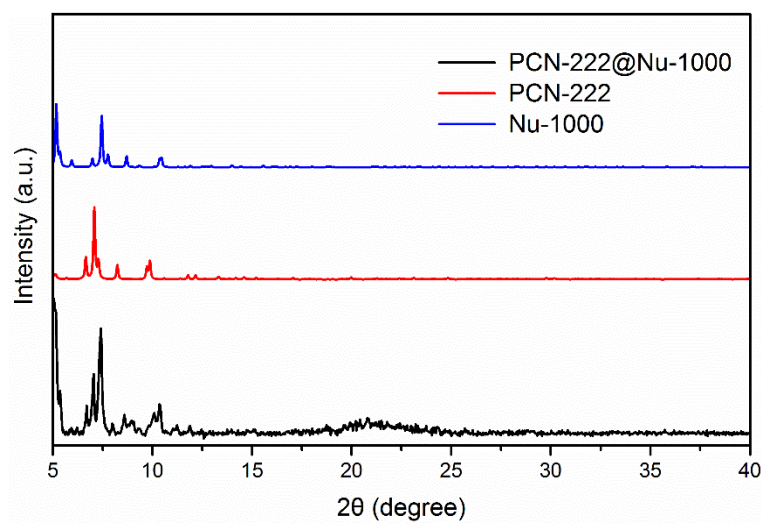


Figure III-19 PXRD patterns of Nu-1000, PCN-222 and PCN-222@Nu-1000.

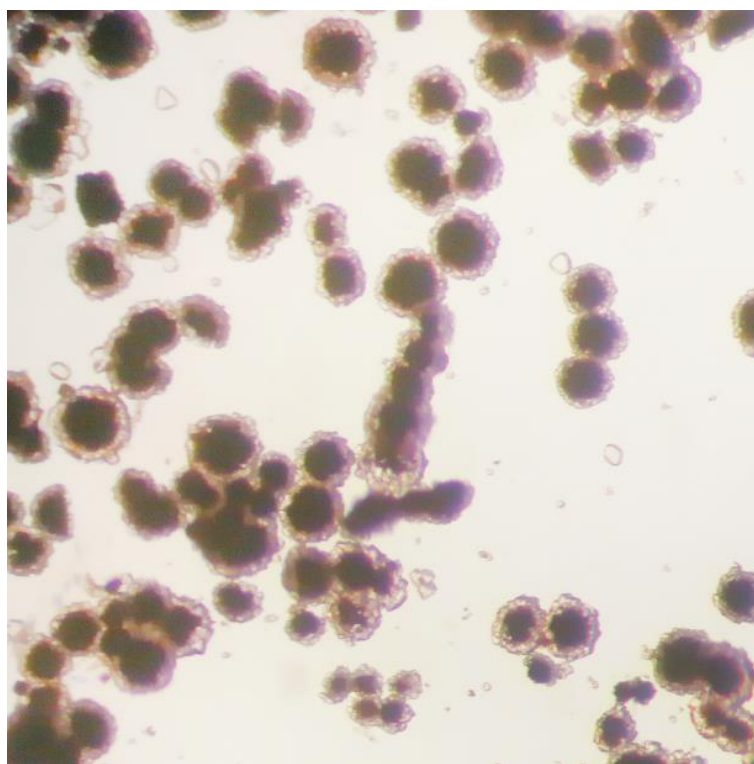


Figure III-20 Microscopic image of La-TCPP@La-BPDC.

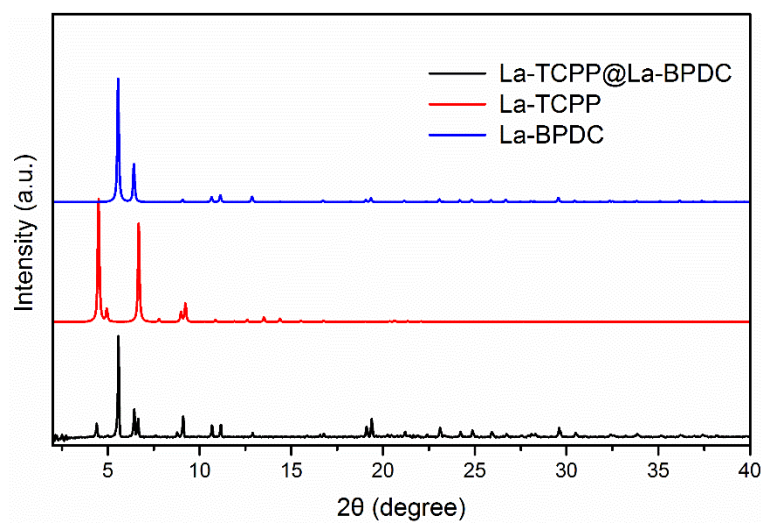


Figure III-21 PXRD patterns of La-BPDC, La-TCPP and La-TCPP@La-BPDC.

3.4 Conclusion

Therefore, the kinetically controlled strategy is a facile and general method to construct mismatching core-shell MOFs through one-step synthesis. Nevertheless, the core MOF and shell MOF are required to have the same metal and similar synthetic conditions. Based on work presented here, core-shell MOFs with the same metal can be synthesized through the control of nucleation kinetics. However, as shown in Zn-MOF@Cu-MOF reported by Kitagawa and co-workers,¹⁷¹ it is possible to extend the one-pot nucleation kinetic control strategy to synthesize hybrid core-shell MOFs with different kinds of metals, which will enrich the synthetic methods of core-shell MOFs. Research along this line is currently under way.

CHAPTER IV

ANCHOR INSTALLATION ON POROUS POLYMER NETWORKS (PPNS) FOR HIGH CO₂ UPTAKE³

4.1 Introduction

With the rapid increase of the global population and the industrialization, the consumption of energy is growing explosively. Currently over 85% of the global energy demand is being supported by fossil fuels, which will continue to play an important role in the foreseeable future.¹⁷⁵⁻¹⁷⁸ The burning of the fossil fuels releases large amounts of CO₂ into the atmosphere, which has made the CO₂ concentration in the atmosphere increase from 280 ppm to 390 ppm since the beginning of the industrial age.¹⁷⁹⁻¹⁸² The increase of the CO₂ concentration affects the incoming and outgoing energy in the atmosphere, resulting in an increase of the average atmospheric temperature. Though researchers are exploring cleaner forms of energy (such as solar energy and hydrogen)¹⁸³⁻¹⁸⁵ to replace the fossil fuels, these are far from practical application. Subsequently, strategies for carbon capture and sequestration (CCS) are urgently required.^{186, 187} CCS is a family of technologies, which can reduce CO₂ emissions. So far, a growing number of fully integrated CCS projects have reached pilot prior to commercialization. However, the large energy penalty and considerable cost of the carbon capture process are slowing down the deployment of commercial CCS projects.

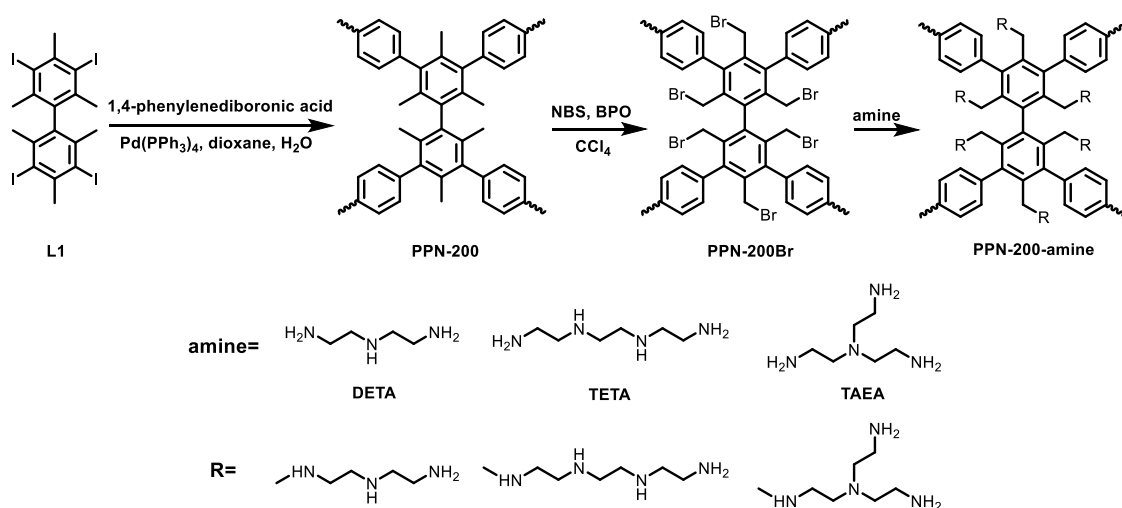
³ Part of this chapter is reproduced with permission from “Anchor Installation on Porous Polymer Networks (PPNs) for High CO₂ Uptake” by Yang, X.; Zou, L.; Zhou, H.-C. *Polymer*, 126 (2017) 303-307, copyright 2017 by Elsevier Ltd.

In real applications, the combustion of fossil fuels in air generates flue gas consisting of a majority of N₂ with 15% CO₂ and other minor components such as H₂O, CO, NO_x and SO_x; thus, CO₂-uptake capacity at about 0.15 bar is more relevant to realistic postcombustion applications. Aqueous alkanolamines, such as monoethanolamine (MEA) solutions, have been utilized as postcombustion “wet scrubbing” methods in power plants due to their large CO₂ capacity and selectivity. However, this method suffers from many complications, such as high regeneration energy, toxicity and the corrosive nature of amines.

As an alternative choice, the solid porous materials are very promising for CCS since they can overcome the downsides of aqueous alkanolamine solutions. During the past decades, metal–organic frameworks (MOFs) have been studied extensively due to their high surface area, tunable pore size, adjustable functionalities and the potential in gas adsorption and separation.^{119, 188, 189} MOFs have well-defined structures and in many cases, these structures are robust enough to allow the removal of included guest species, resulting in permanent porosity. The crystallinity of MOFs also allows precise structural characterization by diffraction methods, thus facilitating their rational design and the formulation of structure-function relationships. Even though some MOFs with high densities of open metal sites (Mg-MOF-74) or high amounts of amine loading (mmen-MOF-74) have shown high CO₂ uptakes, the practical application of most MOFs is limited by their poor physicochemical stability and, particularly, by sensitivity to water.¹⁹⁰⁻¹⁹²

PPNs are another class of very promising candidate materials for carbon capture, which are constructed from rigid monomers through covalent bonds and possess

permanent porosity.¹⁹³⁻¹⁹⁶ Due to their covalent connections, PPNs normally display exceptional chemical and water stability, enabling them to be easily functionalized by pre-synthetic or post-synthetic methods. The introduction of alkylamines into PPNs can significantly enhance the CO₂ adsorption and CO₂/N₂ selectivity by utilizing the polarizability and quadrupole moment of CO₂, which have been demonstrated by Zhou and co-workers.¹⁹³ Nevertheless, till now, there are few works that present novel methods of introducing alkylamines into PPNs.



Scheme IV-1 The synthetic route of PPN-200amines.

Herein, a novel post-synthetic strategy was designed to construct a series of alkylamine tethered PPNs, which demonstrated high carbon capture capability and CO₂/N₂ selectivity. First, PPN-200 was synthesized by Suzuki-Miyaura cross-coupling reaction using L1 and 1,4-phenylenediboric acid. The default diamondoid framework topology (dia topology) constructed by the combination of tetrahedral unit and linear unit provides widely open and interconnected pores to efficiently eliminate the “dead space”. More importantly, the extremely robust scaffold of PPN-200 makes it an ideal platform

for introducing CO₂-philic groups under harsh reaction conditions. By reaction with N-bromosuccinimide (NBS), PPN-200 was modified to give PPN-200Br. The methylbromide groups can be further substituted by alkylamines (diethylenetriamine (DETA), triethylenetetramine (TETA) and tris(2-aminoethyl)amine (TAEA)) to produce PPN-200-amines (PPN-200-DETA, PPN-200-TETA and PPN-200-TAEA) (Scheme IV-2). The resulting alkylamine tethered PPN-200s showed significant increases in CO₂ uptake capacities (~55 cm³/g at 298 K and 1 bar) and high CO₂/N₂ selectivity (289).

4.2 Experimental Section

4.2.1 Materials and Instrumentation

4.2.1.1 Materials

All chemicals were purchased from Sigma-Aldrich or Acros Organics and were used as received without further purification.

4.2.1.2 Instrumentation

Fourier transform infrared measurements (FT-IR) were performed on a SHIMADZU IR Affinity-1 spectrometer. Nuclear magnetic resonance (NMR) data were collected on a Mercury 300 spectrometer. N₂ and CO₂ adsorption–desorption isotherms were measured using a Micromeritics ASAP 2020 system at different temperatures. Powder X-ray diffraction (PXRD) was performed with a BRUKER D8-Focus Bragg–Brentano X-ray powder diffractometer equipped with a Cu sealed tube ($\lambda = 1.54178 \text{ \AA}$) at 40 kV and 40 mA. Thermogravimetric analysis (TGA) was conducted on a TGA-50 (SHIMADZU) thermogravimetric analyzer from room temperature to 600 °C at a ramp rate of 5 °C/min in a flowing nitrogen atmosphere. Scanning electron microscope (SEM) was performed on QUANTA 450 FEG and energy dispersive X-ray spectroscopy (EDS) was carried out by X-Max20 with Oxford EDS system equipped with X-ray mapping

4.2.2 Ligand Synthesis

4.2.2.1 Synthesis of 2,2',4,4',6,6'-hexamethylbiphenyl.

To a 1000 mL three-necked flask containing 7 g of magnesium pieces, degassed anhydrous THF (600 mL) and a pinch of iodine were added under a nitrogen atmosphere. The resulting mixture was heated to 80 °C, and then 2-bromomesitylene (35 mL) was added dropwise. The reaction mixture was refluxed for another 3 h. After it was cooled down to room temperature, a mixture of anhydrous FeCl₃ (1.1 g), 1, 2-dibromoethane (12 mL), and anhydrous THF (15 mL) under a nitrogen atmosphere. Stirring was continued for another 1 h, and then the reaction was quenched by the addition of hydrochloric acid. Organic solvents were evaporated under reduced pressure. The residue was extracted with dichloromethane. The dichloromethane phase was dried over anhydrous MgSO₄, and filtered. Most of dichloromethane was removed under reduced pressure, and then methanol was added. 2,2',4,4',6,6'-hexamethylbiphenyl was collected as colorless solid. (17 g, 62.5% yield). ¹H NMR (300 MHz, CDCl₃) δ: 6.93 (s, 4H), 2.33 (s, 6H), 1.86 (s, 12H).

4.2.2.2 Synthesis of 3,3',5,5'-tetraiodo-2,2',4,4',6,6'-hexamethylbiphenyl

To a mixture of 2,2',4,4',6,6'-hexamethylbiphenyl (4.0 g), solid iodine (7.0 g), H_5IO_6 (3.1 g) in a 500 mL flask, add $\text{CH}_3\text{COOH}/\text{H}_2\text{O}/\text{H}_2\text{SO}_4$ (240/48/7.2 mL). The resulting mixture was stirred at 90 °C for 3 days. The reaction mixture was diluted with a large amount of water. The precipitate was filtered and washed with water. The pink solid was collected and dissolved in CHCl_3 , then washed with saturated $\text{Na}_2\text{S}_2\text{O}_3$ solution to remove iodine residue. The organic phase was dried over anhydrous MgSO_4 , filtered, and evaporated under reduced pressure to produce 3,3',5,5'-tetraiodo-2,2',4,4',6,6'-hexamethylbiphenyl as a white solid (10.6 g, 85% yield). ^1H NMR (300 MHz, CDCl_3) δ : 2.05 (s, 12 H), 3.02 (s, 6 H).

4.2.3 PPN Synthesis

4.2.3.1 Synthesis of PPN-200

3,3',5,5'-tetraiodo-2,2',4,4',6,6'-hexamethylbiphenyl (148.2 mg) and 1,4-phenylenediboronic acid (66.4 mg) in dioxane/water (18 ml/2 ml) and Pd(PPh₃)₄ (20mg). The mixture was stirred at 100 °C under N₂ atmosphere for 48h. After cooling to room temperature, the mixture was filtered and the solid was washed by DMF (30 ml × 3), methanol (30 ml × 3), H₂O (30 ml × 3), acetone (30 ml × 3) and dried in vacuo to get PPN-200 (71.4 mg, 92.4%) as white solid.

4.2.3.2 Synthesis of PPN-200Br

PPN-200 (280 mg), N-bromosuccinimide (0.852 g) and benzoyl peroxide (100 mg) in anhydrous CCl₄ (150ml) and the mixture was refluxed for 48h. After cooling to room temperature, the mixture was filtered and the solid was washed with DMF (30 ml × 3), methanol (30 ml × 3), H₂O (30 ml × 3), acetone (30 ml × 3) and dried in vacuo to get PPN-200Br (380 mg, 28%).

4.2.3.3 Synthesis of PPN-200-DETA

PPN-200Br in 20 ml DETA was heated to 90 °C for 72h. The resulting solid was centrifuged and washed with DMF (30 ml × 3), methanol (30 ml × 3), H₂O (30 ml × 3), acetone (30 ml × 3) and then dried in vacuo. (PPN-200-DETA, yield 85%)

4.2.3.4 Synthesis of PPN-200-TETA

PPN-200Br in 20 ml TETA was heated to 90 °C for 72h. The resulting solid was centrifuged and washed with DMF (30 ml × 3), methanol (30 ml × 3), H₂O (30 ml × 3), acetone (30 ml × 3) and then dried in vacuo. (PPN-200-TETA, yield 81%)

4.2.3.5 Synthesis of PPN-200-TAEA

PPN-200Br in 20 ml TAEA was heated to 90 °C for 72h. The resulting solid was centrifuged and washed with DMF (30 ml × 3), methanol (30 ml × 3), H₂O (30 ml × 3), acetone (30 ml × 3) and then dried in vacuo. (PPN-200-TAEA, yield 96%)

4.2.4 Calculation of CO₂/N₂ Selectivity

4.2.4.1 The Single Isotherm Selectivity

The selectivity of CO₂/N₂ of PPN-200 in flue gas conditions was evaluated from the composition of flue gas where the partial pressure for CO₂ is 0.15 bar and N₂ is 0.85 bar. The uptake of CO₂ at 0.15 bar and N₂ at 0.85 bar were estimated by linear interpolation, and the selectivity is calculated by using Eq. 1.

$$Selectivity = \frac{Q_{CO_2}/Q_{N_2}}{P_{CO_2}/P_{N_2}} \quad \text{Eq. 1}$$

In Eq. 1, Q indicates the quantity of the absorbents, while P indicates the partial pressure.

4.3 Results and Discussion

A high surface area is critical for PPN-200 to investigate its properties and is also essential for postsynthetic modification. So we first optimized the synthetic conditions of PPN-200 by a series of control experiments (Figures IV-1-3, Table IV-1). The first series of experiments were designed to determine an appropriate solvent system. We chose different ratios of dioxane and water as solvents, ranging from 20:0, 18:2, 16:4, 14:6, 12:8 to 10:10. As shown in Figure IV-1, to obtain a porous polymer, it was essential to utilize a mixture of dioxane and water. If pure dioxane was used, we only observed nonporous polymers, whose N_2 adsorption was very close to 0, due to the poor solubility of base in dioxane. But, if too much water was used, the decreasing solubility of L1 in the mixed solvent led to the decreased N_2 adsorption of PPN-200, which peaked at the ratio of 18:2. After determining a suitable solvent, the next step was to optimize the type and amount of base. From the Figure IV-2 and Figure IV-3, we can see that the porosities of PPN-200 synthesized by using CsF were much higher than those with K_2CO_3 . With the increase of the amount of CsF, the N_2 adsorption of PPN-200 increased and peaked at 10 equivalents; after that, the N_2 adsorption decreased as more CsF was used (Figure IV-3).

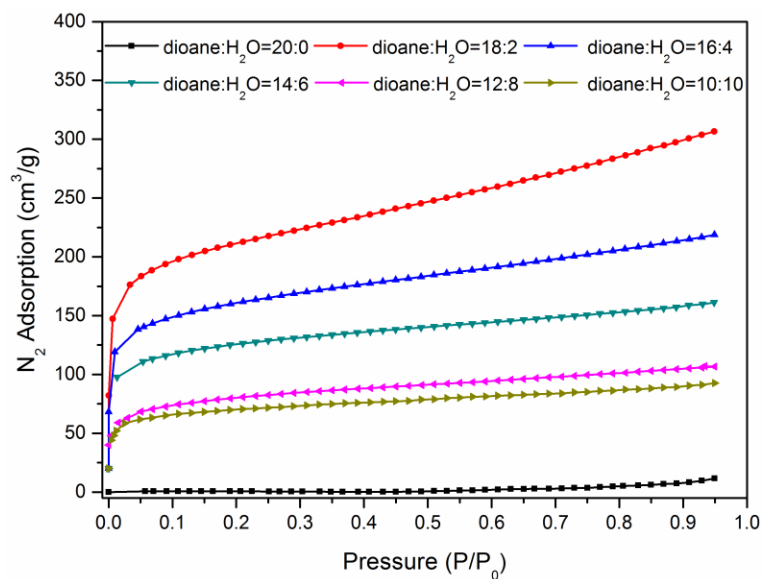


Figure IV-1 N₂ sorption at 77 K with changing solvent.

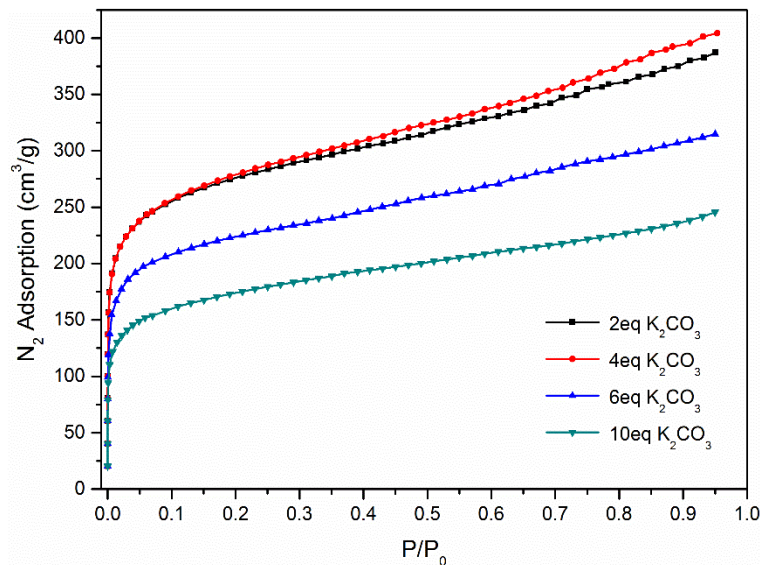


Figure IV-2 N₂ sorption at 77 K with different amount of K₂CO₃.

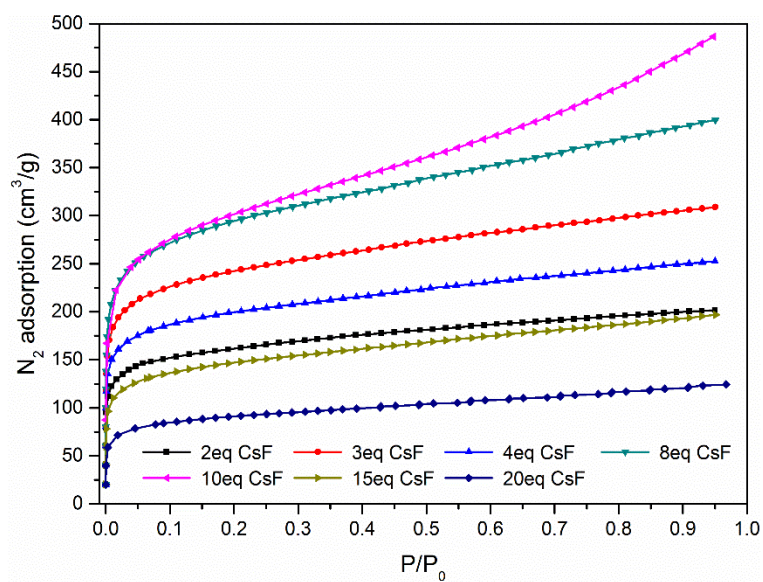


Figure IV-3 N₂ sorption at 77 K with different amount of CsF.

Table IV-1 N₂ adsorption capabilities of PPN-200 under different conditions.

Dioxane:H ₂ O	N ₂ Adsorption (cm ³ g ⁻¹)	K ₂ CO ₃	N ₂ Adsorption (cm ³ g ⁻¹)	CsF	N ₂ Adsorption (cm ³ g ⁻¹)
20: 0	11	2 eq	387	2 eq	201
18: 2	306	4 eq	404	3 eq	308
16: 4	218	6 eq	314	4 eq	252
14: 6	161	10 eq	246	8 eq	399
12: 8	107			10 eq	486
10: 10	92			15 eq	197
				20 eq	124

By combining best synthetic conditions, we determined the PPN-200 with highest N₂ adsorption (486 m³/g) under 1 bar with an adsorption/desorption hysteresis loop (Figure IV-4). Its Langmuir surface area, Brunauer-Emmett-Teller (BET) surface area, and pore volume are 1483 m²/g, 944 m²/g, and 0.48 cm³/g, respectively. Its pore size distribution was calculated by the Density Functional Theory (DFT) method (Figure IV-5). Its pore diameters are widely distributed from 10 Å to more than 60 Å, and no pattern could be identified from the pore size distribution plot, which implies the amorphous nature of PPN-200. This can also be confirmed by powder X-ray diffraction (PXRD) pattern (Figure IV-6) and scanning electron microscope (SEM) (Figures IV-7-11). The most prominent pores have diameters of 11 Å and 14 Å, which is consistent with the microporous nature of PPN-200.

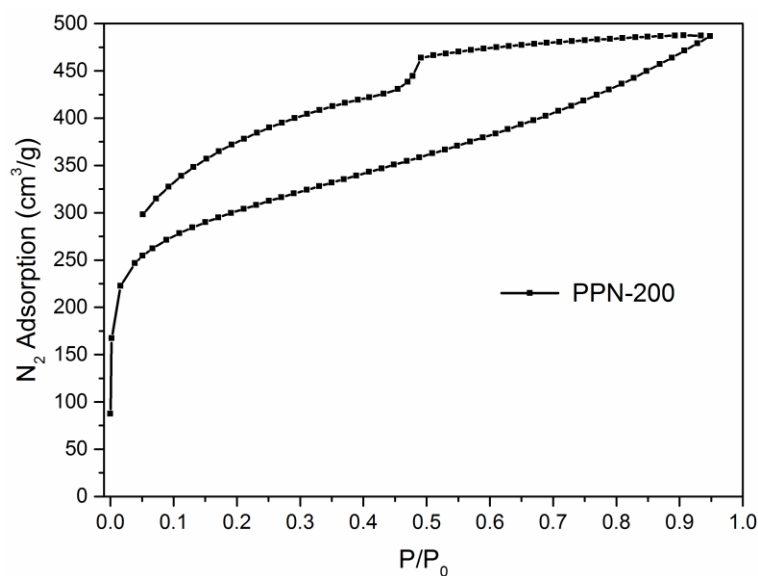


Figure IV-4 N₂ isotherm of optimized PPN-200.

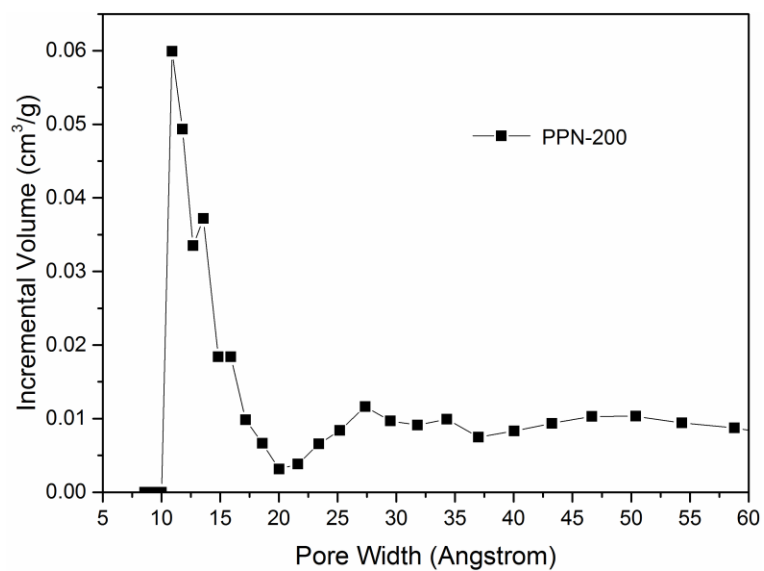


Figure IV-5 Pore size distribution of PPN-200.

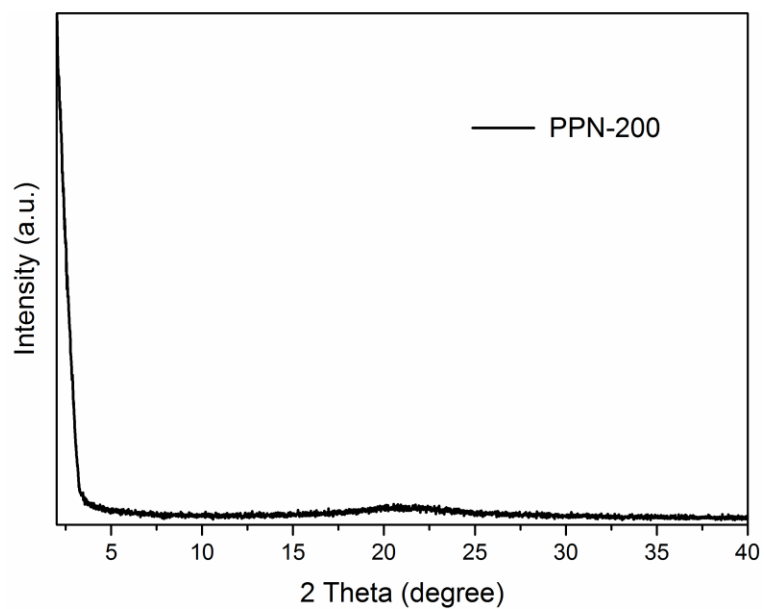


Figure IV-6 The PXRD pattern of the fresh PPN-200.

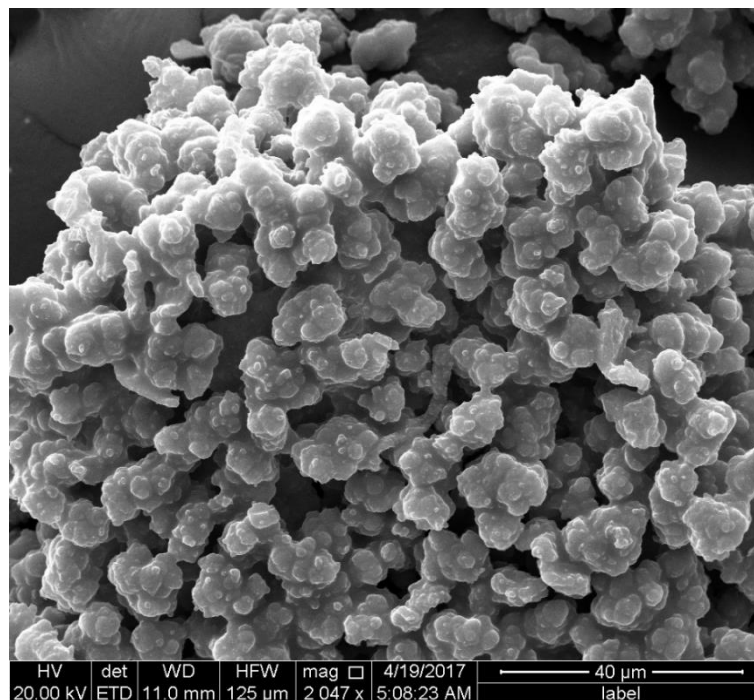


Figure IV-7 SEM image of PPN-200.

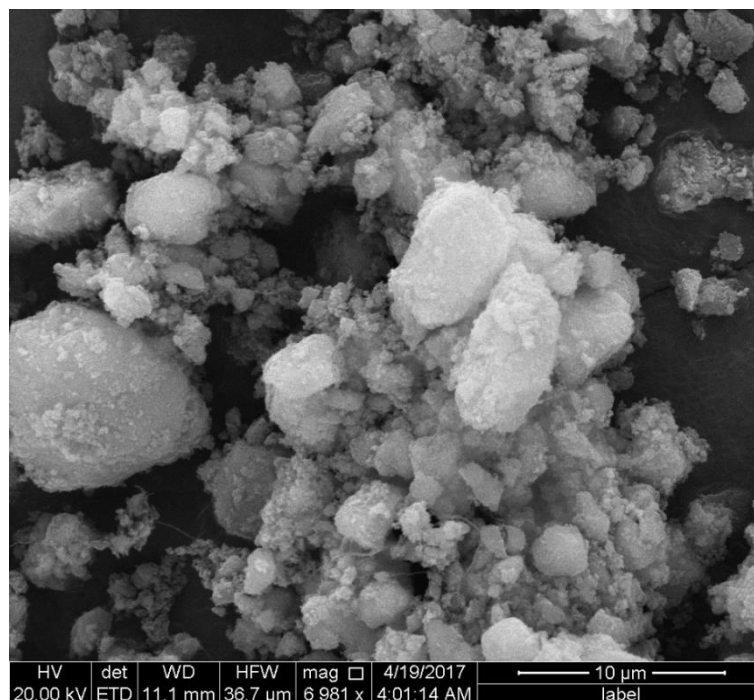


Figure IV-8 SEM image of PPN-200Br.

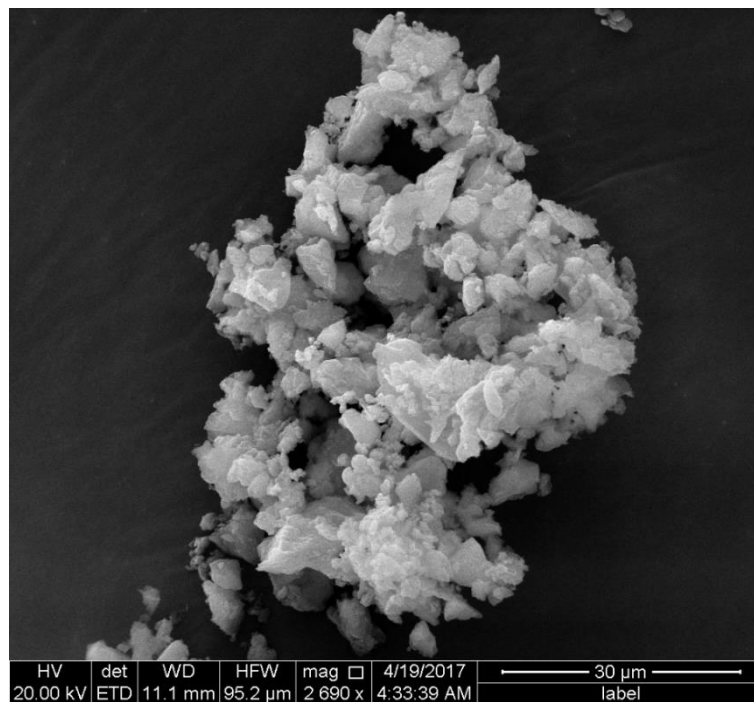


Figure IV-9 SEM image of PPN-200-DETA.

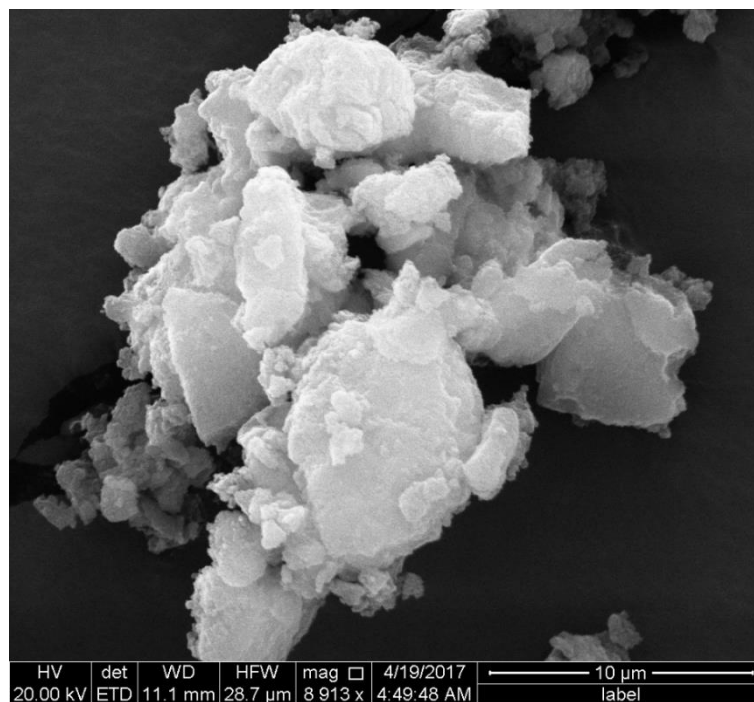


Figure IV-10 SEM image of PPN-200-TETA.

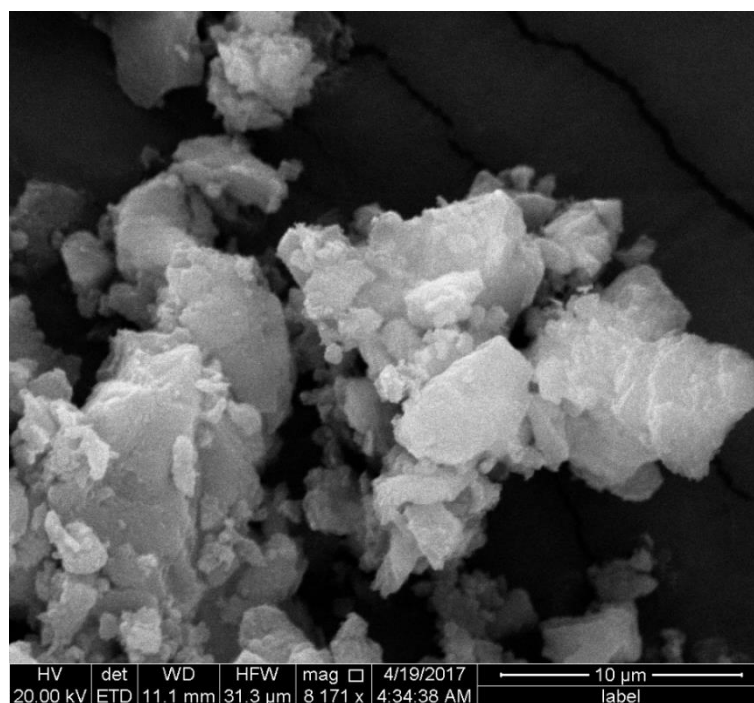


Figure IV-11 SEM image of PPN-200-TAEA.

After acquiring the highly porous PPN-200, we brominated it by using NBS to form the active intermediate PPN-200Br, which followed by substitution with excess alkylamines to yield PPN-200-amines (PPN-200-DETA, PPN-200-TETA and PPN-200-TAEA). The PPN-200Br and PPN-200-amines showed dramatic decreases in N_2 uptake (Figure IV-12), which confirm that the functionalization occurs within the cavities. The occurrence of amine substitution was confirmed by TGA (Figures IV-13-17), EDS (Table IV-2) and infrared spectroscopy (IR) (Figure IV-18), from which we can clearly find there was a broad peak (from 3100 to 3500 cm^{-1}) belonging to alkylamines. The introduction of amine groups into PPN-200 resulted in materials with excellent CO_2 adsorption at 298 K and low pressures (Figure IV-19). The trend of improvement in CO_2 adsorption under low pressure (0.15 bar) in terms of tethered amine groups was $TAEA > TETA > DETA$.

Though the PPN-200-TAEA has the lowest N₂ adsorption, it presents the highest CO₂ adsorption of all amine-tethered PPN-200s, which indicates the CO₂ uptake capacity is closely related to the amount of amine instead of the surface area. PPN-200-TAEA exhibits high CO₂ adsorption: 42 cm³/g (8.3 wt%) at 298 K and 0.15 bar and 55 cm³/g (10.9 wt%) at 298 K and 1 bar. The CO₂/N₂ selectivity of PPN-200-TAEA in flue gas conditions was evaluated by the ratio of the adsorbed gas quantity where the partial pressure for CO₂ is 0.15 bar and N₂ is 0.85 bar. The calculated single-component CO₂/N₂ selectivity of PPN-200-TAEA in flue gas at 298 K is 289 that is significantly larger than other N-riched PPNs. (Figure IV-20)

Table IV-2 Element characterization of PPN-200Br, PPN-200-DETA, PPN-200-TETA, and PPN-200-TAEA.

	PPN-200Br	PPN-200-DETA	PPN-200-TAEA	PPN-200-TETA
C (wt%)	72.76	70.03	78.07	75.69
O (wt%)	3.53	11.01	8.99	7.83
N (wt%)		15.54	12.14	12.02
Br (wt%)	23.71	3.50	0.79	4.46

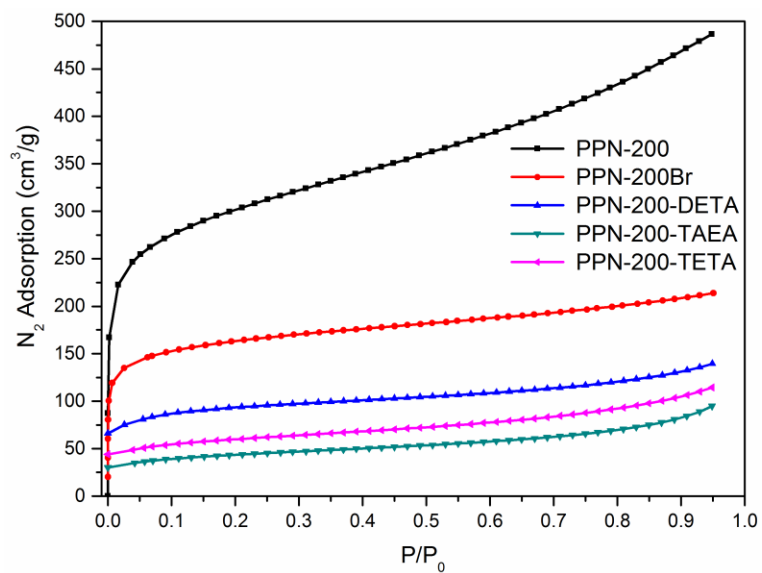


Figure IV-12 N₂ isotherms of PPN-200, PPN-200Br, and PPN-200-amines.

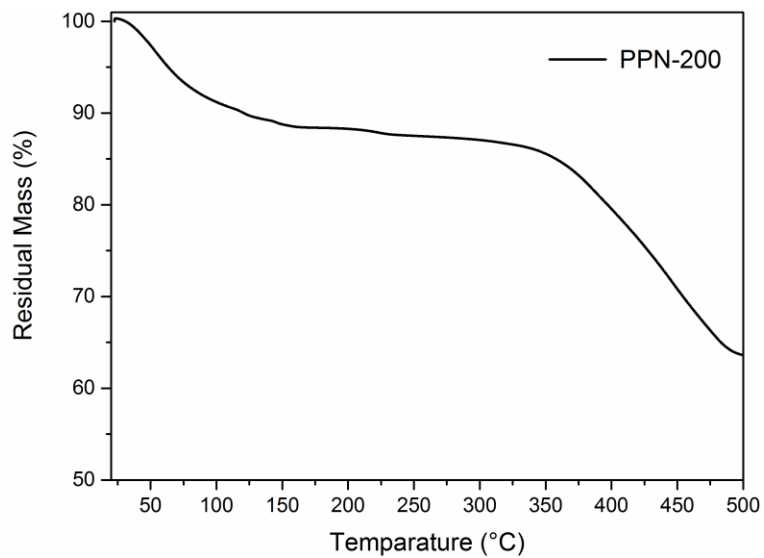


Figure IV-13 TGA of PPN-200.

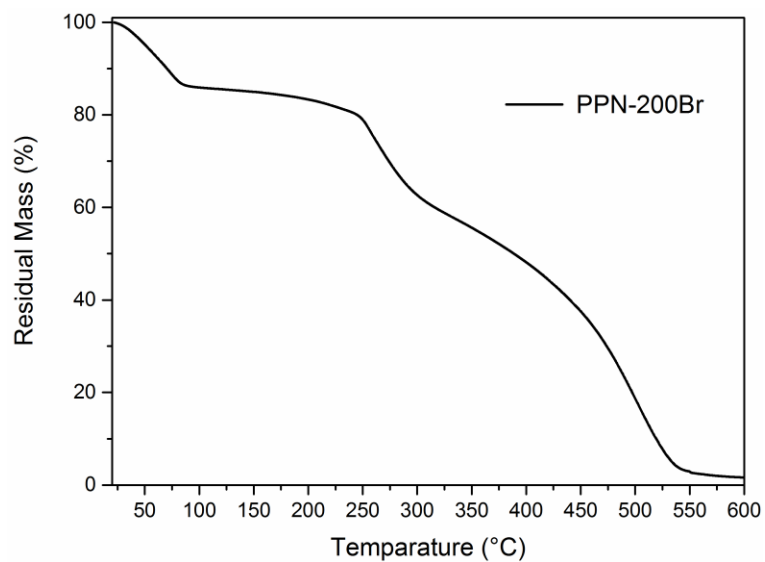


Figure IV-14 TGA of PPN-200Br.

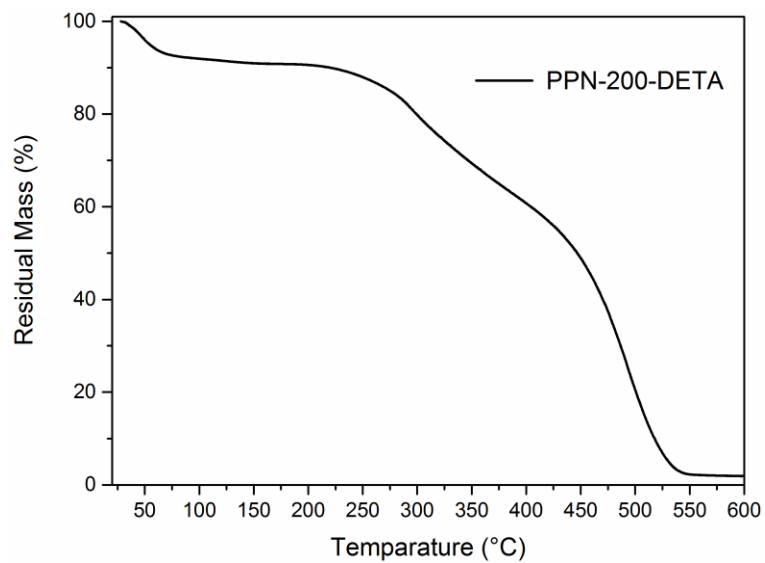


Figure IV-15 TGA of PPN-200-DETA.

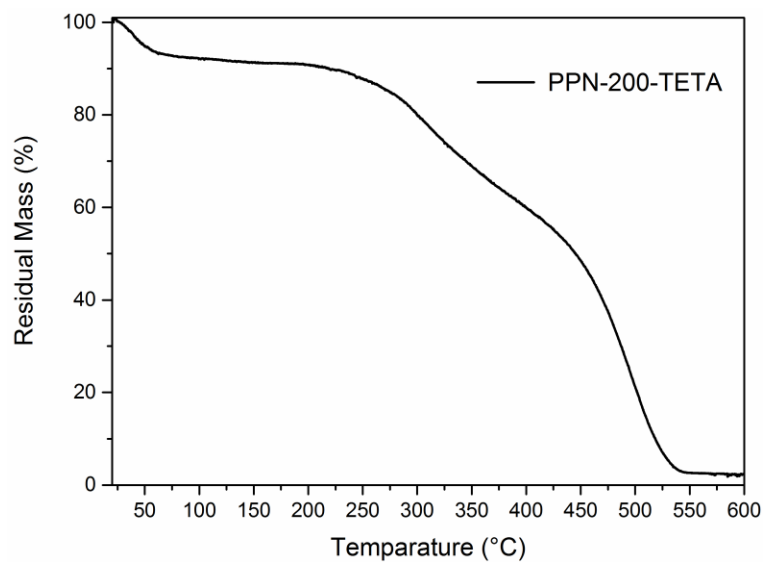


Figure IV-16 TGA of PPN-200-TETA.

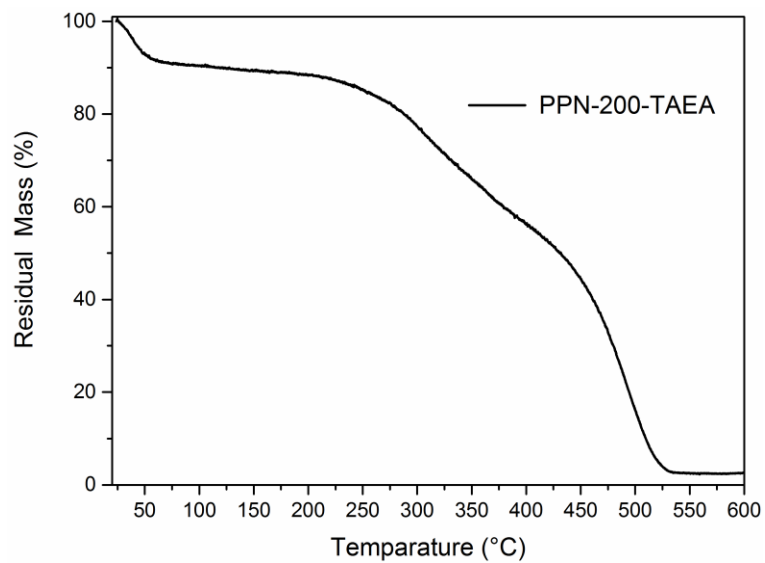


Figure IV-17 TGA of PPN-200-TAEA.

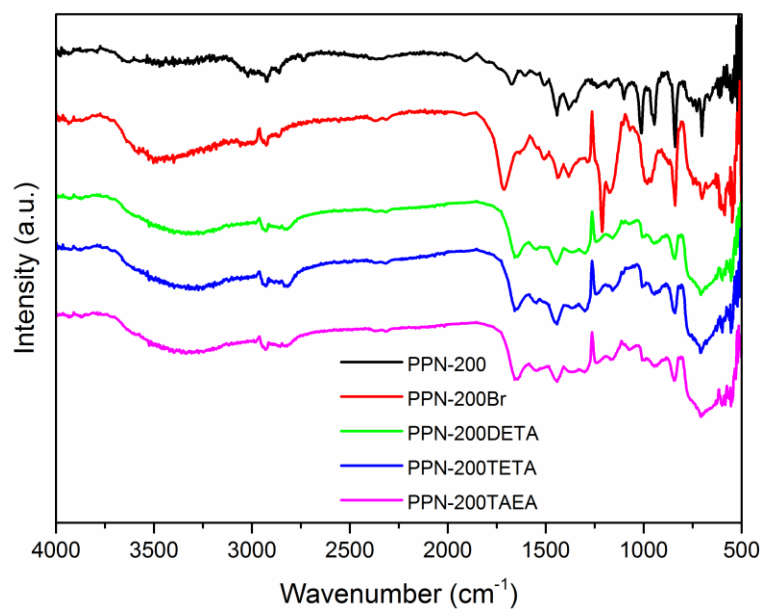


Figure IV-18 FT-IR patterns of the PPN-200, PPN-200Br, and PPN-200-amines.

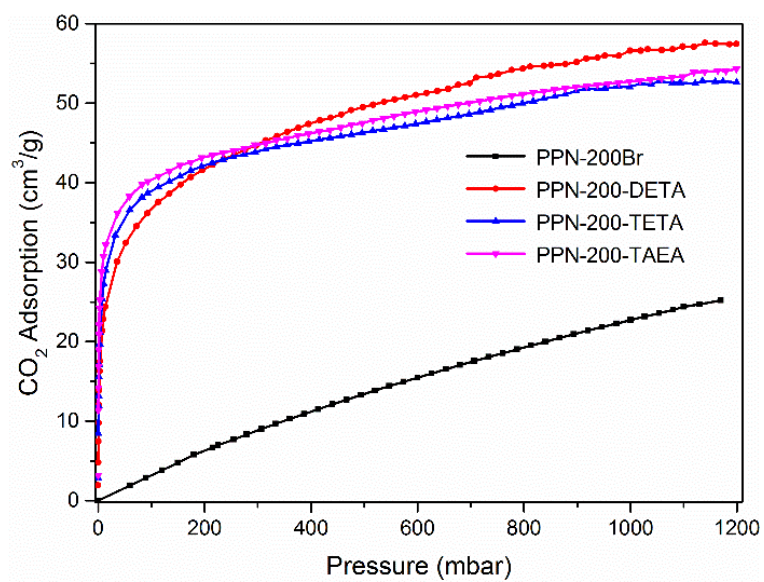


Figure IV-19 CO₂ adsorption of PPN-200Br and PPN-200-amines.

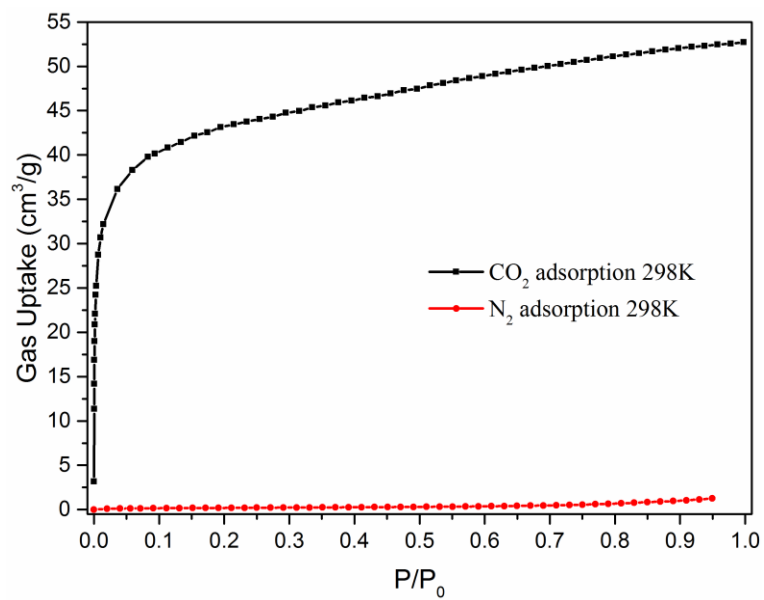


Figure IV-20 CO₂ and N₂ adsorption for PPN-200-TAEA at 298K.

4.4 Conclusion

In conclusion, we have successfully designed a novel strategy to synthesize a series of alkylamine functionalized PPN materials (PPN-200-DETA, PPN-200-TETA, and PPN-200-TAEA), which demonstrated excellent carbon capture properties. Among them, the CO₂ uptake of PPN-200-TAEA reaches 42 cm³/g (8.3 wt%) at 298 K and 0.15 bar and its calculated CO₂/N₂ selectivity reaches 289. Given the outstanding physicochemical stability and high CO₂ adsorption under 0.15 bar, the PPN-200-TAEA has great potential for practical application in postcombustion carbon capture.

CHAPTER V

SUMMARY AND PERSPECTIVE

5.1 Project Summary

Before this work, nearly all reported works share several drawbacks, which limit the development of core-shell MOF. The first limitation is the stepwise synthesis. All reported works are based on the stepwise synthesis, which need to prepare the core MOF and then use it as the seed crystal to grow the second MOF around it. The second limitation is the core MOF and shell MOF must use similar or same ligand, which makes the lattices of core MOF and shell MOF are same. The third limitation is stability. As most of core-shell MOFs are composed of divalent metal ion, which makes the materials are not stable high enough to suffer from the harsh condition. So the research about core-shell MOF mainly focuses on the gas storage/separation and crystallography study.

The work in the dissertation has pushed the envelope of core-shell MOF research. Under the guidance of nucleation kinetics control strategy, a series of stable core-shell MOFs with mismatching lattice were prepared through one-step synthesis.

In Chapter II, a series of zirconium core-shell MOFs, with needle-like cores and octahedral shells, have been prepared through one-step synthesis. Linkers with high connectivity (TCPP) bind strongly with metal cations, allowing for fast homogeneous nucleation in solvothermal reaction conditions. The resulting crystals (PCN-222) subsequently work as seed crystals to accelerate the heterogeneous nucleation of the second MOF, which leads to the formation of the core-shell structure. The crystallinity, porosity, surface area, and structure of core-shell MOFs were demonstrated through

various characterization methods. As the core-shell MOFs can take advantage of both biomimetic catalytic center and adjustable window size, the materials can work as heterogeneous catalyst for olefin epoxidation. The size-selective catalytic behavior of the core-shell MOFs was tuned by changing the ligand length of the shell MOF.

In Chapter III, the selective catalytic behavior of core-shell MOF was further explored by changing the ligand functionalities. In this case, the window size of shell MOF was controlled by attaching different functional groups. To demonstrate the generality of the nucleation kinetics control strategy, other core-shell MOFs, such as PCN-134@Zr-BTB, La-TCPP@La-BPDC, and PCN-222@Nu-1000, were synthesized.

In Chapter IV, to efficiently capture CO₂ from post-combustion gas, a novel post-synthetic method, called anchor installation, was put forward. In this method, diamondoid PPN-200 was synthesized by Suzuki coupling reaction. Through two-step modifications, (i.e. bromination and amination) three alkylamine tethered PPNs were prepared. With the presence of alkylamine groups, all of the materials (PPN-200-DETA, PPN-200-TETA, and PPN-200-TAEA) have high CO₂ uptake and excellent CO₂/N₂ selectivity.

In conclusion, stable porous materials have shown great potential in different applications, especially in heterogeneous catalysis and carbon capture. Porous materials with desirable properties can be rationally designed and functionalized for specific applications. This work not only prepared a series of highly stable porous materials for different applications but also put forward two strategies to synthesize multifunctional porous materials.

5.2 Outlook

5.2.1 *The Future of MOFs*

With the development of MOF, researchers put forward lots of strategies to introduce functional groups into MOF or increase the complexity of MOF. The first and directed strategy is one-pot synthesis strategy. The representative work of this strategy was published in 2010. In this work, Yaghi and coworkers introduced eight linkers with different functional groups into MOF-5. However, in some case, the organic linkers or metal ions are unstable under solvothermal synthetic conditions so we cannot import them into MOF directly. In this case, we need the second strategy, post-synthetic modification. In this strategy, a prototype MOF is firstly prepared. Then through linker exchange or ion exchange, the original MOF is functionalized. Quests for advanced functionalities in MOFs inevitably requires more complex structures. The MOF structures based on pure MOF are far from enough to satisfy the requirements. Constructing MOF composites by using different materials is a pathway to achieve sophisticated application. We propose the core-shell MOF should be the development direction of MOF research. The core-shell MOF could be synthesized through one-step synthesis, which was guided by nucleation kinetics. The selective catalytic behavior of core-shell MOF could be tuned by changing ligand length and ligand functionality. (Chapter II and III)

5.2.2 Future Work: Tuning Selective Behavior by the Hydrophobicity of Shell MOF

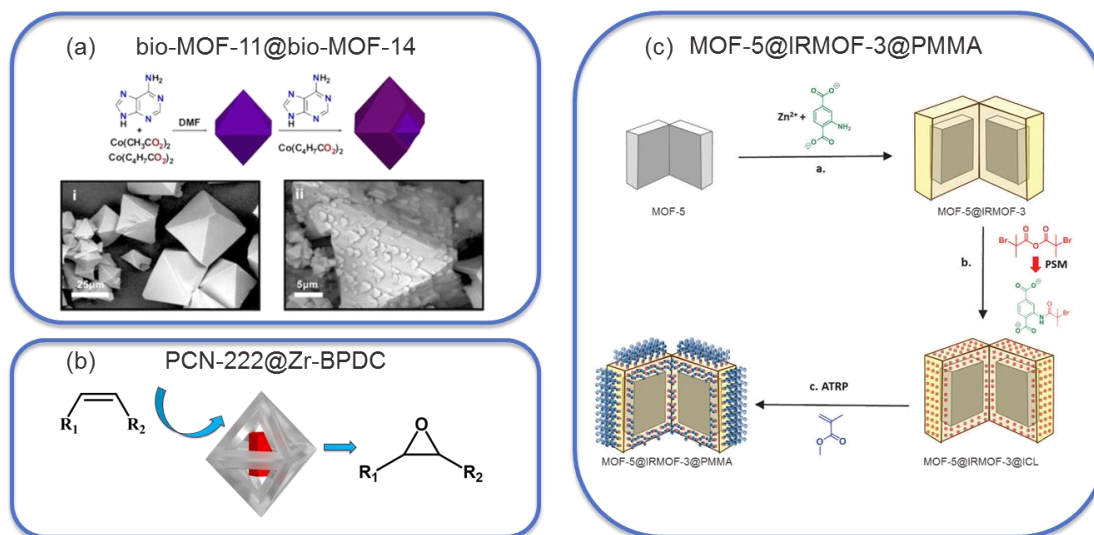


Figure V-1 Advantages of core-shell MOFs

The shell MOF could enrich the functions of the core-shell MOF composite from at least the following three aspects: 1) work as a protective layer to increase the stability of core MOF (Figure V-2a); 2) work as a molecular sieve to discriminate larger guest molecules (Figure V-3b); and 3) serve as transition layer for the covalent attachment to bridge the core MOF (Figure V-4c). From the above-mentioned advantages, we can find that the shell MOF plays an important role in the core-shell MOF. The core-shell MOFs we synthesized own water sensitive heme-like catalytic center. For next step research, we could synthesize series of linkers with fluoro, methyl or alkyl chain on the phenyl rings to increase the hydrophobicity of the shell MOF. Further exploration of hydrophobic shell MOF will lead to the discovery of more useful core-shell MOFs.

5.2.3 Future Work: One-Step Synthesis of Binary Metal Core-Shell MOF

In this work, we have prepared a series of zirconium based core-shell MOFs guided by nucleation kinetic control strategy and extended the strategy to another MOF system (PCN-134@Zr-BTB). However, all of these core-shell MOFs share the same metal in core MOF and shell MOF. As shown in Zn-MOF@Cu-MOF reported by Kitagawa and co-workers, it is possible to extend the one-pot nucleation kinetic control strategy to synthesize hybrid binary metal core-shell MOFs, which will enrich the synthetic methods of core-shell MOFs.

REFERENCES

1. J. Lee, O. K. Farha, J. Roberts, K. A. Scheidt, S. T. Nguyen and J. T. Hupp, *Chem. Soc. Rev.*, 2009, **38**, 1450-1459.
2. H. Li, M. Eddaoudi, M. O'Keeffe and O. M. Yaghi, *Nature*, 1999, **402**, 276.
3. N. L. Rosi, J. Eckert, M. Eddaoudi, D. T. Vodak, J. Kim, M. Keffe and O. M. Yaghi, *Science*, 2003, **300**, 1127.
4. H.-C. Zhou, J. R. Long and O. M. Yaghi, *Chem. Rev.*, 2012, **112**, 673-674.
5. X. Zhu, H. Zheng, X. Wei, Z. Lin, L. Guo, B. Qiu and G. Chen, *Chem. Commun.*, 2013, **49**, 1276-1278.
6. C. J. H. Jacobsen, C. Madsen, J. Houzvicka, I. Schmidt and A. Carlsson, *J. Am. Chem. Soc.*, 2000, **122**, 7116-7117.
7. G. T. Kokotailo, S. L. Lawton, D. H. Olson and W. M. Meier, *Nature*, 1978, **272**, 437-438.
8. F. Hoffmann, M. Cornelius, J. Morell and M. Fröba, *Angew. Chem. Int. Ed.*, 2006, **45**, 3216-3251.
9. F. Tang, L. Li and D. Chen, *Adv. Mater.*, 2012, **24**, 1504-1534.
10. D. Zhao, J. Feng, Q. Huo, N. Melosh, G. H. Fredrickson, B. F. Chmelka and G. D. Stucky, *Science*, 1998, **279**, 548.
11. D. Zhao, Q. Huo, J. Feng, B. F. Chmelka and G. D. Stucky, *J. Am. Chem. Soc.*, 1998, **120**, 6024-6036.
12. A. Ahmadpour and D. D. Do, *Carbon*, 1997, **35**, 1723-1732.

13. J. i. Hayashi, A. Kazehaya, K. Muroyama and A. P. Watkinson, *Carbon*, 2000, **38**, 1873-1878.
14. S. Sircar, T. C. Golden and M. B. Rao, *Carbon*, 1996, **34**, 1-12.
15. M. Suzuki, *Carbon*, 1994, **32**, 577-586.
16. T.-H. Bae, J. S. Lee, W. Qiu, W. J. Koros, C. W. Jones and S. Nair, *Angew. Chem. Int. Ed.*, 2010, **49**, 9863-9866.
17. E. D. Bloch, W. L. Queen, R. Krishna, J. M. Zadrozny, C. M. Brown and J. R. Long, *Science*, 2012, **335**, 1606.
18. D. Britt, H. Furukawa, B. Wang, T. G. Glover and O. M. Yaghi, *PNAS*, 2009, **106**, 20637.
19. D. Britt, D. Tranchemontagne and O. M. Yaghi, *PNAS*, 2008, **105**, 11623.
20. B. Chen, C. Liang, J. Yang, D. S. Contreras, Y. L. Clancy, E. B. Lobkovsky, O. M. Yaghi and S. Dai, *Angew. Chem. Int. Ed.*, 2006, **45**, 1390-1393.
21. O. K. Farha, A. Özgür Yazaydın, I. Eryazici, C. D. Malliakas, B. G. Hauser, M. G. Kanatzidis, S. T. Nguyen, R. Q. Snurr and J. T. Hupp, *Nat. Chem.*, 2010, **2**, 944.
22. Z.-Y. Gu and X.-P. Yan, *Angew. Chem. Int. Ed.*, 2010, **49**, 1477-1480.
23. J. Y. Lee, D. H. Olson, L. Pan, T. J. Emge and J. Li, *Adv. Funct. Mater.*, 2007, **17**, 1255-1262.
24. Y. Li and R. T. Yang, *Langmuir*, 2007, **23**, 12937-12944.
25. S. Ma and H.-C. Zhou, *Chem. Commun.*, 2010, **46**, 44-53.
26. J. A. Mason, M. Veenstra and J. R. Long, *Chem. Sci.*, 2014, **5**, 32-51.

27. A. R. Millward and O. M. Yaghi, *J. Am. Chem. Soc.*, 2005, **127**, 17998-17999.
28. T. Rodenas, I. Luz, G. Prieto, B. Seoane, H. Miro, A. Corma, F. Kapteijn, F. X. Llabrés i Xamena and J. Gascon, *Nat. Mater.*, 2014, **14**, 48.
29. J. L. C. Rowsell, A. R. Millward, K. S. Park and O. M. Yaghi, *J. Am. Chem. Soc.*, 2004, **126**, 5666-5667.
30. M. P. Suh, H. J. Park, T. K. Prasad and D.-W. Lim, *Chem. Rev.*, 2012, **112**, 782-835.
31. P. K. Thallapally, J. Tian, M. Radha Kishan, C. A. Fernandez, S. J. Dalgarno, P. B. McGrail, J. E. Warren and J. L. Atwood, *J. Am. Chem. Soc.*, 2008, **130**, 16842-16843.
32. A. G. Wong-Foy, A. J. Matzger and O. M. Yaghi, *J. Am. Chem. Soc.*, 2006, **128**, 3494-3495.
33. A. H. Chughtai, N. Ahmad, H. A. Younus, A. Laypkov and F. Verpoort, *Chem. Soc. Rev.*, 2015, **44**, 6804-6849.
34. A. Corma, H. García and F. X. Llabrés i Xamena, *Chem. Rev.*, 2010, **110**, 4606-4655.
35. D. Dang, P. Wu, C. He, Z. Xie and C. Duan, *J. Am. Chem. Soc.*, 2010, **132**, 14321-14323.
36. S. Horike, M. Dincă, K. Tamaki and J. R. Long, *J. Am. Chem. Soc.*, 2008, **130**, 5854-5855.
37. J. Liu, L. Chen, H. Cui, J. Zhang, L. Zhang and C.-Y. Su, *Chem. Soc. Rev.*, 2014, **43**, 6011-6061.

38. Y. Liu, W. Xuan and Y. Cui, *Adv. Mater.*, 2010, **22**, 4112-4135.
39. L. Ma, C. Abney and W. Lin, *Chem. Soc. Rev.*, 2009, **38**, 1248-1256.
40. C.-D. Wu, A. Hu, L. Zhang and W. Lin, *J. Am. Chem. Soc.*, 2005, **127**, 8940-8941.
41. C.-D. Wu and W. Lin, *Angew. Chem. Int. Ed.*, 2007, **46**, 1075-1078.
42. M. Yoon, R. Srirambalaji and K. Kim, *Chem. Rev.*, 2012, **112**, 1196-1231.
43. M. Zhao, S. Ou and C.-D. Wu, *Acc. Chem. Res.*, 2014, **47**, 1199-1207.
44. L. Zhu, X.-Q. Liu, H.-L. Jiang and L.-B. Sun, *Chem. Rev.*, 2017, **117**, 8129-8176.
45. B. Chen, L. Wang, Y. Xiao, F. R. Fronczek, M. Xue, Y. Cui and G. Qian, *Angew. Chem. Int. Ed.*, 2009, **48**, 500-503.
46. B. Chen, L. Wang, F. Zapata, G. Qian and E. B. Lobkovsky, *J. Am. Chem. Soc.*, 2008, **130**, 6718-6719.
47. L. He, Y. Liu, J. Liu, Y. Xiong, J. Zheng, Y. Liu and Z. Tang, *Angew. Chem. Int. Ed.*, 2013, **52**, 3741-3745.
48. Z. Hu, B. J. Deibert and J. Li, *Chem. Soc. Rev.*, 2014, **43**, 5815-5840.
49. L. E. Kreno, K. Leong, O. K. Farha, M. Allendorf, R. P. Van Duyne and J. T. Hupp, *Chem. Rev.*, 2012, **112**, 1105-1125.
50. Q. Tang, S. Liu, Y. Liu, J. Miao, S. Li, L. Zhang, Z. Shi and Z. Zheng, *Inorg. Chem.*, 2013, **52**, 2799-2801.
51. M. Zhang, G. Feng, Z. Song, Y.-P. Zhou, H.-Y. Chao, D. Yuan, T. T. Y. Tan, Z. Guo, Z. Hu, B. Z. Tang, B. Liu and D. Zhao, *J. Am. Chem. Soc.*, 2014, **136**, 7241-7244.

52. A. J. Amali, J.-K. Sun and Q. Xu, *Chem. Commun.*, 2014, **50**, 1519-1522.
53. L. Wang, Y. Han, X. Feng, J. Zhou, P. Qi and B. Wang, *Coord. Chem. Rev.*, 2016, **307**, 361-381.
54. H. B. Wu and X. W. Lou, *Sci. Adv.*, 2017, **3**, eaap9252.
55. W. Xia, A. Mahmood, R. Zou and Q. Xu, *Energy Environ. Sci.*, 2015, **8**, 1837-1866.
56. Y. Zhao, Z. Song, X. Li, Q. Sun, N. Cheng, S. Lawes and X. Sun, *Energy Storage Materials*, 2016, **2**, 35-62.
57. S. Zheng, X. Li, B. Yan, Q. Hu, Y. Xu, X. Xiao, H. Xue and H. Pang, *Adv. Energy Mater.*, 2017, **7**, 1602733.
58. J. An, S. J. Geib and N. L. Rosi, *J. Am. Chem. Soc.*, 2009, **131**, 8376-8377.
59. L. Cooper, T. Hidalgo, M. Gorman, T. Lozano-Fernández, R. Simón-Vázquez, C. Olivier, N. Guillou, C. Serre, C. Martineau, F. Taulelle, D. Damasceno-Borges, G. Maurin, Á. González-Fernández, P. Horcajada and T. Devic, *Chem. Commun.*, 2015, **51**, 5848-5851.
60. J. Della Rocca, D. Liu and W. Lin, *Acc. Chem. Res.*, 2011, **44**, 957-968.
61. P. Horcajada, T. Chalati, C. Serre, B. Gillet, C. Sebrie, T. Baati, J. F. Eubank, D. Heurtaux, P. Clayette, C. Kreuz, J.-S. Chang, Y. K. Hwang, V. Marsaud, P.-N. Bories, L. Cynober, S. Gil, G. Férey, P. Couvreur and R. Gref, *Nat. Mater.*, 2009, **9**, 172.
62. S. Keskin and S. Kızılel, *Ind. Eng. Chem. Res.*, 2011, **50**, 1799-1812.

63. Y. Li, J. Tang, L. He, Y. Liu, Y. Liu, C. Chen and Z. Tang, *Adv. Mater.*, 2015, **27**, 4075-4080.
64. M. Lismont, L. Dreesen and S. Wuttke, *Adv. Funct. Mater.*, 2017, **27**, 1606314.
65. K. Lu, C. He and W. Lin, *J. Am. Chem. Soc.*, 2014, **136**, 16712-16715.
66. A. C. McKinlay, R. E. Morris, P. Horcajada, G. Férey, R. Gref, P. Couvreur and C. Serre, *Angew. Chem. Int. Ed.*, 2010, **49**, 6260-6266.
67. M.-X. Wu and Y.-W. Yang, *Adv. Mater.*, 2017, **29**, 1606134.
68. S. Wuttke, A. Zimpel, T. Bein, S. Braig, K. Stoiber, A. Vollmar, D. Müller, K. Haastert-Talini, J. Schaeske, M. Stiesch, G. Zahn, A. Mohmeyer, P. Behrens, O. Eickelberg, D. A. Bölükbas and S. Meiners, *Adv. Healthcare Mater.*, 2017, **6**, 1600818.
69. S. S. Y. Chui, S. M. F. Lo, J. P. H. Charmant, A. G. Orpen and I. D. Williams, *Science*, 1999, **283**, 1148.
70. O. K. Farha, I. Eryazici, N. C. Jeong, B. G. Hauser, C. E. Wilmer, A. A. Sarjeant, R. Q. Snurr, S. T. Nguyen, A. Ö. Yazaydin and J. T. Hupp, *J. Am. Chem. Soc.*, 2012, **134**, 15016-15021.
71. T. Loiseau, C. Serre, C. Huguenard, G. Fink, F. Taulelle, M. Henry, T. Bataille and G. Férey, *Chem. Eur. J.*, 2004, **10**, 1373-1382.
72. S. Surblé, C. Serre, C. Mellot-Draznieks, F. Millange and G. Férey, *Chem. Commun.*, 2006, 284-286.

73. M. Latroche, S. Surblé, C. Serre, C. Mellot-Draznieks, P. L. Llewellyn, J.-H. Lee, J.-S. Chang, S. H. Jung and G. Férey, *Angew. Chem. Int. Ed.*, 2006, **45**, 8227-8231.
74. W. Lu, Z. Wei, Z.-Y. Gu, T.-F. Liu, J. Park, J. Park, J. Tian, M. Zhang, Q. Zhang, T. Gentle Iii, M. Bosch and H.-C. Zhou, *Chem. Soc. Rev.*, 2014, **43**, 5561-5593.
75. J. H. Cavka, S. Jakobsen, U. Olsbye, N. Guillou, C. Lamberti, S. Bordiga and K. P. Lillerud, *J. Am. Chem. Soc.*, 2008, **130**, 13850-13851.
76. D. Feng, Z.-Y. Gu, J.-R. Li, H.-L. Jiang, Z. Wei and H.-C. Zhou, *Angew. Chem. Int. Ed.*, 2012, **51**, 10307-10310.
77. D. Feng, W.-C. Chung, Z. Wei, Z.-Y. Gu, H.-L. Jiang, Y.-P. Chen, D. J. Darensbourg and H.-C. Zhou, *J. Am. Chem. Soc.*, 2013, **135**, 17105-17110.
78. A. Henschel, K. Gedrich, R. Kraehnert and S. Kaskel, *Chem. Commun.*, 2008, 4192-4194.
79. A. Dhakshinamoorthy, M. Alvaro, H. Chevreau, P. Horcajada, T. Devic, C. Serre and H. Garcia, *Catal. Sci. Technol.*, 2012, **2**, 324-330.
80. P. Horcajada, S. Surblé, C. Serre, D.-Y. Hong, Y.-K. Seo, J.-S. Chang, J.-M. Grenèche, I. Margiolaki and G. Férey, *Chem. Commun.*, 2007, 2820-2822.
81. D. Feng, Z.-Y. Gu, Y.-P. Chen, J. Park, Z. Wei, Y. Sun, M. Bosch, S. Yuan and H.-C. Zhou, *J. Am. Chem. Soc.*, 2014, **136**, 17714-17717.
82. O. V. Zalomaeva, A. M. Chibiryaev, K. A. Kovalenko, O. A. Kholdeeva, B. S. Balzhinimaev and V. P. Fedin, *J. Catal.*, 2013, **298**, 179-185.

83. A. Dhakshinamoorthy, M. Alvaro and H. Garcia, *Chem. Eur. J.*, 2010, **16**, 8530-8536.
84. A. Dhakshinamoorthy, M. Alvaro and H. Garcia, *Adv. Synth. Catal.*, 2010, **352**, 711-717.
85. F. Vermoortele, R. Ameloot, A. Vimont, C. Serre and D. De Vos, *Chem. Commun.*, 2011, **47**, 1521-1523.
86. F. Vermoortele, B. Bueken, G. Le Bars, B. Van de Voorde, M. Vandichel, K. Houthoofd, A. Vimont, M. Daturi, M. Waroquier, V. Van Speybroeck, C. Kirschhock and D. E. De Vos, *J. Am. Chem. Soc.*, 2013, **135**, 11465-11468.
87. F. Vermoortele, M. Vandichel, B. Van de Voorde, R. Ameloot, M. Waroquier, V. Van Speybroeck and D. E. De Vos, *Angew. Chem. Int. Ed.*, 2012, **51**, 4887-4890.
88. F. Vermoortele, R. Ameloot, L. Alaerts, R. Mattheissen, B. Carlier, E. V. R. Fernandez, J. Gascon, F. Kapteijn and D. E. De Vos, *J. Mater. Chem.*, 2012, **22**, 10313-10321.
89. A. Herbst, A. Khutia and C. Janiak, *Inorg. Chem.*, 2014, **53**, 7319-7333.
90. J. Jiang, F. Gándara, Y.-B. Zhang, K. Na, O. M. Yaghi and W. G. Klemperer, *J. Am. Chem. Soc.*, 2014, **136**, 12844-12847.
91. C. M. McGuirk, M. J. Katz, C. L. Stern, A. A. Sarjeant, J. T. Hupp, O. K. Farha and C. A. Mirkin, *J. Am. Chem. Soc.*, 2015, **137**, 919-925.
92. M. G. Goesten, J. Juan-Alcañiz, E. V. Ramos-Fernandez, K. B. Sai Sankar Gupta, E. Stavitski, H. van Bekkum, J. Gascon and F. Kapteijn, *J. Catal.*, 2011, **281**, 177-187.

93. Z. Hasan, J. W. Jun and S. H. Jung, *Chem. Eng. J.*, 2015, **278**, 265-271.
94. J. Tang, W. Dong, G. Wang, Y. Yao, L. Cai, Y. Liu, X. Zhao, J. Xu and L. Tan, *RSC Advances*, 2014, **4**, 42977-42982.
95. K. Manna, T. Zhang, F. X. Greene and W. Lin, *J. Am. Chem. Soc.*, 2015, **137**, 2665-2673.
96. Q.-L. Zhu and Q. Xu, *Chem. Soc. Rev.*, 2014, **43**, 5468-5512.
97. Y. K. Hwang, D.-Y. Hong, J.-S. Chang, S. H. Jung, Y.-K. Seo, J. Kim, A. Vimont, M. Daturi, C. Serre and G. Férey, *Angew. Chem. Int. Ed.*, 2008, **47**, 4144-4148.
98. X. Gu, Z.-H. Lu, H.-L. Jiang, T. Akita and Q. Xu, *J. Am. Chem. Soc.*, 2011, **133**, 11822-11825.
99. Q.-L. Zhu, J. Li and Q. Xu, *J. Am. Chem. Soc.*, 2013, **135**, 10210-10213.
100. M. Zhao, K. Yuan, Y. Wang, G. Li, J. Guo, L. Gu, W. Hu, H. Zhao and Z. Tang, *Nature*, 2016, **539**, 76.
101. A. Dhakshinamoorthy, A. M. Asiri and H. García, *Angew. Chem. Int. Ed.*, 2016, **55**, 5414-5445.
102. L. Zeng, X. Guo, C. He and C. Duan, *ACS Catalysis*, 2016, **6**, 7935-7947.
103. M. Dan-Hardi, C. Serre, T. Frot, L. Rozes, G. Maurin, C. Sanchez and G. Férey, *J. Am. Chem. Soc.*, 2009, **131**, 10857-10859.
104. Y. Fu, D. Sun, Y. Chen, R. Huang, Z. Ding, X. Fu and Z. Li, *Angew. Chem. Int. Ed.*, 2012, **51**, 3364-3367.

105. Y. Horiuchi, T. Toyao, M. Saito, K. Mochizuki, M. Iwata, H. Higashimura, M. Anpo and M. Matsuoka, *J. Phys. Chem. C*, 2012, **116**, 20848-20853.
106. S. Yuan, T.-F. Liu, D. Feng, J. Tian, K. Wang, J. Qin, Q. Zhang, Y.-P. Chen, M. Bosch, L. Zou, S. J. Teat, S. J. Dalgarno and H.-C. Zhou, *Chem. Sci.*, 2015, **6**, 3926-3930.
107. C. Gomes Silva, I. Luz, F. X. Llabrés i Xamena, A. Corma and H. García, *Chem. Eur. J.*, 2010, **16**, 11133-11138.
108. J. Long, S. Wang, Z. Ding, S. Wang, Y. Zhou, L. Huang and X. Wang, *Chem. Commun.*, 2012, **48**, 11656-11658.
109. D. Sun, W. Liu, Y. Fu, Z. Fang, F. Sun, X. Fu, Y. Zhang and Z. Li, *Chem. Eur. J.*, 2014, **20**, 4780-4788.
110. J.-D. Xiao, Q. Shang, Y. Xiong, Q. Zhang, Y. Luo, S.-H. Yu and H.-L. Jiang, *Angew. Chem. Int. Ed.*, 2016, **55**, 9389-9393.
111. H.-Q. Xu, J. Hu, D. Wang, Z. Li, Q. Zhang, Y. Luo, S.-H. Yu and H.-L. Jiang, *J. Am. Chem. Soc.*, 2015, **137**, 13440-13443.
112. H. Zhang, J. Wei, J. Dong, G. Liu, L. Shi, P. An, G. Zhao, J. Kong, X. Wang, X. Meng, J. Zhang and J. Ye, *Angew. Chem. Int. Ed.*, 2016, **55**, 14310-14314.
113. M. Li, Z. Zheng, Y. Zheng, C. Cui, C. Li and Z. Li, *ACS Appl. Mater. Interfaces*, 2017, **9**, 2899-2905.
114. A. B. Rao and E. S. Rubin, *Environ. Sci. Technol.*, 2002, **36**, 4467-4475.
115. G. T. Rochelle, *Science*, 2009, **325**, 1652.

116. S. Cavenati, C. A. Grande and A. E. Rodrigues, *Energy & Fuels*, 2006, **20**, 2648-2659.
117. A. Brunetti, F. Scura, G. Barbieri and E. Drioli, *J. Memb. Sci.*, 2010, **359**, 115-125.
118. H. Zhai and E. S. Rubin, *Environ. Sci. Technol.*, 2013, **47**, 3006-3014.
119. T. M. McDonald, W. R. Lee, J. A. Mason, B. M. Wiers, C. S. Hong and J. R. Long, *J. Am. Chem. Soc.*, 2012, **134**, 7056-7065.
120. S. Choi, J. H. Drese and C. W. Jones, *ChemSusChem*, 2009, **2**, 796-854.
121. R. Dawson, L. A. Stevens, T. C. Drage, C. E. Snape, M. W. Smith, D. J. Adams and A. I. Cooper, *J. Am. Chem. Soc.*, 2012, **134**, 10741-10744.
122. R. T. Woodward, L. A. Stevens, R. Dawson, M. Vijayaraghavan, T. Hasell, I. P. Silverwood, A. V. Ewing, T. Ratvijitvech, J. D. Exley, S. Y. Chong, F. Blanc, D. J. Adams, S. G. Kazarian, C. E. Snape, T. C. Drage and A. I. Cooper, *J. Am. Chem. Soc.*, 2014, **136**, 9028-9035.
123. R. Dawson, A. I. Cooper and D. J. Adams, *Polym. Int.*, 2013, **62**, 345-352.
124. W. Lu, D. Yuan, D. Zhao, C. I. Schilling, O. Plietzsch, T. Muller, S. Bräse, J. Guenther, J. Blümel, R. Krishna, Z. Li and H.-C. Zhou, *Chem. Mater.*, 2010, **22**, 5964-5972.
125. D. Yuan, W. Lu, D. Zhao and H.-C. Zhou, *Adv. Mater.*, 2011, **23**, 3723-3725.
126. W. Lu, M. Bosch, D. Yuan and H.-C. Zhou, *ChemSusChem*, 2015, **8**, 433-438.
127. T. R. Cook, Y.-R. Zheng and P. J. Stang, *Chem. Rev.*, 2013, **113**, 734-777.
128. G. Ferey, *Chem. Soc. Rev.*, 2008, **37**, 191-214.

129. S. Kitagawa, R. Kitaura and S.-i. Noro, *Angew. Chem. Int. Ed.*, 2004, **43**, 2334-2375.
130. H. Li, M. Eddaoudi, M. O'Keeffe and O. M. Yaghi, *Nature*, 1999, **402**, 276-279.
131. J. R. Long and O. M. Yaghi, *Chem. Soc. Rev.*, 2009, **38**, 1213-1214.
132. O. K. Farha, A. Özgür Yazaydın, I. Eryazici, C. D. Malliakas, B. G. Hauser, M. G. Kanatzidis, S. T. Nguyen, R. Q. Snurr and J. T. Hupp, *Nat. Chem.*, 2010, **2**, 944-948.
133. S. S. Kaye, A. Dailly, O. M. Yaghi and J. R. Long, *J. Am. Chem. Soc.*, 2007, **129**, 14176-14177.
134. B. Li, H.-M. Wen, H. Wang, H. Wu, M. Tyagi, T. Yildirim, W. Zhou and B. Chen, *J. Am. Chem. Soc.*, 2014, **136**, 6207-6210.
135. S. Ma and H.-C. Zhou, *Chem. Commun.*, 2010, **46**, 44-53.
136. D. Britt, H. Furukawa, B. Wang, T. G. Glover and O. M. Yaghi, *PNAS*, 2009, **106**, 20637-20640.
137. J. R. Li, D. J. Timmons and H. C. Zhou, *J. Am. Chem. Soc.*, 2009, **131**, 6368-6369.
138. F. Luo, C. Yan, L. Dang, R. Krishna, W. Zhou, H. Wu, X. Dong, Y. Han, T.-L. Hu, M. O'Keeffe, L. Wang, M. Luo, R.-B. Lin and B. Chen, *J. Am. Chem. Soc.*, 2016, **138**, 5678-5684.
139. T. Rodenas, I. Luz, G. Prieto, B. Seoane, H. Miro, A. Corma, F. Kapteijn, F. X. Llabrés i Xamena and J. Gascon, *Nat. Mater.*, 2015, **14**, 48-55.

140. M. I. Gonzalez, E. D. Bloch, J. A. Mason, S. J. Teat and J. R. Long, *Inorg. Chem.*, 2015, **54**, 2995-3005.
141. X. Zhang, Z. Zhang, J. Boissonnault and S. M. Cohen, *Chem. Commun.*, 2016, **52**, 8585-8588.
142. B. Chen, Y. Yang, F. Zapata, G. Lin, G. Qian and E. B. Lobkovsky, *Adv. Mater.*, 2007, **19**, 1693-1696.
143. Z. Guo, H. Xu, S. Su, J. Cai, S. Dang, S. Xiang, G. Qian, H. Zhang, M. O'Keeffe and B. Chen, *Chem. Commun.*, 2011, **47**, 5551-5553.
144. F. Luo and S. R. Batten, *Dalton Transactions*, 2010, **39**, 4485-4488.
145. X. Zhu, H. Zheng, X. Wei, Z. Lin, L. Guo, B. Qiu and G. Chen, *Chem. Commun.*, 2013, **49**, 1276-1278.
146. J. A. Hurd, R. Vaidhyanathan, V. Thangadurai, C. I. Ratcliffe, I. L. Moudrakovski and G. K. H. Shimizu, *Nat. Chem.*, 2009, **1**, 705-710.
147. G. K. H. Shimizu, J. M. Taylor and S. Kim, *Science*, 2013, **341**, 354-355.
148. Y. Cui, Y. Yue, G. Qian and B. Chen, *Chem. Rev.*, 2012, **112**, 1126-1162.
149. D. Ma, B. Li, X. Zhou, Q. Zhou, K. Liu, G. Zeng, G. Li, Z. Shi and S. Feng, *Chem. Commun.*, 2013, **49**, 8964-8966.
150. H. Xu, F. Liu, Y. Cui, B. Chen and G. Qian, *Chem. Commun.*, 2011, **47**, 3153-3155.
151. P. Horcajada, T. Chalati, C. Serre, B. Gillet, C. Sebrie, T. Baati, J. F. Eubank, D. Heurtaux, P. Clayette, C. Kreuz, J.-S. Chang, Y. K. Hwang, V. Marsaud, P.-N.

- Bories, L. Cynober, S. Gil, G. Férey, P. Couvreur and R. Gref, *Nat. Mater.*, 2010, **9**, 172-178.
152. P. Horcajada, C. Serre, G. Maurin, N. A. Ramsahye, F. Balas, M. Vallet-Regí, M. Sebban, F. Taulelle and G. Férey, *J. Am. Chem. Soc.*, 2008, **130**, 6774-6780.
153. J. Park, Q. Jiang, D. Feng, L. Mao and H.-C. Zhou, *J. Am. Chem. Soc.*, 2016, **138**, 3518-3525.
154. J.-S. Qin, D.-Y. Du, W.-L. Li, J.-P. Zhang, S.-L. Li, Z.-M. Su, X.-L. Wang, Q. Xu, K.-Z. Shao and Y.-Q. Lan, *Chem. Sci.*, 2012, **3**, 2114-2118.
155. H. Deng, C. J. Doonan, H. Furukawa, R. B. Ferreira, J. Towne, C. B. Knobler, B. Wang and O. M. Yaghi, *Science*, 2010, **327**, 846-850.
156. Q. Liu, H. Cong and H. Deng, *J. Am. Chem. Soc.*, 2016, **138**, 13822-13825.
157. T.-F. Liu, L. Zou, D. Feng, Y.-P. Chen, S. Fordham, X. Wang, Y. Liu and H.-C. Zhou, *J. Am. Chem. Soc.*, 2014, **136**, 7813-7816.
158. Z. Wang and S. M. Cohen, *J. Am. Chem. Soc.*, 2007, **129**, 12368-12369.
159. Z. Wang and S. M. Cohen, *Chem. Soc. Rev.*, 2009, **38**, 1315-1329.
160. S. Yuan, Y.-P. Chen, J.-S. Qin, W. Lu, L. Zou, Q. Zhang, X. Wang, X. Sun and H.-C. Zhou, *J. Am. Chem. Soc.*, 2016, **138**, 8912-8919.
161. S. Yuan, L. Zou, H. Li, Y.-P. Chen, J. Qin, Q. Zhang, W. Lu, M. B. Hall and H.-C. Zhou, *Angew. Chem. Int. Ed.*, 2016, **55**, 10776-10780.
162. Y.-Y. Fu, C.-X. Yang and X.-P. Yan, *Chem. Eur. J.*, 2013, **19**, 13484-13491.
163. P. Hu, J. V. Morabito and C.-K. Tsung, *ACS Catal.*, 2014, **4**, 4409-4419.
164. M. Jahan, Q. Bao and K. P. Loh, *J. Am. Chem. Soc.*, 2012, **134**, 6707-6713.

165. G. Lu, S. Li, Z. Guo, O. K. Farha, B. G. Hauser, X. Qi, Y. Wang, X. Wang, S. Han, X. Liu, J. S. DuChene, H. Zhang, Q. Zhang, X. Chen, J. Ma, S. C. J. Loo, W. D. Wei, Y. Yang, J. T. Hupp and F. Huo, *Nat. Chem.*, 2012, **4**, 310-316.
166. J. V. Morabito, L.-Y. Chou, Z. Li, C. M. Manna, C. A. Petroff, R. J. Kyada, J. M. Palomba, J. A. Byers and C.-K. Tsung, *J. Am. Chem. Soc.*, 2014, **136**, 12540-12543.
167. N. Stock and S. Biswas, *Chem. Rev.*, 2012, **112**, 933-969.
168. Q.-L. Zhu and Q. Xu, *Chem. Soc. Rev.*, 2014, **43**, 5468-5512.
169. M. Zhao, K. Yuan, Y. Wang, G. Li, J. Guo, L. Gu, W. Hu, H. Zhao and Z. Tang, *Nature*, 2016, **539**, 76-80.
170. S. Choi, T. Kim, H. Ji, H. J. Lee and M. Oh, *J. Am. Chem. Soc.*, 2016, **138**, 14434-14440.
171. S. Furukawa, K. Hirai, K. Nakagawa, Y. Takashima, R. Matsuda, T. Tsuruoka, M. Kondo, R. Haruki, D. Tanaka, H. Sakamoto, S. Shimomura, O. Sakata and S. Kitagawa, *Angew. Chem. Int. Ed.*, 2009, **48**, 1766-1770.
172. K. Koh, A. G. Wong-Foy and A. J. Matzger, *Chem. Commun.*, 2009, 6162-6164.
173. T. Li, J. E. Sullivan and N. L. Rosi, *J. Am. Chem. Soc.*, 2013, **135**, 9984-9987.
174. M. Pan, Y.-X. Zhu, K. Wu, L. Chen, Y.-J. Hou, S.-Y. Yin, H.-P. Wang, Y.-N. Fan and C.-Y. Su, *Angew. Chem. Int. Ed.*, 2017, **56**, 14582-14586.
175. K. Caldeira and M. E. Wickett, *Nature*, 2003, **425**, 365-365.
176. J. K. Hurst, *Science*, 2010, **328**, 315-316.

177. A. Korre, Z. Nie and S. Durucan, *International Journal of Greenhouse Gas Control*, 2010, **4**, 289-300.
178. C. McGlade and P. Ekins, *Nature*, 2015, **517**, 187-190.
179. P. Friedlingstein, R. M. Andrew, J. Rogelj, G. P. Peters, J. G. Canadell, R. Knutti, G. Luderer, M. R. Raupach, M. Schaeffer, D. P. van Vuuren and C. Le Quere, *Nat. Geosci.*, 2014, **7**, 709-715.
180. T. L. Frolicher, M. Winton and J. L. Sarmiento, *Nature Clim. Change*, 2014, **4**, 40-44.
181. D. S. Jenkinson, D. E. Adams and A. Wild, *Nature*, 1991, **351**, 304-306.
182. F. Parrenin, V. Masson-Delmotte, P. Köhler, D. Raynaud, D. Paillard, J. Schwander, C. Barbante, A. Landais, A. Wegner and J. Jouzel, *Science*, 2013, **339**, 1060-1063.
183. Z. Abdin, M. A. Alim, R. Saidur, M. R. Islam, W. Rashmi, S. Mekhilef and A. Wadi, *Renewable and Sustainable Energy Reviews*, 2013, **26**, 837-852.
184. M. Grätzel, *Inorg. Chem.*, 2005, **44**, 6841-6851.
185. C. X. Guo, G. H. Guai and C. M. Li, *Adv. Energy Mater.*, 2011, **1**, 448-452.
186. V. Scott, S. Gilfillan, N. Markusson, H. Chalmers and R. S. Haszeldine, *Nat. Clim. Change*, 2013, **3**, 105-111.
187. T. Wall, R. Stanger and Y. Liu, *Fuel*, 2013, **108**, 85-90.
188. J. M. Simmons, H. Wu, W. Zhou and T. Yildirim, *Energy Environ. Sci.*, 2011, **4**, 2177-2185.

189. K. Sumida, S. Horike, S. S. Kaye, Z. R. Herm, W. L. Queen, C. M. Brown, F. Grandjean, G. J. Long, A. Dailly and J. R. Long, *Chem. Sci.*, 2010, **1**, 184-191.
190. R. Banerjee, A. Phan, B. Wang, C. Knobler, H. Furukawa, M. O'Keeffe and O. M. Yaghi, *Science*, 2008, **319**, 939-943.
191. A. Phan, C. J. Doonan, F. J. Uribe-Romo, C. B. Knobler, M. O'Keeffe and O. M. Yaghi, *Acc. Chem. Res.*, 2010, **43**, 58-67.
192. B. Wang, A. P. Cote, H. Furukawa, M. O'Keeffe and O. M. Yaghi, *Nature*, 2008, **453**, 207-211.
193. W. Lu, J. P. Sculley, D. Yuan, R. Krishna, Z. Wei and H.-C. Zhou, *Angew. Chem. Int. Ed.*, 2012, **51**, 7480-7484.
194. M. G. Rabbani, T. E. Reich, R. M. Kassab, K. T. Jackson and H. M. El-Kaderi, *Chem. Commun.*, 2012, **48**, 1141-1143.
195. M. G. Rabbani, A. K. Sekizkardes, O. M. El-Kadri, B. R. Kaafarani and H. M. El-Kaderi, *J. Mater. Chem.*, 2012, **22**, 25409-25417.
196. M. Zhang, Z. Perry, J. Park and H.-C. Zhou, *Polymer*, 2014, **55**, 335-339.